THE UNIVERSITY OF MICHIGAN

COLLEGE OF ENGINEERING
Department of Nuclear Engineering

Technical Report

MEASUREMENT OF FAST NEUTRON SPECTRA IN WATER AND GRAPHITE

Lawrence Harris, Jr.

ORA Project 07786

supported by:

DEPARTMENT OF HEALTH, EDUCATION, AND WELFARE
PUBLIC HEALTH SERVICE
BUREAU OF STATE SERVICES
DIVISION OF RADIOLOGICAL HEALTH
GRANT NO. RH-00253-03
WASHINGTON, D.C.

administered through:

OFFICE OF RESEARCH ADMINISTRATION ANN ARBOR

April 1967

This report was also a dissertation submitted in partial fulfillment of the requirements for the degree of Doctor of Philosophy in The University of Michigan, 1967.

ACKNOWLEDGMENTS

The development of the spectrometer reported here was initiated by Lt. Col. Glenn G. Sherwood, U.S.A.F., who later carried out the detailed NIOBE calculations. Professor John S. King has directed this work since its beginning. His guidance and encouragement are gratefully acknowledged. Also, Assistant Professor Glenn F. Knoll contributed substantially to the spectrometer development.

The cooperation of Messrs. J. B. Bullock, R. D. Martin, and J. R. Miller, and the reactor operators during the spectrum measurements was outstanding. Dr. H. G. Olson and the Phoenix Memorial Laboratory staff provided considerable assistance throughout this program. Their help is greatly appreciated.

Financial assistance was provided by three AEC Special Fellowships in Nuclear Science and Engineering and by grants from the Michigan Memorial—Phoenix Project (Research Grant 215) and the Division of Radiological Health, U. S. Public Health Service (Research Grant RH 00253).

The untiring encouragement and support of my wife, Carole, have been invaluable.

TABLE OF CONTENTS

	Page
LIST OF TABLES	v
LIST OF FIGURES	vi
ABSTRACT	ix
CHAPTER	
I. INTROUDCTION	1
A. Significance of Fast Neutron Spectrum Measurements in Bulk Media	1
B. Methods for Measuring Fast Neutron Spectra in Bulk Media	2
1. Threshold Activation Method	2
2. Time-of-Flight Method	2
3. Nuclear Reaction Method	5
4. Proton-Recoil Method	6
C. Fast Neutron Spectrum Measurements in Bulk Media	8
II. SPECTROMETER DESIGN AND OPERATION	12
A. Principles of Design and Operation	12
1. Energy Analysis	12
2. Energy Calibration	14
3. Thick Detector Operation	15
4. Thin Detector Operation	15
B. Detectors	17
1. Silicon Surface Barrier Detectors	17
2. Depletion Region	20
3. Electron-Hole Pair Generation	23
4. Electron-Hole Pair Collection	24
5. Energy Calibration	25
6. Leakage Current	26
C. Instrumentation	26
D. Signal-to-Background Ratio	29
1. Sources of Background	30
2. Design Considerations	31
3. Influence of Detector Thickness	34
4. Carbon Recoils	39
5. Collimator Effects	39
E. Efficiency	40
F. Energy Resolution	47
1. Detector Term	47

TABLE OF CONTENTS (Concluded)

		Page
	2. Radiator Term	49
	3. Geometry Term	49
	4. System Resolution	55
	5. Influence on Measurement	57
G.	Energy Range	60
III.	EXPERIMENTAL RESULTS	61
A.	Ford Nuclear Reactor	61
	1. Reactor Description	61
	2. Reactor Power Measurement	61
B.	Water Measurements	63
	1. Normalization	63
	2. Reactor Power	66
	3. Counting Times and Statistics	66
	4. Measured Spectra	67
	5. Experimental Uncertainties	69
C.	Graphite Measurements	71
	1. Description of Graphite Slabs	71
	2. Reactor Core Modification	74
	3. Normalization and Reactor Power	74
	4. Counting Times and Statistics	75
	5. Measured Spectra and Experimental Uncertainties	75
IV.	COMPARISON WITH CALCULATIONS AND CONCLUSIONS	77
A.	NIOBE Calculations	77
	1. Neutron Transport Equation	77
	2. Source Terms	79
	3. Energy Groups	81
	4. Geometry	82
	5. Cross Sections	83
	6. Comparison with Measurements	83
B.	Conclusions	86
C.	Suggested Future Work	87
APPENDICES		
A.	EFFECT OF CARBON RECOILS	89
B.	COLLIMATOR EFFECTS	96
C.	TABULATION OF MEASURED SPECTRA	100
REFERENCES		105

LIST OF TABLES

Table		Page
1.	Methods for Measuring Fast Neutron Spectra in Bulk Media	3
2.	Fast Neutron Spectrum Measurements in Bulk Media	9
3.	Silicon Surface Barrier Detectors	21
4.	Proton Energy Analysis Instrumentation	29
5.	Anticoincidence Instrumentation	29
6.	Influence of $F(r_m)$ on $\Delta(\cos^2\psi)$	55
7.	Principal Experimental Uncertainties	70
8.	Ratios of Calculated Flux to Measured Flux	84

LIST OF FIGURES

Figure		Page
1.	Principal features of proton-recoil fast neutron spectrometer.	13
2.	Block diagram of instrumentation used with thick proton detector.	16
3.	Block diagram of instrumentation used with thin proton detector showing anticoincidence system that counts only protons stopped in thin detector.	18
4.	Calculated energy response of two tandem silicon detectors to protons.	19
5.	Block diagram and equivalent circuit for reverse-biased detector, charge-sensitive preamplifier, and amplifier.	28
6.	Background count rates for detector positions above and below collimator axis.	32
7.	Proton recoil spectrum obtained using thick (1040 microns) detector and thick (2.95 mg/cm^2) radiator with collimator against reactor core.	35
8.	Signal-to-background ratios for proton recoil spectra obtained using thick (1040 microns) detector and thick (2.95 mg/cm^2) radiator.	36
9.	Ratio of thick detector background to thin detector background.	37
10.	Proton recoil spectra obtained using thin (245 microns) detector and thin (1.25 mg/cm^2) radiator with collimator against reactor core.	38
11.	Calculated efficiency: $\epsilon_R(E)$.	44
12.	Calculated total efficiency: $\epsilon(E)$.	45
13.	Calculated energy Jacobian: dE/dE_p.	48

LIST OF FIGURES (Concluded)

Figure		Page
14.	Radiator-detector geometry used for calculation of $f(\psi)$ and $f(\cos^2\psi)$.	51
15.	Example of construction used for calculation of $S(\psi)$.	54
16.	Calculated distribution function: $f(\cos^2\psi)$.	56
17.	Calculated energy resolution: $\Delta E/E$.	58
18.	Ford Nuclear Reactor core configurations.	62
19.	Spectrometer suspended above FNR pool.	64
20.	Collimator positioned 60 cm from FNR core.	65
21.	Neutron penetration in water.	68
22.	Two views of four graphite slabs.	72
23.	Three graphite slabs positioned against FNR core.	73
24.	Neutron penetration in graphite.	76
25.	Range of carbon ions in polyethylene.	94
26.	Ratio of carbon recoil counts to proton recoil counts.	95

ABSTRACT

Detailed knowledge of the energy and spatial distributions of fast neutrons in bulk media is required in radiation shielding, radiation effects, and fast reactor physics. Although computer codes are available to calculate spatially dependent spectra with accuracies presumably limited only by uncertainties in cross sections and source spectra, few spectrum measurements which provide a good test for these calculations have been reported.

Here a relatively simple, moderate resolution (12%), differential proton-recoil, fast neutron spectrometer has been developed to measure directed neutron fluxes in the presence of high intensity fission gamma fields of 10^7 to 10^8 roentgens/hour. Good signal-to-background ratios are obtained by (1) careful shielding, (2) using silicon surface barrier detectors, (3) positioning the detectors out of the collimated beam of mixed radiation which traverses the thin polyethylene (CH_2) radiator, and (4) using tandem detectors in anticoincidence. The efficiency is about 10^{-6} for neutrons incident on the radiator.

Measurements of the energy spectrum from 2 to 12 Mev of normally directed neutrons which leaked from the Ford Nuclear Reactor core and penetrated 0, 20.0, 40.0, and 60.0 cm of H_2O and 0, 20.2, 40.4, and 60.6 cm of graphite are reported. The relatively high accuracy of these deep penetration measurements ($\pm$10% relative intensity and $\pm$20% absolute intensity, $\pm$2% energy) makes them useful for testing calculations. Comparison with detailed transport calculations shows good agreement.

CHAPTER I

INTRODUCTION

A. SIGNIFICANCE OF FAST NEUTRON SPECTRUM MEASUREMENTS IN BULK MEDIA

Knowledge of the energy and spatial distributions of fast neutrons (1 - 15 Mev) in bulk media is required in the design of radiation shielding,[1-4] the study of radiation effects,[5-7] and the design of fast reactors.[8-11] The parallel development of high-speed digital computers with large memory capacity and multigroup computer codes based on transport and Monte-Carlo methods has made detailed calculations of fast neutron spectra feasible. With the more rigorous codes such as NIOBE,[12-14] DTF-IV,[15] and 05R,[16] the accuracy of the calculations is essentially limited only by uncertainties in the cross sections and source representation. Unfortunately, due to the difficulty of measuring space and energy dependent fast neutron fluxes, these calculations are usually tested only against integral flux measurements[17] or against other calculations.[18] Clearly the best test of a code, and the representation of the cross sections and the source is a comparison with spectrum measurements. Only by such comparisons can the accuracy of the calculations be established. This work reports a method for accurately measuring spatially dependent fast neutron spectra in bulk media. Measurements in two common reactor materials are presented and compared with detailed calculations.

B. METHODS FOR MEASURING FAST NEUTRON SPECTRA IN BULK MEDIA

Numerous reviews[1,19-25] of the methods used to measure fast neutron spectra have been published. The current methods used to measure spectra (1-15 Mev) in bulk media are listed in Table 1. Table 1 also gives typical values for the efficiency and resolution reported for each method and indicates which methods require beam extraction. When a beam is extracted, the directional or angular flux is measured; otherwise, the scalar flux is measured. In this section, each method is discussed briefly with emphasis on its limitations.

1. Threshold Activation Method

The threshold activation method[26-29] is based on the activation of foils with activation thresholds in the energy region of interest. Its principal limitations are low efficiency and low resolution. The low efficiency results from the small size of the foils used and the low cross sections in the Mev range. The low resolution is due first to the limited number of materials with suitable activation thresholds and well-known cross sections, and secondly to the uncertainties associated with the unfolding of spectra from the activation data.

2. Time-of-Flight Method

The time-of-flight (TOF) method consists of measuring neutron flight times over a known flight path. The origin of the flight time is usually defined by using a pulsed neutron source. The application of this technique to spectrum measurements in bulk media has been made possible by

TABLE 1

METHODS FOR MEASURING FAST NEUTRON SPECTRA IN BULK MEDIA

Method	Beam Extraction	Detector	Efficiency	Resolution
1. Threshold Activation	Not Required	Foils	Low	Low
2. Time-of-Flight (TOF)	Required	Liquid Organic Scintillator[33]	10^{-8} -10^{-6} (includes collimation)	10%
3. Nuclear Reaction				
A. $Li^6(n,\alpha)H^3$	Not Required (but used in this example)	Silicon Surface Barrier Detectors in Sandwich Configuration[36]	10^{-7} -10^{-6} or 10^{-9} -10^{-8} (includes collimation)	21% at 3 Mev 2% at 14 Mev
B. $He^3(n,p)H^3$	Not Required	He^3 Filled Proportional Counter[40]	10^{-4} -10^{-3}	3% - 5%
4. Proton Recoil				
A. Integral	Not Required	Liquid Organic Scintillator[49]	0.15 - 0.40	32% at 1 Mev 9% at 14 Mev
B. Differential	Required	Silicon Surface Barrier Detectors in Tandem Configuration[57]	3-6 x 10^{-6} or 3-6 x 10^{-9} (includes collimation)	24% at 2 Mev 15% at 3 Mev 12% at 12 Mev

the development of high intensity, nanosecond scale, pulsed neutron sources. The high intensity is required because of the long flight paths necessary for good resolution and because of the limitation imposed on the repetition rate by the increase of the pulse width along the flight path. For measurements in nonmultiplying media,[9,30,31] an electron linear accelerator (LINAC) is generally used to bombard lead or depleted uranium targets with ~30 Mev electrons to generate bremsstrahlung. This in turn generates up to 10^{13} neutrons per second with a near fission spectrum by (γ,n) and (γ,f) reactions. Flight paths are usually 50 to 60 meters long. For measurements in multiplying media,[9,10,32] less intense sources are required. The neutron yield obtained from a positive ion accelerator through the $H^2(d,n)He^3$ and $H^3(d,n)He^4$ reactions is adequate for some measurements.

With current TOF apparatus used with LINAC sources, the principal limitations on resolution are due to (1) counting statistics which require channel grouping to make statistical uncertainties less than some specified value,[33] and/or (2) uncertainty in the mean time and the variance in time for neutrons to slow down and migrate from the source to the entrance of the flight path.[34] According to Russell, et al.,[30] this latter effect is small but nonnegligible (~10 ns above 0.5 Mev) in hydrogenous media, but it may lead to ~40% energy resolution for measurements in a large shield of high A elements such as lead. If this is true, a 50-meter flight path is too short for these measurements.

Profio[33] points out that the main shortcomings of his TOF technique

are the uncertainties in the detector efficiency and the transient gamma background. In order to surpress the latter, a 3.14-cm thick depleted uranium plate was interposed in the flight path during measurements. The effect of the depleted uranium is indicated by spectrum measurements made with and without the filter. Addition of the filter reduced the measured 1 Mev flux, presumably after correction for attenuation by the filter, by a factor of three. The measured 10 Mev flux was reduced by 20%. These results indicate the gamma background may be causing substantial errors.

3. Nuclear Reaction Method

The nuclear reaction method uses either the $He^3(n,p)H^3$ reaction (Q = +0.76 Mev) or the $Li^6(n,\alpha)H^3$ reaction (Q = +4.78 Mev) to produce charged particles whose total energy is equal to the energy of the neutron plus the Q of the reaction. This energy is measured using semiconductor detectors,[35-39] gas proportional counters,[40,41] or scintillation crystals.[42,43]

The semiconductor detectors are arranged in a sandwich configuration with either a thin Li^6F film[35-37] or He^3 gas at up to 995 psi pressure[38,39] between them. A sum-coincidence circuit is used to obtain signals proportional to the full energy of both reaction products and to remove noncoincident background. The positive Q of both reactions also assists in gamma discrimination.

Use of the Li^6F film is complicated by competing reactions and by $Li^6(n,\alpha)H^3$ reactions induced by thermal neutrons for which the reaction

cross section is very high. Similarly, the use of He^3 gas is complicated by competing reactions (especially elastic scattering which produces He^3 recoils).

4. Proton-Recoil Method

The proton-recoil method consists of measuring the energy of elastically scattered protons. The proton energy, E_p, is related to the neutron energy, E, by the relation, $E_p = E \cos^2\psi$, where ψ is the n-p scattering angle in the laboratory system. If all of the scattered protons are counted, an integral proton spectrum is obtained. This must be differentiated or unfolded to obtain the neutron spectrum.

In early applications of the integral proton-recoil method, integral proton spectra obtained with stilbene scintillation crystals were differentiated.[44] More recently, sophisticated unfolding techniques have been developed to convert integral proton spectra obtained in stilbene scintillator crystals[45,46] and liquid organic scintillators[47-49] and in hydrogen filled and methane filled proportional counters[50-52] to neutron spectra. Pulse shape gamma discrimination is usually used in conjunction with these detectors.

The chief limitations of the integral proton-recoil method are that the unfolding techniques require precise detector response functions in order to be accurate, and the background due to gamma interactions and neutron interactions other than single n-p scattering is difficult to determine precisely.

In contrast to the integral proton-recoil method, if only those protons scattered through $d\psi_o$ about ψ_o are counted, a differential proton spectrum is obtained. Since this is related to the neutron spectrum through $E_p = E \cos^2 \psi_o$, the conversion to the neutron spectrum is straightforward.

With this method, a thin hydrogeneous material, such as polyethylene (CH_2), is located in a neutron beam and the protons scattered into some solid angle are intercepted by a detector for energy analysis. The neutron beam is extracted from the source with a collimator system. The hydrogeneous film or proton radiator is made thin to reduce the proton energy losses in it and thus permit good energy resolution. The detectors are usually scintillator crystals[53,54] or semiconductor detectors,[55-57] although Cialella[58,59] has reported using magnetic energy analysis. Radiators may be used in series to increase efficiency,[56] and detectors may be used in series to reduce background with coincidence[53] or anticoincidence[57] techniques. Tandem detector devices are usually called telescopes.

The spectrometer developed as part of this work is a differential proton-recoil device.[57] The detectors are silicon surface barrier diodes as used by Furr and Runyon,[55] and like Herdade, et al.,[54] they are located off the collimator axis. The collimator efficiency is 10^{-3} and the detector efficiency varies from 3 to 6 x 10^{-6} in the energy range 2 to 12 Mev. The resolution is 24% at 2 Mev, but improves to 15% at 3 Mev and to 12% at 12 Mev. For measurements from 2 to 6 Mev, a 1.25 mg/cm^2 thick

polyethylene radiator is used with a 245-micron thick detector. A second detector aligned behind the first one, is used to identify protons which are not stopped in the first detector and, by means of an anticoincidence arrangement, to block signals from the first detector due to these protons. The signals must be blocked because the energy deposition in the first detector does not represent the total proton energy. For measurements from 4 to 12 Mev, a 2.95 mg/cm^2 radiator is used with a single 1040-micron thick detector.

The principal advantages of this type of spectrometer are its low gamma sensitivity, its well-known absolute efficiency, the straight forward conversion from proton spectra to neutron spectra, and the essentially unbounded upper energy limit (available by use of multiple thick detectors and/or a large n-p scattering angle). The main disadvantages are its low efficiency and the lower energy limit of about 1 Mev (due to poor resolution resulting from relatively large proton energy losses in the radiator).

C. FAST NEUTRON SPECTRUM MEASUREMENTS IN BULK MEDIA

Measurements of fast neutron spectra in bulk media which are perhaps the best reported in the literature are summarized in Table 2. Other measurements[43,73-77] were omitted because they are less suitable for testing detailed calculations. Of the measurements listed in Table 2, several are more useful than the others as tests. First, Verbinski and Bokhari's[36,37] spectra (No. 4) are the most detailed measurements of reactor neutron spectra in H_2O that have been published. However, comparison with the NIOBE and

TABLE 2

FAST NEUTRON SPECTRUM MEASUREMENTS IN BULK MEDIA

Number	Group	Year	Neutron Source	Method	Energy Range (Mev)	Medium	Shield Geometry	Penetration Distances	Calculations/Comparison	Ref.
1	ORNL	1953	BSR-I Reactor	Diff. n-p	1.3-10	H_2O	Infinite	0,5,20 & 30 cm at 0°	None	(60)
2	ORNL	1954	BSR-I Reactor	Diff. n-p	1.3- 8.5	Graphite	Slab	0 & 32.7 cm at 0°	None	(61)
3	ORNL	1963	LINAC/Pb Target	TOF	1 -13	LiH	Slab	0,10,20 & 27.5 cm at 0°	NIOBE/Fair	(62)
4	ORNL	1964	BSR-I Reactor	$Li^6(n,\alpha)H^3$	1 -11.5	H_2O	Infinite	0,10,20,30,40 & 50 cm at 0°;20 & 40 cm at 41°; 10,20,30 & 40 cm at 52°	NIOBE & DTK/Fair	(36,37)
5	ORNL	1967	LINAC/Pb Target	TOF	1 -12	H_2O	Slab	0,20 & 40 cm at 0°; 10,20 & 30 cm at 30°	NIOBE & DTK/Good	(37)
6	ORNL	1967	TSR-II Reactor	Int. n-p	0.7-10	Liquid N	Slab	0,61.0 & 91.4 cm	$\exp[-\Sigma_t(E)t]$/Excellent	(49)
7	ORNL	1967	TSR-II Reactor	Int. n-p	1.8-10	Liquid O	Slab	0,61.0 & 91.4 cm	$\exp[-\Sigma_t(E)t]$/Excellent	(49)
8	ORNL	1967	TSR-II Reactor	Int. n-p	0.7-10	Graphite	Slab	0,11.0,20.3 & 30.5 cm	$\exp[-\Sigma_t(E)t]$/Excellent	(49)
9	ORNL	1967	TSR-II Reactor	Int. n-p	0.7-10	Pb	Slab	0 & 15.2 cm	$\exp[-\Sigma_t(E)t]$/Excellent	(49)
10	GA	1964	LINAC/U Target	TOF	0.5-15	Liquid H	Cylinder	0,6.4,11.4,17.8,26.7 & 33.0 cm at 0°, 15°,37°,53°, & 78°	None	(63,64)
11	GA	1964	LINAC/U Target	TOF	0.5-15	CH_2	Infinite	0,5 & 15 cm at 0°; 30 cm at 16°,32° & 60°	GAPLSN & GGSN/Poor	(65,66)
12	GA	1966	LINAC/U Target	TOF	0.5-15	CH_2	Sphere	0,15 & 30 cm at 0°; 30 cm at 11.5°,20.1°, 35.5° & 55.7°	GAPLSN & GGSN/Fair	(33)
13	GA	1966	LINAC/U Target	TOF	0.5-12	Graphite	Infinite	0,20.3,35.6,50.8 & 66.1 cm at 0°	None	(67)
14	USSR(I)	1963	Thermal Reactor	Int. n-p	1 -10	CH_2	Slab	0,10,20,30,60 & 80 grams/cm^2	Moments/Fair	(68)
15	USSR(I)	1964	Thermal Reactor	Int. n-p	1 -11	Graphite	Slab	0,22.5,45,92.5 & 135 cm	Moments/Poor	(69)
16	USSR(I)	1964	Thermal Reactor	Int. n-p	1 -11	Pb	Slab	0,12,24,49 & 74 cm	None	(69)
17	USSR(I)	1964	Thermal Reactor	Int. n-p	1 -11	Fe	Slab	0,10.4,20.4,40 & 65 cm	None	(69)
18	USSR(I)	1965	Thermal Reactor	Int. n-p	1 -12.5	Concrete	Slab	0,10,30,60 & 100 cm	None	(70)
19	USSR(II)	1964	Po-Be	Int. n-p	1.5-10	H_2O	Semi-Infinite	0,10,20,30 & 40 cm	Moments/Fair	(71)
20	USSR(II)	1964	Po-Be	Int. n-p	1.5-10	H_2O	Slab	0,10,20 & 30 cm	None	(71)
21	USSR(II)	1965	Po-Be	Int. n-p	2 -10.5	CH_2	Slab	0 & 45 cm	None	(72)
22	USSR(II)	1965	Po-Be	Int. n-p	1.5-10.5	Al	Slab	0 & 44 cm	None	(72)
23	Mich.	1966	FNR Reactor	Diff. n-p	2 -12	H_2O	Infinite	0,20.0,40.0 & 60.0 cm at 0°	NIOBE/Excellent	(57)
24	Mich.	1966	FNR Reactor	Diff. n-p	2 -12	Graphite	Slab	0,20.2,40.4 & 60.6 cm at 0°	NIOBE/Good	(57)

DTK* calculations shows only fair agreement. Of note is a dip which appears at 3.5 Mev in the calculations and at 4 Mev in the measurements. Since this dip results from the elastic scattering resonance of oxygen at 3.5 Mev, it appears the spectrometer energy calibration was in error. Also, the NIOBE calculations show another dip at 7.3 Mev which does not appear in the measurements. In this case, it seems the NIOBE cross sections used were in error because current oxygen cross sections[78] do not show a sizable resonance near 7.3 Mev.

Secondly, Verbinski's[37] recently reported spectra (No. 5) of (γ,n) and (γ,f) neutrons which penetrated water in slab geometry show good agreement with NIOBE and DTK calculations. However, the comparison is somewhat biased because the measured spectra were individually normalized to the calculated spectra for convenience in comparing spectrum shapes.

Thirdly, Profio's[33] spectra (No. 12) of (γ,n) and (γ,f) neutrons in a paraffin sphere (15.2 cm ID and 76.2 cm OD) were measured in very clean geometry. Even so, comparison with GAPLSN** and GGSN*** calculations shows only fair agreement.

Fourthly, Clifford, et al.'s[49] recently reported spectra (Nos. 6-9) of reactor neutrons which traversed several samples were measured in narrow beam geometry. Thus, only uncollided neutrons were counted. These

---

*DTK is an early LASL version of DTF-IV.

**GAPLSN is a General Atomic version of DTF-IV.

***GGSN is a faster running version of GAPLSN which permits downscattering only.

measured spectra depend only on the spectrum of neutrons incident on the sample, the sample thickness, and the total cross section of the sample material. Comparison with calculated spectra, $N_t(E) = N_o(E) \exp [-\Sigma_t(E)t]$, shows agreement which ranges from good to excellent depending on which of several sets of total cross sections was used. Although these measurements provide excellent tests for the total cross sections, they give no information on slowing down sources.

Thus, in view of the apparent absence of reliable measurements to test calculated spectra which include scattered neutrons, the spectrum measurements (Nos. 23 & 24) reported here should be very useful. At the deeper penetrations, they are in fact dominated by scattered neutrons. For example, the ratio of scattered neutrons to unscattered neutrons ranges from 100 at 2 Mev to 1 at 12 Mev for the neutrons which penetrated 60 cm of H_2O.

CHAPTER II

SPECTROMETER DESIGN AND OPERATION

A. PRINCIPLES OF DESIGN AND OPERATION

The principal features of the proton-recoil, fast neutron spectrometer developed for these measurements are shown in Figure 1. During operation, the spectrometer is submerged in the open pool of the Ford Nuclear Reactor, the 2 megawatt research reactor at The University of Michigan. Fast neutrons from the FNR core stream through the collimator to a proton radiator. The radiator is a thin polyethylene (CH_2) film from which about one out of every 10^6 incident neutrons elastically scatters a proton to the detector. The detector system generates a voltage pulse whose height is proportional to the energy of the incident recoil proton.

1. Energy Analysis

The energy of the recoil protons is related to the energy of the neutrons incident on the radiator by applying the laws of conservation of kinetic energy and linear momentum. Neglecting the small difference between proton mass and neutron mass, this results in the following ratio:

$$\frac{\text{proton energy}}{\text{neutron energy}} = \cos^2\psi$$

where ψ is the n-p scattering angle in the laboratory system. This relation assumes that prior to being scattered, the protons are free and at rest. These assumptions are reasonable for hydrogen nuclei

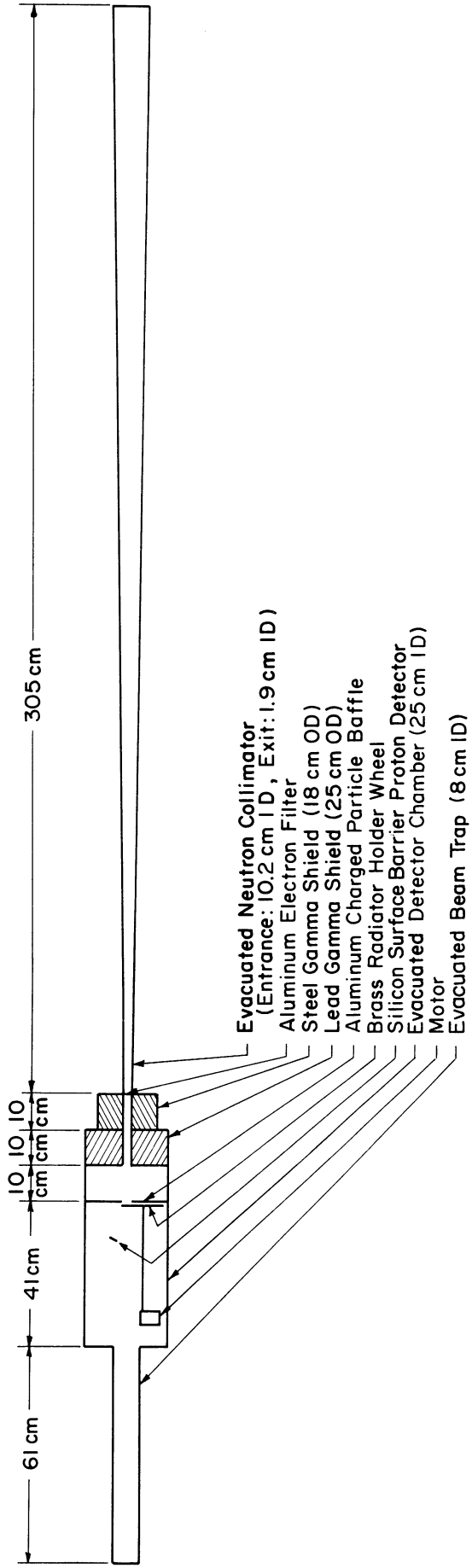

Figure 1. Principal features of proton-recoil fast neutron spectrometer.

held in place by ev bonds and scattered by Mev neutrons.

Since the hydrogen nuclei are scattered from within the radiator, they lose some energy before leaving it. If the remainder of their energy is deposited within the detector, then for neutrons with energy E which scatter protons from the radiator through an angle ψ to the detector,

$$E\cos^2\psi = \int_{RADIATOR}\left(\frac{dE}{dx}\right)dx + \int_{DETECTOR}\left(\frac{dE}{dx}\right)dx$$

This equation assumes the region between the radiator and detector is evacuated and the detector window is very thin. Because the protons are scattered through some angles in $\delta\psi$ about ψ, there are small variations in $\cos^2\psi$. Also, since the protons travel various distances in the radiator before escaping it, there are variations in the proton energy losses in the radiator. Thus, it is necessary to rewrite the above equation in terms of average values in the following approximate form.

$$E\,\overline{\cos^2\psi} = \overline{\int_{RADIATOR}\left(\frac{dE}{dx}\right)dx} + \overline{\int_{DETECTOR}\left(\frac{dE}{dx}\right)dx} \qquad (1)$$

To simplify the notation, define

$$\delta E_p \equiv \overline{\int_{RADIATOR}\left(\frac{dE}{dx}\right)dx} \quad \text{and} \quad E_p \equiv \overline{\int_{DETECTOR}\left(\frac{dE}{dx}\right)dx}$$

Hence the neutron energy,

$$E = \frac{\delta E_p + E_p}{\overline{\cos^2\psi}}$$

2. Energy Calibration

The energy calibration of the spectrometer is based on the above re-

lation. The proton energy deposition in the detector, E_p, is measured with a calibrated detector system. This calibration is described in Section II-B-5. The proton energy deposition in the radiator, δE_p, is generally much less than E_p. δE_p is calculated using range-energy data[79-81] or energy loss data[53,81] for protons traversing an average radiator thickness of $(1/2)t_R \overline{\sec \psi}$, where t_R is the radiator thickness. Determination of $\overline{\sec \psi}$ and $\overline{\cos^2 \psi}$ requires a careful measurement of the radiator-detector geometry and the calculation of their average values as determined by the angular dependence of n-p scattering. Details of this calculation are in Section II-F-3.

3. Thick Detector Operation

In order for the detector response to be proportional to the incident recoil proton energy, the proton must be stopped in the depletion region. A detector thick enough to stop all incident protons is designated a "thick" detector in this connection. Since the measured neutron spectra decrease exponentially above 9 Mev, a detector thick enough to stop protons scattered by 14 Mev neutrons responds essentially as a thick detector for measurements to 12 Mev. A block diagram of the instrumentation used with this detector is shown in Figure 2.

4. Thin Detector Operation

As will be demonstrated in Section II-D-3, the use of a thin detector results in important background reduction. Of course, a thin detector does not stop all incident protons. Thus, in order to accept only those detector

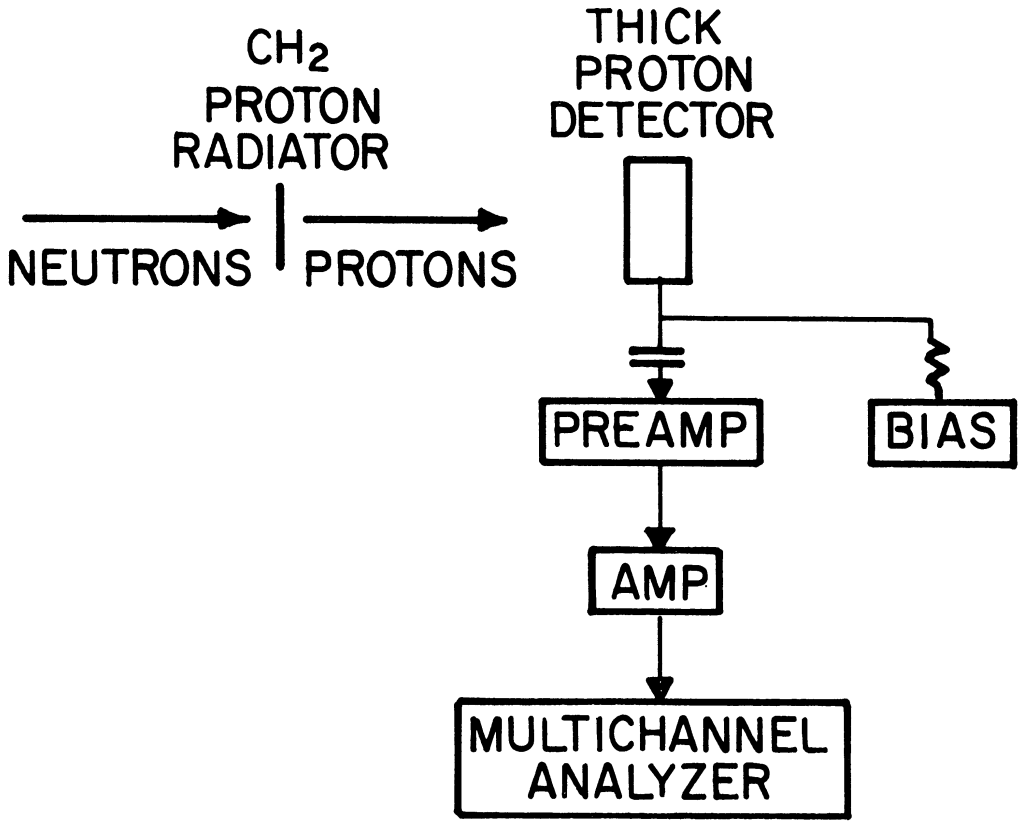

Figure 2. Block diagram of instrumentation used with thick proton detector.

signals due to protons stopped in the thin detector, the two-detector, anti-coincidence arrangement shown in Figure 3 is used. The energy response of the two tandem detectors is indicated in Figure 4. As these figures indicate, protons which traverse the thin detector and deposit enough energy in the second detector to exceed the discriminator level (0.5 Mev), trigger a coincidence pulse which blocks the signal from the thin detector. The dashed lines of Figure 4 show this anticoincidence arrangement should operate satisfactorily for proton energies up to 4.9 Mev. This corresponds to neutron energies up to 6.1 Mev.

The detectors are described in the next section and their instrumentation is covered in detail in Section II-C.

B. DETECTORS

Semiconductor devices were first used for nuclear radiation detection by Van Heerden[82] in 1945. His bulk type detector has been succeeded by the junction type detector first reported by McKay[83] in 1949. It was 1960 before extensive use of the latter detector was reported.[84,85] Today surface barrier and diffused junction detectors of intrinsic and lithium-ion-drifted silicon and germanium are used widely. The detectors used with this spectrometer are intrinsic silicon surface barrier detectors.

1. Silicon Surface Barrier Detectors

These detectors were chosen because of their following characteristics: thin windows, linear response, high resolution, fast response, high stability, low gamma sensitivity, and compact size. Details of the detectors

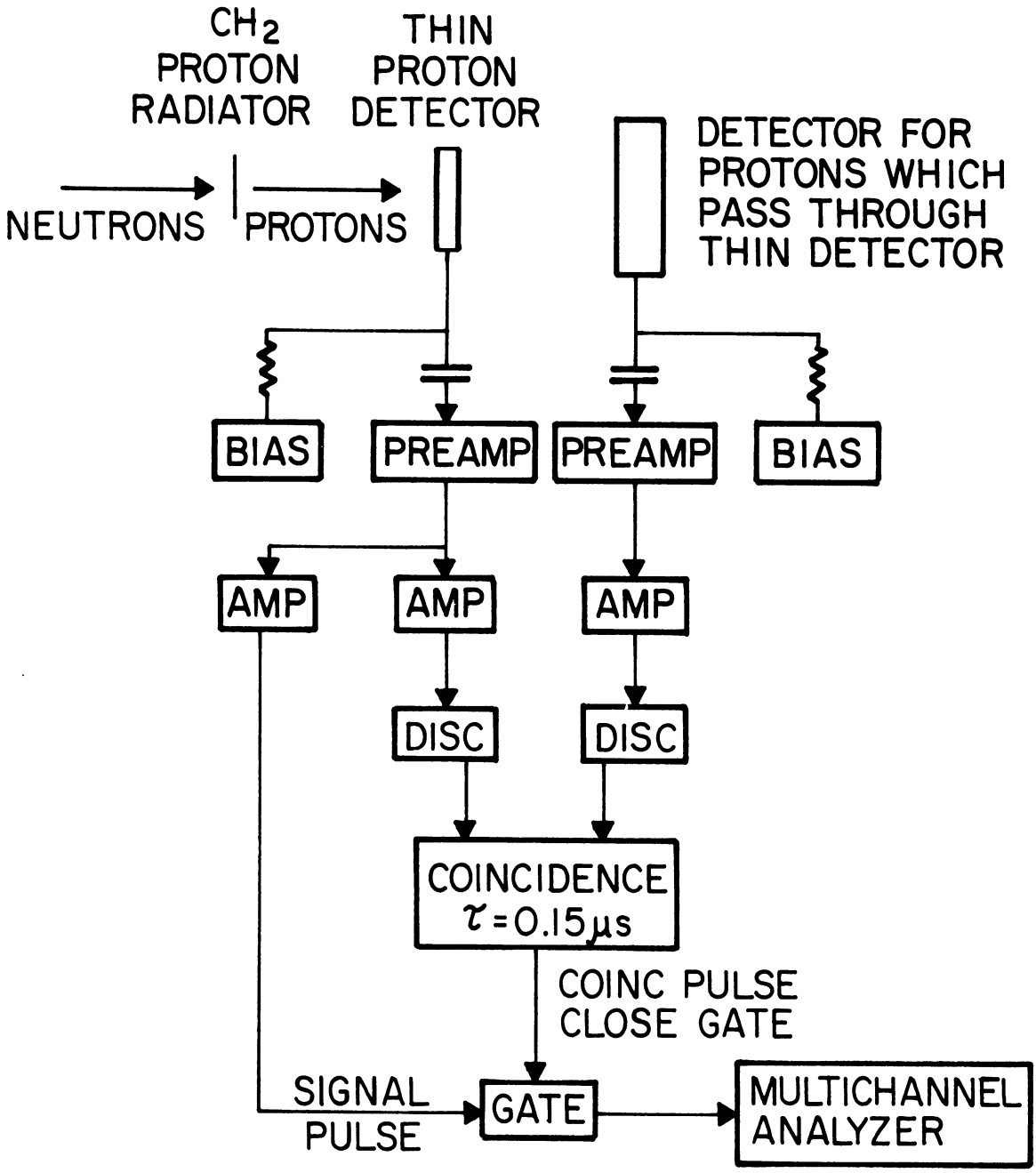

Figure 3. Block diagram of instrumentation used with thin proton detector showing anticoincidence system that counts only protons stopped in thin detector.

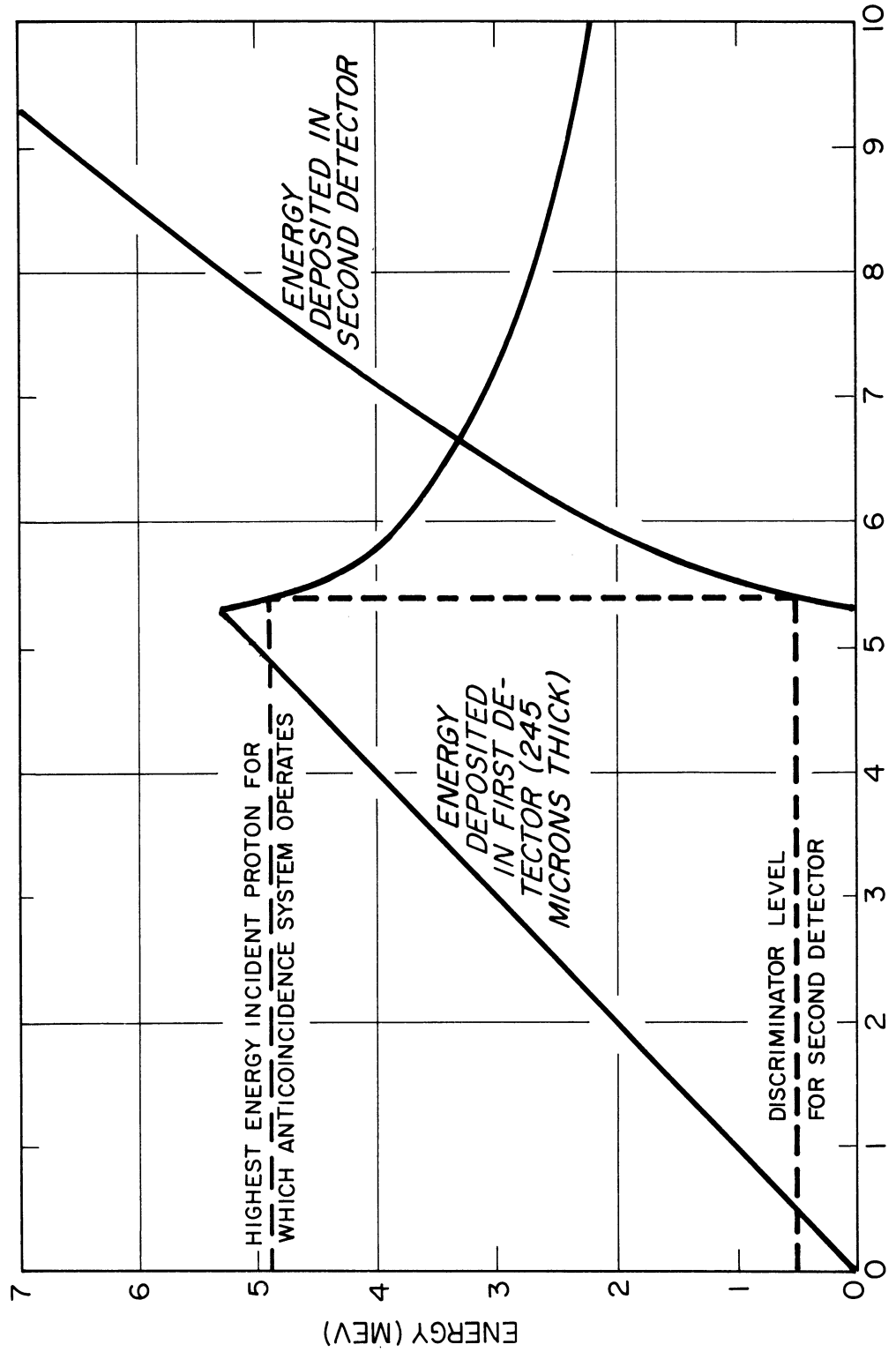

Figure 4. Calculated energy response of two tandem silicon detectors to protons.

are given in Table 3. The operation of these detectors is based on the properties of the depletion region in a semiconductor diode operated with reverse bias. Electron-hole pairs generated in the depletion region by ionizing radiation are collected to provide a direct measure of the energy deposition in this region. The theory of these detectors deals primarily with the establishment of the depletion region and the generation and collection of electron-hole pairs. Although the theory is covered in the literature,[86-89] the essential ideas will be reviewed briefly here.

2. Depletion Region

When n-type and p-type crystals of the same material are placed together, electrons diffuse from the n-type into the p-type crystal and holes diffuse in the opposite direction. The region in which this diffusion occurs is characterized by a depletion of the majority charge carriers and the presence of the resulting space charges due to the bound impurity sites (donors and acceptors). Reverse biasing (plus to n-type and minus to p-type) the junction widens the depletion region. Hence, because the region is depleted of the majority charge carriers, its conductance is low and very little current flows through it. Forward biasing the junction removes the depletion region and current flows freely. This action is the basis for the semiconductor diode rectifier.

The depletion region of the semiconductor diodes is not formed by placing two crystals together. Rather, for the silicon surface barrier detector, a p-type surface layer is formed on a single n-type silicon crystal by ox-

TABLE 3

SILICON SURFACE BARRIER DETECTORS

Detector	Thickness (mm)	Depletion Depth (mm)	Area (cm^2)	Crystal[a] Resistivity (ohm-cm)	Detector[b] Bias (volts)	Capacitance (picofarads)	Leakage[c] Current (microamps)	5.5 Mev Alpha[c] Resolution (Kev)	Manufacturer
Thick Detector	1.040	1.040	1.77	12,000	375	20	1.2	30	ORTEC[d]
Thin Detector (First Tandem Detector)	0.245	0.245	1.77	5,700	55	80	0.7	40	ORTEC
Second Tandem Detector	1.0	0.16	3.0	4,700	35	200	0.7	60	G. G. Sherwood Univ. of Mich.

[a]Intrinsic n-type Silicon

[b]$V_{DET} = V_o + V_{SUPPLY} - I_L R_L, R_L = 22$ megohms, $V_o \cong 0.5$ volt

[c]Measured in Evacuated Test Chamber at 22°C

[d]Oak Ridge Technical Enterprises Corp.

idation. The depletion region extends into the n-type crystal. The approximate thickness of this region is found by solving Poisson's equation for constant space charge density and using the reverse bias and zero electric field as boundary conditions. This thickness is $x = (kV/2\pi\ Ne)^{1/2}$, where k is the dielectric constant of the crystal, V is the reverse bias, e is the electronic charge, and N is the charge density due to impurity sites. If all impurities are ionized, the resistivity of the crystal is $\rho = 1/\mu Ne$, where μ is the majority charge carrier mobility. Thus, $x = (\rho\ Vk\ \mu/2\pi)^{1/2}$ shows the depletion thickness varies as the half power of the crystal resistivity and the reverse bias.

The capacitance of the depletion region is approximately that of a parallel plate capacitor of the same thickness with a silicon dielectric. Thus, the capacitance per unit area,

$$\frac{C}{A} = \frac{K}{4\pi x} = \left(\frac{KNe}{4\pi V}\right)^{\frac{1}{2}} = \left(\frac{K}{4\pi\mu\rho V}\right)^{\frac{1}{2}}$$

When the crystal resistivity and breakdown voltage are sufficiently high, the reverse bias can be increased until the depletion region extends from the p-type surface layer to the other side of the n-type crystal. The resulting fully depleted detector has three advantages over the partially depleted one. First, with the reverse bias somewhat higher than that required for full depletion, the thickness of the depletion region and hence the detector capacitance are insensitive to bias fluctuations. Secondly, with thin windows on both front and back, essentially all of the energy lost by charged particles traversing the detector is deposited in the depletion

region. Thirdly, the pulse rise time is reduced as the undepleted region of the detector is reduced. This is because the undepleted region contributes to the series resistance of the detector and the time constant of the detector equivalent circuit varies as this resistance. As indicated in Table 3, both the thick and thin detectors are fully depleted.

3. Electron-Hole Pair Generation

The average energy required to generate an electron-hole pair in the depletion region is predicted by Shockley[90,91] to be

$$\epsilon = 2.2\, E_g + r E_R$$

where E_g is the energy gap between the valence and conduction bands, E_R is the energy of the highest frequency optical mode phonon, and $r = (L_i/L_R)$, the ratio of the mean free path between ionizing collisions, L_i, and the mean free path for phonon collisions, L_R. For silicon at 300°K, E_g = 1.12 ev. With r = 17.5 and E_R = 0.063 ev, ϵ = 3.57 ev.

Until recently, all measurements indicated that ϵ was independent of the mass, charge and energy of the ionizing particle. However, careful measurements by an Italian group[92] give $\epsilon_\alpha = 3.61 \pm 0.01$ ev for the 5.49 Mev alphas of Am^{241} and $\epsilon_e = 3.79 \pm 0.01$ ev for the 0.365 Mev conversion electrons of Sn^{113}. These results have been substantiated by a U. S. group[93] who found $\epsilon_\alpha = 3.60 \pm 0.01$ ev for the same alphas and $\epsilon_e = 3.80 \pm 0.01$ ev for the 1.05 Mev conversion electrons of Bi^{207}. Both sets of results are for silicon at 300°K (E_g = 1.12 ev) and with the data extrapolated to

infinite collecting electric field to eliminate the influence of trapping and recombination. The approximately 5% difference in ϵ_α and ϵ_e is not explained by Shockley's model. Even so, the agreement with the predicted 3.57 ev gives some credence to his model.

4. Electron-Hole Pair Collection

The collection of electron-hole pairs is impeded by two mechanisms: trapping and recombination. These phenomena usually occur at imperfection sites in the crystal. Trapping of the charge carriers refers to the immobilization of the carriers at trapping centers. If the mean carrier lifetime is on the order of or less than the amplifier clipping time, a substantial portion of the signal is lost. The loss of charge carriers by recombination is most likely to occur in the vicinity of the particle track where the ionization density is highest. This recombination takes place before the electrons and holes in the ionized column are separated by the applied electric field. Hence, recombination increases with increasing ionization density and decreasing electric field. The principal consequence of trapping and recombination is to reduce the collection efficiency and energy resolution of the detector.

The collection efficiency, $\eta = Q/Ne$, gives the ratio of the charge Q on the collecting electrode to the charge generated by the release of N electron-hole pairs. Here $N = E/\epsilon$, where E is the energy deposited in the depletion region and ϵ is the mean number of ion pairs generated per unit energy deposited in this region. Most junction detectors can be biased suf-

ficiently for η to be very nearly 100%.

5. Energy Calibration

The energy calibration of the detectors and their instrumentation is based on the use of a precision pulse generator to determine the zero energy channel and the use of the 5.49 Mev* alphas of Am^{241} to fix the channel width. The pulse generator, whose output is linear, was capacity coupled to the preamplifier input and the pulse amplitudes were varied to obtain a plot of pulse height versus channel number. The intercept of this plot was the zero energy channel. The linearity of this plot demonstrated the linearity of the preamplifier, amplifier, and ADC combination.

The use of alphas to determine the channel width for protons is based on the assumption that $\eta_p/\epsilon_p = \eta_\alpha/\epsilon_\alpha$. It is generally considered that the difference between η_p and η_α is too small to be measured with present techniques. However, a recent measurement[97] gives $\epsilon_p/\epsilon_\alpha \cong 0.99$. At the time of data reduction, this result was unavailable. Hence, in the absence of other data to substantiate it, this 1% is neglected. Future measurements of $\epsilon_p/\epsilon_\alpha$ for silicon may indicate the desirability of correcting the channel width for a small difference between ϵ_p and ϵ_α.

An approximate verification of the calibration procedure was made using the 1.05 Mev[98] conversion electrons of Bi^{207}. Two previously described measurements give $\epsilon_e/\epsilon_\alpha = 1.050 \pm 0.004$ and 1.056 ± 0.004. Assuming then

*Am^{241} alpha spectrum: 5.4870 Mev (86.0%), 5.4435 Mev (12.7%), 5.3880 Mev (1.3%), and 20 others (<0.5%).[94-96]

that $\epsilon_e/\epsilon_p = 1.053$ and $\eta_e/\eta_p = 1.000$, the 1.05 Mev electrons should be counted in the channel calibrated for 1.00 Mev protons. This response was observed.

6. Leakage Currents

Another important characteristic of reverse biased junctions is the current flow in the absence of radiation. This current, called bulk current, must be sufficiently small that heating of the crystal is negligible. The bulk current has two components: the drift current due to the diffusion of minority carriers into the depletion region and the generation current due to the thermal generation of minority carriers in the depletion region.

In addition to the bulk current through the depletion region, some current flows around its edge. This edge leakage or surface leakage current depends on many factors including the design and construction of the detector, treatment and contamination of its surfaces, and ambient conditions such as temperature, humidity, and pressure. The sum of the bulk current and the edge leakage current is called the reverse current or leakage current. It must be much smaller than the signal currents resulting from radiation interactions in the depletion region if the signal-to-noise ratio is to be sufficiently high to permit good energy resolution. Leakage currents for the detectors used here are given in Table 3.

C. INSTRUMENTATION

Integrating or charge-sensitive preamplifiers are used with these junction detectors. This type of preamplifier is favored because its output

is very nearly independent of the detector capacitance. This is indicated in Figure 5 which shows the block diagram and equivalent circuit for a reverse-biased detector, charge-sensitive preamplifier, and amplifier. Here the amplifier output voltage pulse due to the collection of charge Q at the detector $V_{AMP} = A(Q/C)$, where $C = \left[C_D + C_A + (G+1)C_F\right] / G \cong C_F$, G is the voltage gain of the preamplifier input section (with feedback capacitance C_F), A is the combined voltage gain of the preamplifier (after the input section) and the amplifier, C_D and C_A are the capacitances to ground of the detector and the preamplifier input (including stray), respectively. This equation is derived for negative G. To follow convention,[99] $|G|$ is written as G. For G = 2000, (i.e., $|G| = 2000$), C_D = 80pf (as for thin detector), and C_A = 20 pf, $C = 1.01\ C_F$ and $V = 0.99\ A(Q/C_F)$.

In order to keep C_A small, the preamplifiers were located within 1 ft of the detectors. This was done by putting the preamplifiers in a watertight box that was attached to the top side of the detector chamber.

Each preamplifier was connected to an amplifier in a temperature controlled instrument room through a 200 ft length of RG-71 doubly shielded, 93 ohm coaxial cable. The multichannel pulse height analyzer and anticoincidence system were located in the same instrument room.

Block diagrams of the instrumentation are given in Figures 2 and 3. Details on the components are given in Tables 4 and 5.

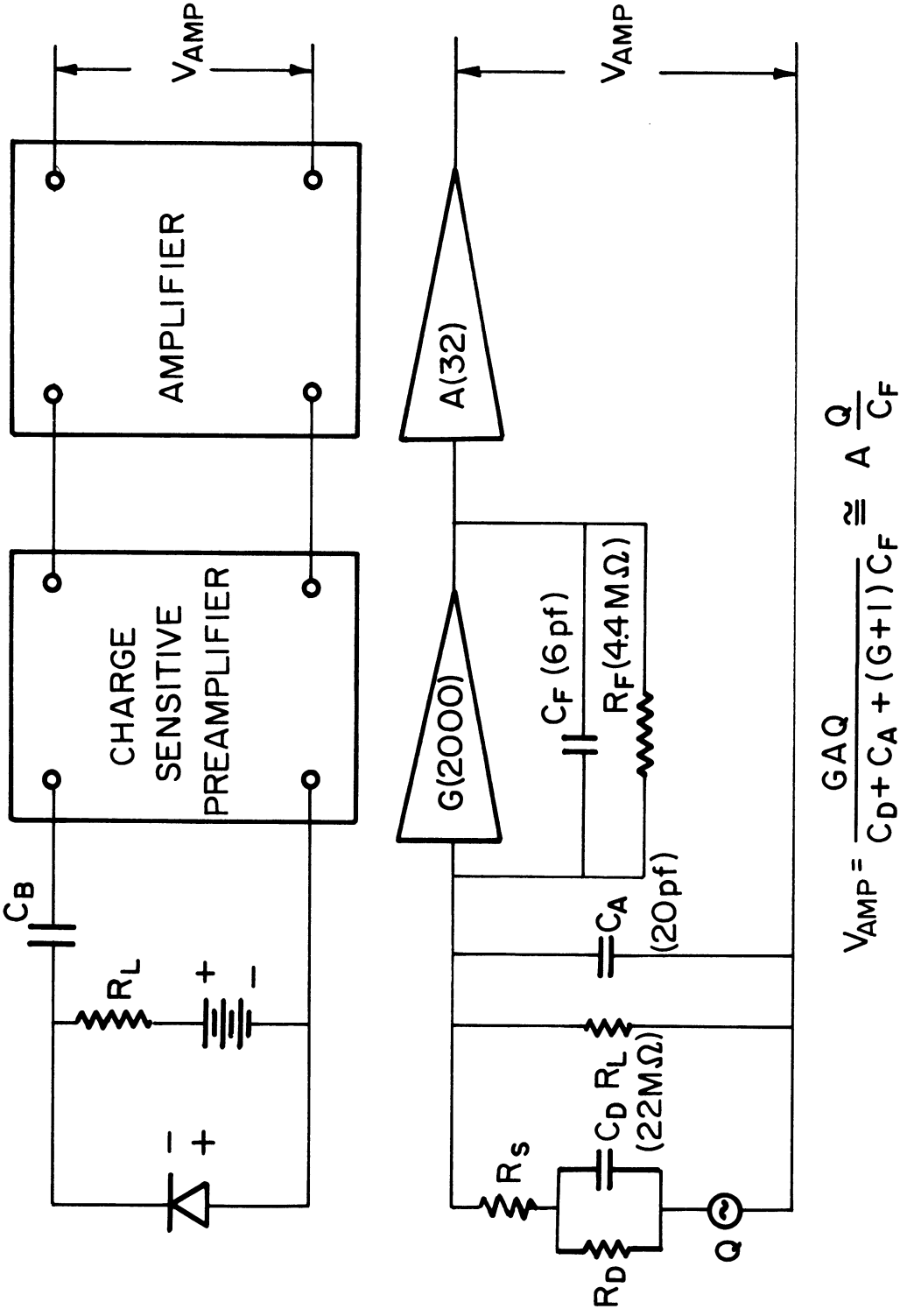

Figure 5. Block diagram and equivalent circuit for reverse-biased detector, charge-sensitive preamplifier, and amplifier.

TABLE 4

PROTON ENERGY ANALYSIS INSTRUMENTATION

Component	Manufacturer	Model
Preamplifier	Tennelec	100A
Amplifier	Nuclear Data	150F
Multichannel pulse height analyzer		
ADC	Nuclear Data	150F
Memory	Nuclear Data	150M

TABLE 5

ANTICOINCIDENCE INSTRUMENTATION

Component	Manufacturer	Model
Preamplifiers	Tennelec	100A
Amplifiers	Sturrup	101
Discriminators	Sturrup	501
Coincidence unit	Sturrup	1401
Gate unit	Nuclear Data	150F

D. SIGNAL-TO-BACKGROUND RATIO

Since low signal-to-background ratios (S/B) have been the principal limitation encountered in most measurements of reactor neutron spectra, the improvement of the S/B has been one of the main objectives in the development of this spectrometer system. Here the signal refers to those counts which result from neutrons entering the source end of the collimator, travel-

ing through the collimator without being scattered, and then scattering protons from the radiator to a detector which is thick enough to stop them. The background, as it is customarily defined, refers to all nonsignal counts.

1. Sources of Background

It is useful to consider the background as consisting of two components: nonsignal counts associated with the radiator and all other nonsignal counts. The latter component is measured by removing the radiator and is usually found to be the larger one. It is due to charged particles resulting from gamma and neutron interactions which occur within the detector and in the shielding and structural material in the vicinity of the detector. Data which indicates that gamma interactions within the detector dominate at higher energies and gamma interactions in material around the detector dominate at lower energies will be presented.

The nonsignal counts associated with the radiator are due to (1) protons scattered from the radiator with such high energy that they are not stopped in the detector, (2) carbon ions scattered from the CH_2 radiator by neutrons, and (3) protons scattered from the radiator by neutrons which either entered the collimator through the side wall rather than through the source end or entered the collimator through the source end, but were scattered in the collimator wall before reaching the radiator. The first case is designated as a nonsignal count because the measured proton energy is less than the energy of the proton incident on the detector. The third case, although not usually designated background in the literature, is designated such here because it does not qualify as

part of the above defined signal.

2. Design Considerations

As previously stated, most of the background counts usually result from gamma interactions within and near the detector. Hence, the spectrometer was specifically designed to reduce this source of backgound. The principal features are shown in Figure 1. This spectrometer has been operated with the source end of its collimator in fission gamma fields of 10^7 to 10^8 roentgens/hour.

The long, evacuated, conical collimator extracts a well-defined neutron beam from the reactor. It also allows the detector chamber to be far enough from the reactor core so that the pool water is an effective shield. The effectiveness of the water shielding was demonstrated by a measurement of the background count rate with the collimator removed. The measurement showed that only 10 to 20% of the background counts from 2 to 5 Mev are due to radiation which did not enter the detector chamber through the collimator.

The cylindrical steel and lead shields assist in the collimation of fission gammas. The desirability of this collimation is indicated in Figure 6. This figure shows the detector count rate without radiator as a function of the detector position above and below the collimator axis. This data was taken with only the lead shield installed. The background reduction by a factor of over a hundred along with a signal reduction of only 10% dictated the use of an off-axis detector position. The detector was positioned with its center 4.2 cm above the collimator axis and 10.2 cm

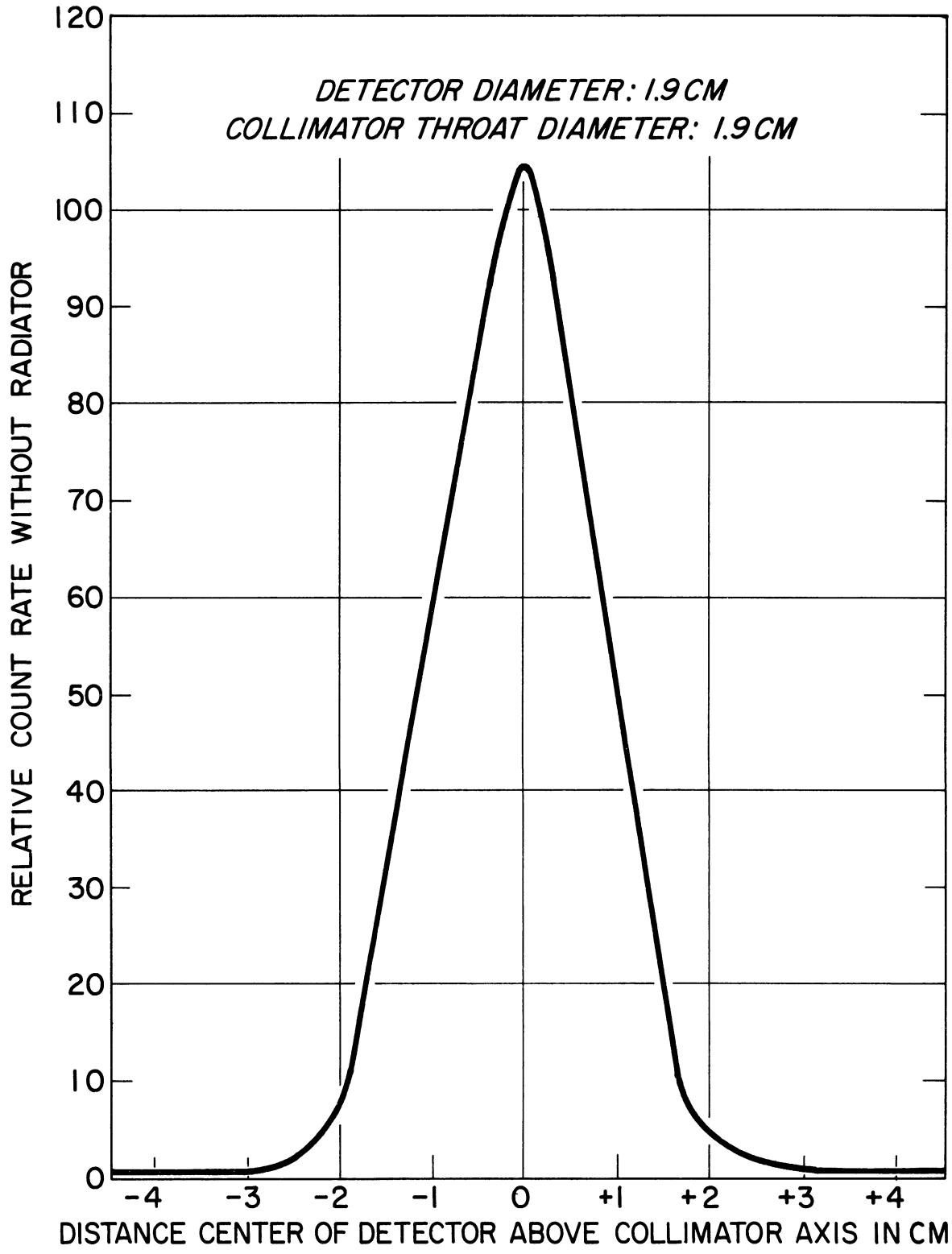

Figure 6. Background count rates for detector positions above and below collimator axis.

from the center of the radiator position. The resulting angle between the radiator-detector centerline and the collimator axis was 24°. As a result of the suggestion by Dr. F. C. Maienschein of ORNL to increase the thickness of the gamma shield, the steel shield was added. Its addition reduced the background counts from 2 to 5 Mev by 44%.

The electron filter is a 50-mil thick aluminum plate located over the front of the collimator throat to reduce the number of electrons streaming into the detector chamber. It reduces the background counts from 2 to 5 Mev by 36%. The charged particle baffle shields the detector from charged particles originating in the rear portion of the collimator throat. The beam trap reduces backscattering to the detector.

The radiator wheel is a thin brass plate with six equally spaced 2.1-cm diameter holes. They are slightly larger than the 1.9-cm diameter of the collimator throat. The wheel can be rotated and stopped so that the center of any one of the holes is aligned with the collimator axis. Various thickness polyethylene radiators can be mounted over these holes on the collimator side of the radiator wheel. For these measurements, only 1.25 mg/cm^2 and 2.95 mg/cm^2 thick CH_2 radiators were used. A blank wheel position was aligned with the collimator axis for the measurement of the background counts not associated with the radiator.

The evacuated detector chamber is much larger than that required to house the detector, radiator wheel, and motor. The extra volume provides free space around the detector to reduce charged particle events in material near the detector.

3. Influence of Detector Thickness

The limitation imposed by a low S/B is illustrated by the data of Figure 7. The S/B for this data and for data taken with 60 cm of water between the reactor core and collimator is shown in Figure 8. The lower S/B for the latter data indicates the background is dominated by gamma interactions since water attenuates fast neutrons (the signal) more than it does gammas (the background).

The S/B for the latter data also demonstrates that reliable data (i.e., S/B > 1) cannot be taken with this radiator-detector combination through 60 cm of water in the energy range from 2 to 5 Mev. Resolution considerations prohibit the use of a thicker radiator to improve the S/B in this energy region. An alternative is to use a thinner detector. The effect of using a detector of the same area but with its thickness reduced by a factor of four is shown in Figure 9. These curves show that the ratio of background counts for thick and thin detectors is equal to the ratio of their thicknesses at high energies but is much greater at lower energies. Thus, since the detector areas are equal, the background at high energies is proportional to the detector volume. This indicates gamma interactions within the detector are the main source of background at these energies. At the lower energies, the curves indicate the background is dominated by gamma interactions in material outside the detectors.

Data taken with the thin detector is shown in Figure 10. The coincidence spectrum shows the energy lost in the thin detector by protons which are not stopped in it. The anticoincidence system discussed earlier prevents

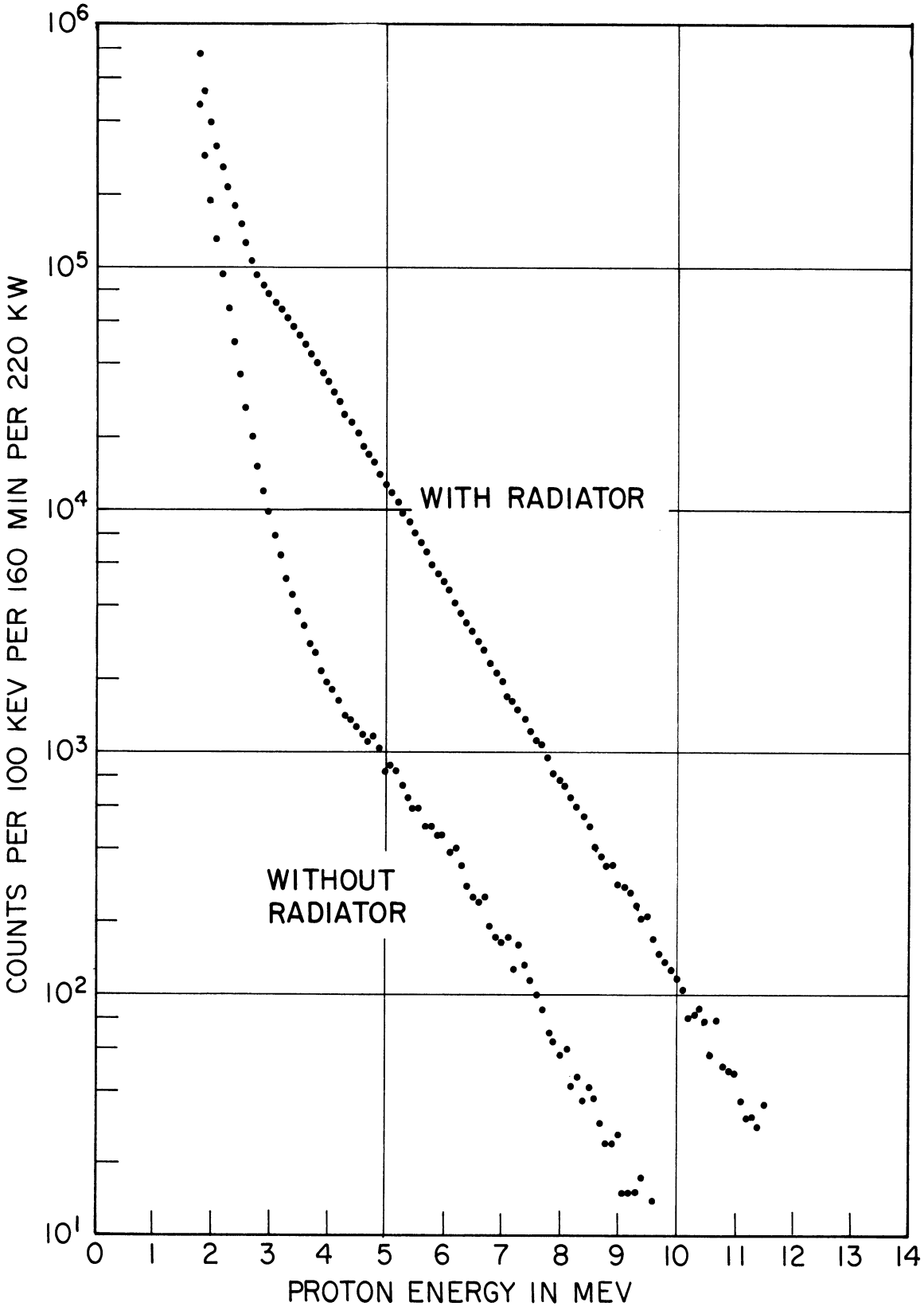

Figure 7. Proton recoil spectrum obtained using thick (1040 microns) detector and thick (2.95 mg/cm^2) radiator with collimator against reactor core.

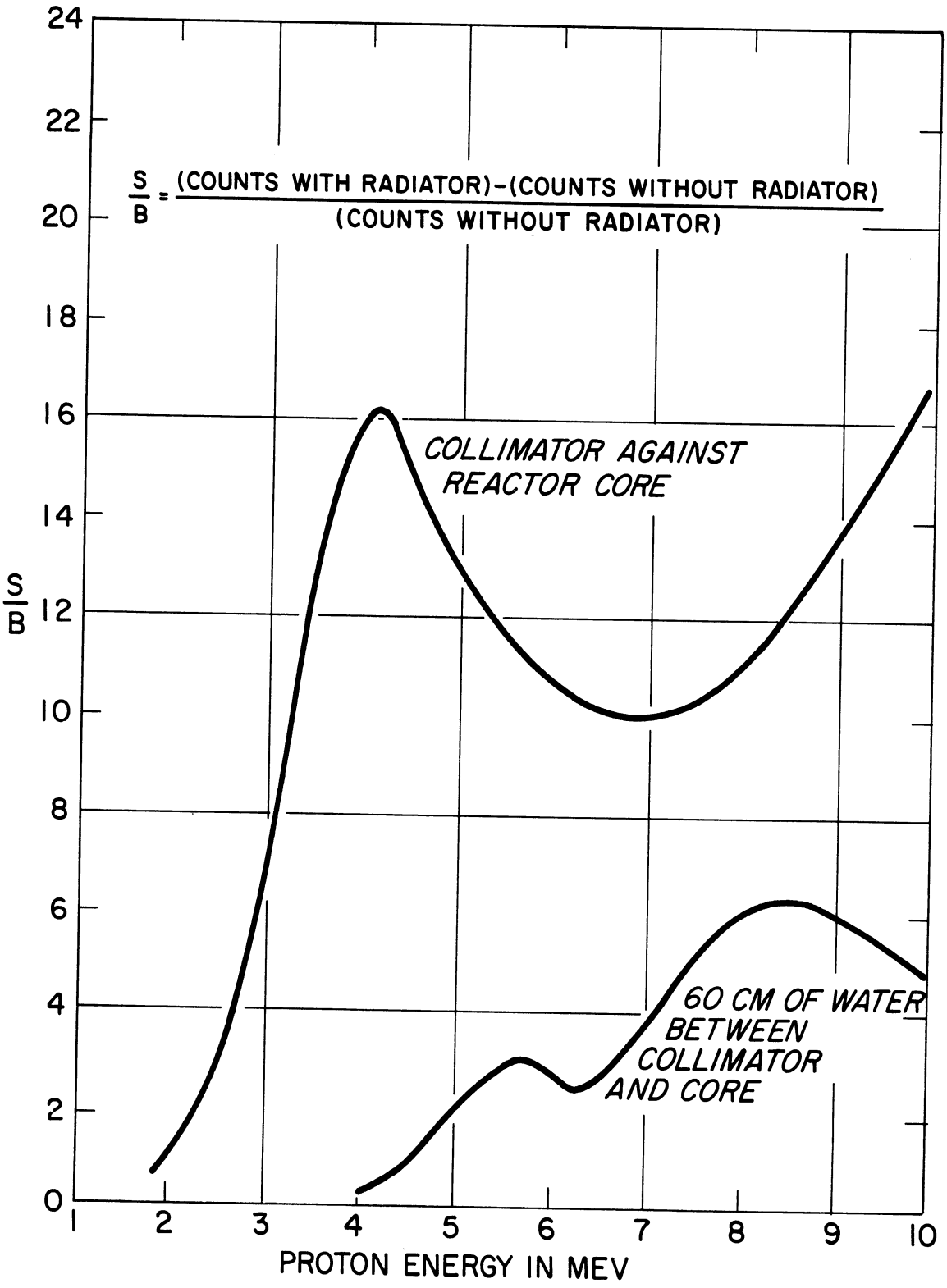

Figure 8. Signal-to-background ratios for proton recoil spectra obtained using thick (1040 microns) detector and thick (2.95 mg/cm^2) radiator.

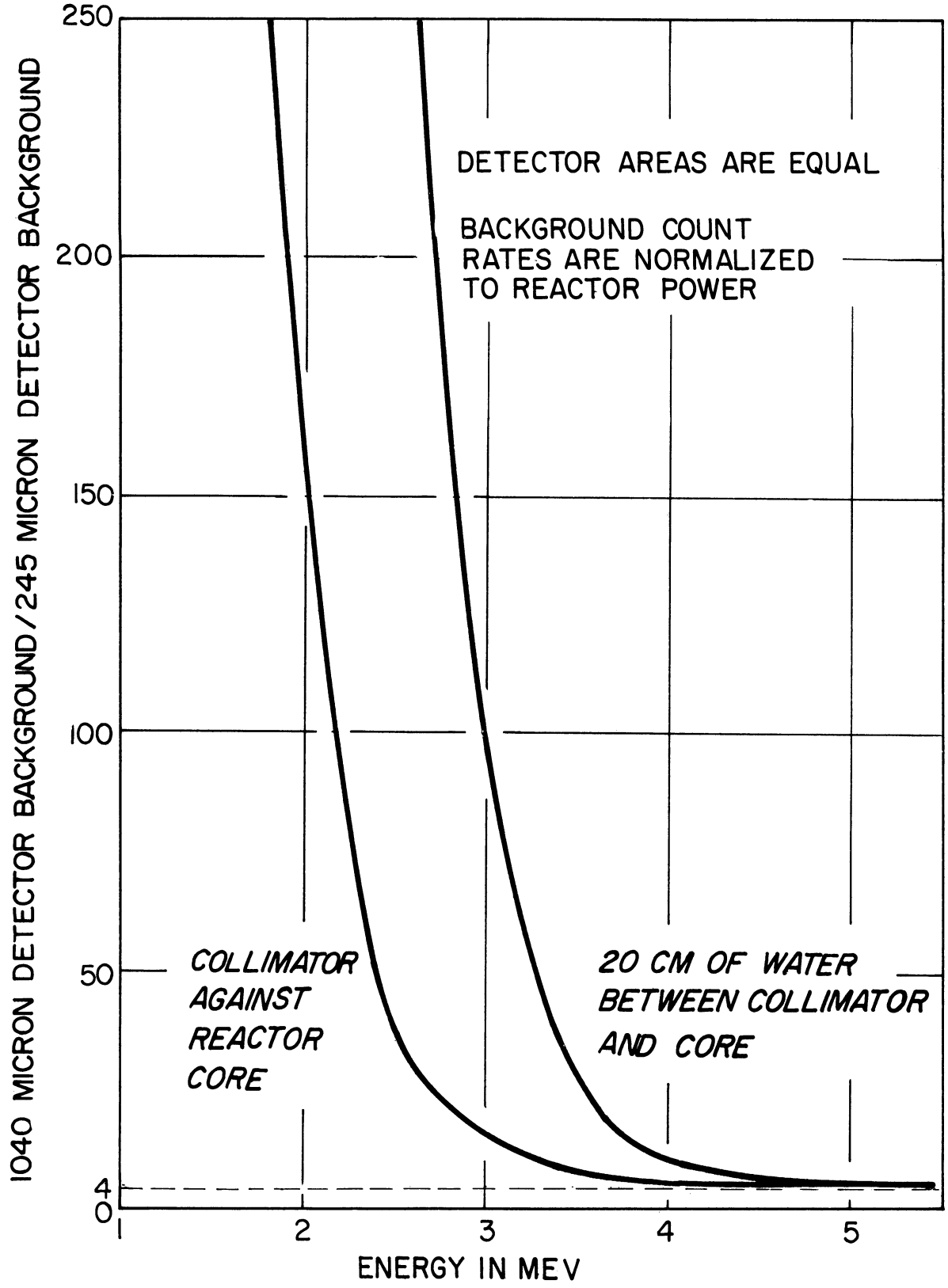

Figure 9. Ratio of thick detector background to thin detector backgound.

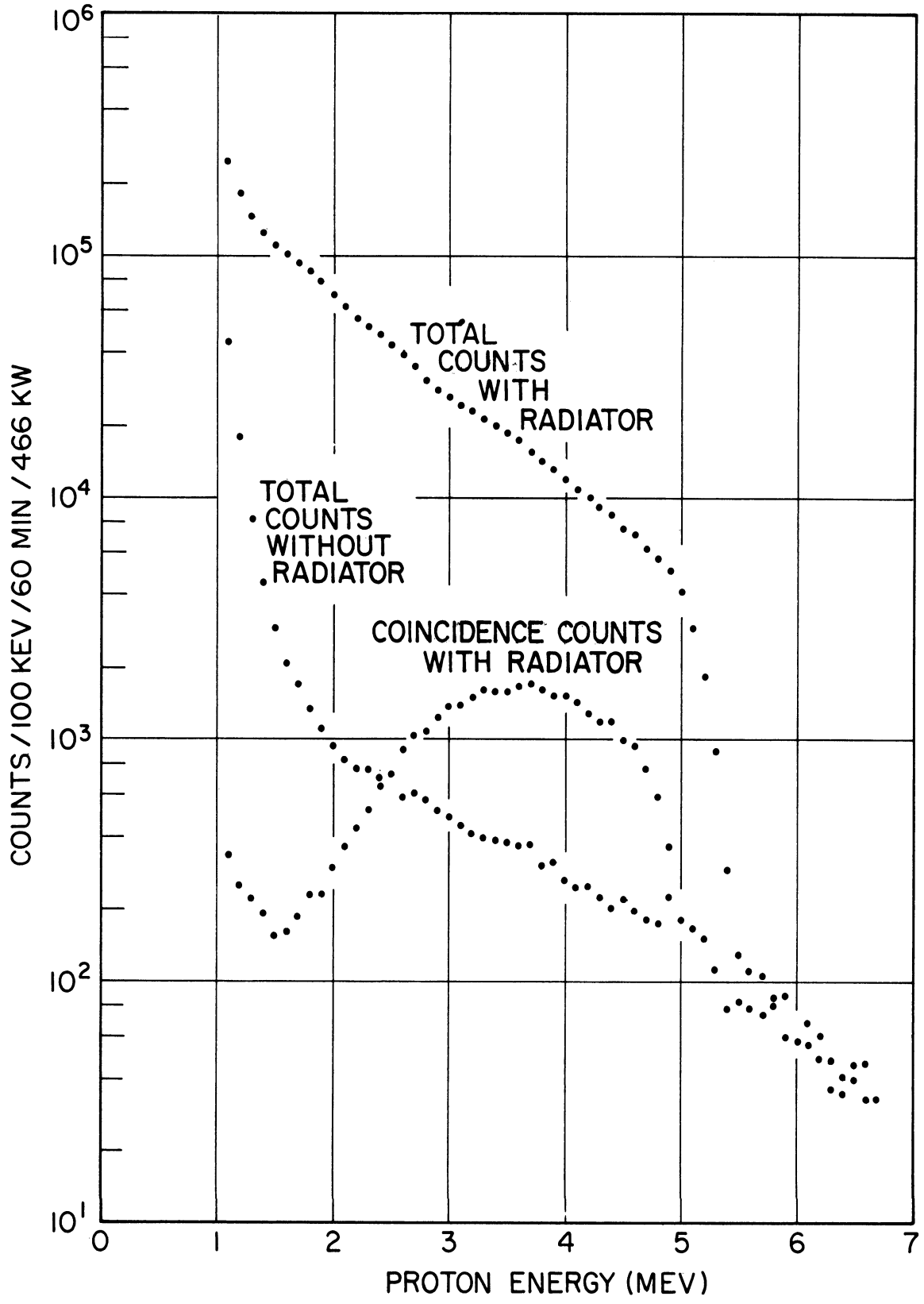

Figure 10. Proton recoil spectra obtained using thin (245 microns) detector and thin (1.25 mg/cm^2) radiator with collimator against reactor core.

these counts from being recorded. Alternately, they can be recorded separately as shown in Figure 10 and subtracted along with the counts recorded with the radiator removed. Use of the thin detector and anticoincidence system permits measurements above 2 Mev through 60 cm of water to be made with $S/B > 1$.

4. Carbon Recoils

It is shown in Appendix A that the background due to carbon recoils depends on the neutron energies of interest and on the shape of the spectrum being measured. For a hypothetical neutron spectrum which is constant from energy $4.24\ (E_C)^*_{min}$ to E_{max}, and zero thereafter, the maximum background occurs at the lowest neutron energy of interest, E_{min}. For the present measurements, E_{min} = 2 Mev and $(E_C)_{min}$ = 1.5 Mev. If E_{max} is 14 Mev, the maximum background due to carbon recoils is 4%, and if E_{max} is 18 Mev, it is 6%. These are conservative estimates, of course, since the actual measured spectra decrease rapidly with energy above the minimum energy, $4.24\ (E_C)_{min}$ = 6.36 Mev, required to scatter 1.5 Mev carbon recoils to the detector.

5. Collimator Effects

There are two effects which occur when the collimator walls are not black. First, some of the neutrons which exit the collimator entered it through the source end but were scattered in the collimator wall before reaching the exit. Secondly, some of the neutrons that reach the collimator exit initially entered the collimator through the side wall rather than

*The lowest carbon recoil energy of interest is $(E_C)_{min} = (E_p)_{min} = (E_{min}\ \overline{\cos^2\psi} - \delta E_p)$, and 4.24 is the ratio of the incident neutron energy to the carbon recoil energy.

through the source end. In Appendix B, these effects are estimated by use of a crude model to introduce 4.8% and 1.7% errors, respectively, when using the long conical collimator of this spectrometer.

Because the background due to carbon recoils and collimator effects is relatively small and the corrections are difficult to determine, no corrections were made for these measurements.

E. EFFICIENCY

The efficiency of the spectrometer can be defined either in terms of the neutron angular flux at the source end of the collimator or in terms of the neutron flux incident on the radiator. These two efficiencies, of course, differ only by the collimator efficiency.

For the first case, the total efficiency $\epsilon(E)$ is defined as the number of neutrons with energy E counted per unit time per unit neutron angular flux incident on the source end of the collimator and directed about the collimator axis toward the radiator:

$$\epsilon(E) \equiv \frac{C(E_p)\,dE_p}{\varphi(E)\,dE} \tag{2}$$

where:

$C(E_p)dE_p$ is the count rate in counts per sec due to protons which are scattered from the radiator to the detector by neutrons with energies in dE about E and which deposit energies in dE_p about E_p within the detector.

$\varphi(E)dE$ is the number of neutrons with energies in dE about E per sec

per cm^2 per steradian incident on the source end of the collimator and directed about the collimator axis toward the radiator.

For the second case, a similar expression is used to define $\epsilon_R(E)$, the number of neutrons with energy E which are counted per unit time per unit neutron flux incident on the radiator.

$$\epsilon_R(E) \equiv \frac{C(E_p)dE_p}{\varphi_R(E)dE} \tag{3}$$

where:

$\varphi_R(E)dE$ is the number of neutrons with energies in dE about E per sec per cm^2 directed about the collimator axis toward the radiator and incident on the radiator.

$\epsilon(E)$ and $\epsilon_R(E)$ are related by defining the collimator efficiency,

$$\epsilon_c \equiv \frac{\epsilon(E)}{\epsilon_R(E)} \tag{4}$$

In order to simplify the evaluation of ϵ_C and $\epsilon_R(E)$, the following assumptions are made:

a. The radiator is positioned over the exit end of the collimator.

b. The distance from the source end of the collimator to the exit end is large compared with the largest dimension of these two apertures.

c. The distance from the radiator to the detector is large compared with the largest dimension of these two components.

d. The anisotropy of n-p scattering in the center-of-mass system is negligible for the neutron energies of interest. (This is reasonable because n-p scattering is essentially 100% s-wave scattering up to 10 Mev and

is still 99% s-wave scattering at 14 Mev.)[100]

e. The radiator is sufficiently thin so that neutron attenuation and multiple n-p scattering are negligible.

From its definition,

$$\varepsilon_C = \Omega_C = \frac{A_C}{L_C^2} \quad \text{in steradians}$$

where:

Ω_C is the solid angle subtended at the radiator by the source end of the collimator in steradians.

A_C is the area of the source end of the collimator in cm^2.

L_C is the distance from the source end of the collimator to the radiator end in cm.

Also from its definition,

$$\varepsilon_R(E) = (N_R^H t_R A_R) \overline{\frac{d\sigma_{n\text{-}p}(E,\psi)}{d\Omega}} \Omega_D \quad \text{in } cm^2$$

where:

$(N_R^H t_R A_R)$ is the number of hydrogen atoms in the radiator.

N_R^H is the number of hydrogen atoms per milligram of radiator.

t_R is the thickness of the radiator in milligrams per cm^2.

A_R is the radiator area in cm^2.

$\overline{\frac{d\sigma_{n\text{-}p}(E,\psi)}{d\Omega}}$ is the differential cross section for neutrons with energy E to elastically scatter protons through the laboratory angle ψ with respect to the direction of the incident neutron, averaged with respect to ψ, in cm^2 per hydrogen atom per steradian.

$\Omega_D = \frac{A_D}{L_D^2}$ is the solid angle subtended at the radiator by the detector in steradians.

A_D is the area of the detector in cm^2.

L_D is the distance from the radiator to the detector in cm.

From assumption (d),

$$\overline{\frac{d\sigma_{n\text{-}p}(E,\psi)}{d\Omega}} = \frac{\sigma_{n\text{-}p}(E)\,\overline{\cos\psi}}{\pi}$$

where:

$\sigma_{n\text{-}p}(E)$ is the cross section for neutrons with energy E to elastically scatter protons in cm^2 per hydrogen atom.

$\overline{\cos\psi}$ is the cosine of the laboratory scattering angle, averaged with respect to ψ.

Combining these terms,

$$\varepsilon_R(E) = \frac{1}{\pi}\left(N_R^H t_R\right)\left(\frac{A_R A_D}{L_D^2}\right)\overline{\cos\psi}\;\sigma_{n\text{-}p}(E) \quad \text{in} \quad cm^2 \tag{5}$$

Taking the product $\epsilon_C\epsilon_R(E)$ to get the total efficiency,

$$\varepsilon(E) = \frac{1}{\pi}\left(N_R^H t_R\right)\left(\frac{A_C A_R A_D}{L_C^2 L_D^2}\right)\overline{\cos\psi}\;\sigma_{n\text{-}p}(E) \quad \text{in } cm^2 \text{ steradian} \tag{6}$$

An outstanding feature of these efficiency expressions is that the energy dependent term, $\sigma_{n\text{-}p}(E)$, is very well known ($< \pm 1\%$).[100] Figures 11 and 12 show $\epsilon_R(E)$ and $\epsilon(E)$ as calculated using the following constants:

$N_R^H = 0.86 \times 10^{20}$ H atoms/mg

$t_R = 1.25$ and 2.95 mg/cm^2

$A_C = \pi(5.1\text{ cm})^2 = 81.7\text{ cm}^2$

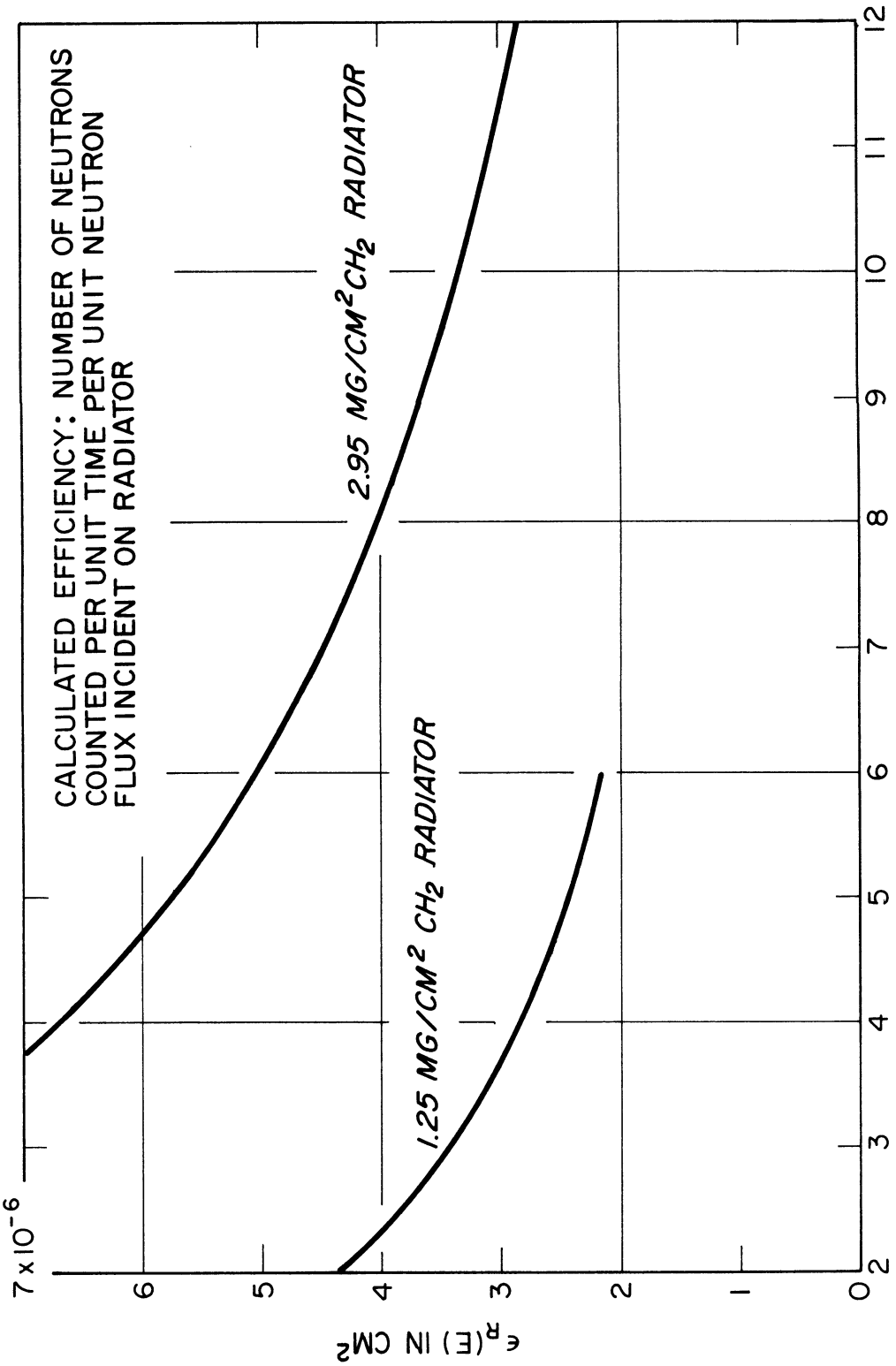

Figure 11. Calculated efficiency: $\epsilon_R(E)$.

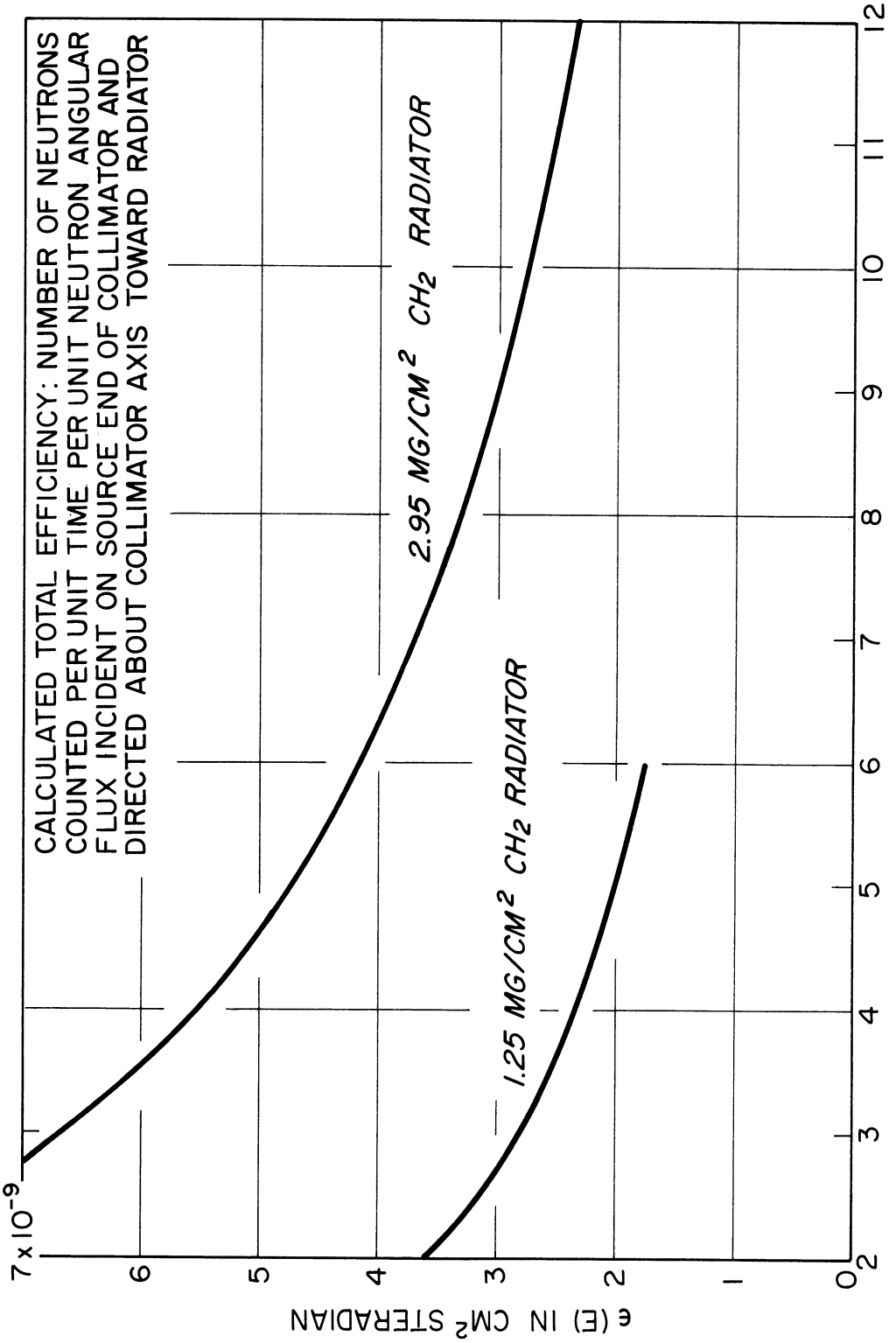

Figure 12. Calculated total efficiency: $\epsilon(E)$.

$A_R = \pi(0.95\ \text{cm})^2 = 2.84\ \text{cm}^2$

$A_D = \pi(0.75\ \text{cm})^2 = 1.77\ \text{cm}^2$*

$L_C = 315\ \text{cm}$

$L_D = 10.2\ \text{cm}$

$\overline{\cos\ \psi} = \int \cos\psi f(\psi)\ d\psi = 0.91$

$\overline{\cos^2\psi} = \int \cos^2\psi f(\psi)\ d\psi = 0.83$

$\overline{\sec\ \psi} = \int \sec\psi f(\psi)\ d\psi = 1.10$

The last two quantities are used to evaluate $E_p = E\ \overline{\cos^2\psi} - \delta E_p$ and $\delta E_p = (1/2)\int_0^{t_R} \overline{\sec\psi}\,(dE/dx)dx \cong (1/2)t_R\ \overline{\sec\psi}\ \left(\frac{dE}{dx}\right)_{E_p}$. The normalized scattering frequency, $f(\psi)d\psi$, is derived and evaluated in Section II-F-3.

From the definitions of $\epsilon_R(E)$ and $\epsilon(E)$, the differential fluxes

$$\phi_R(E) = \frac{C(E_p)}{\Sigma_R(E)\,dE/dE_p} \tag{7}$$

$$\phi(E) = \frac{C(E_p)}{\Sigma(E)\,dE/dE_p} \tag{8}$$

The differential count rate, $C(E_p) = N(E_p)/\Delta t\ \Delta E_p$, where $N(E_p)$ is the number of counts accumulated during Δt in the channel whose width is ΔE_p and whose midpoint is E_p. To find $\frac{dE}{dE_p}$, recall

$$E = \frac{E_p + \delta E_p}{\overline{\cos^2\psi}}$$

Thus,

$$\frac{dE}{dE_p} = \frac{1 + d(\delta E_p)/dE_p}{\overline{\cos^2\psi}}$$

where

$$\frac{d(\delta E_p)}{dE_p} \cong \frac{1}{2} t_R\ \overline{\sec\psi}\ \frac{d}{dE_p}\left(\frac{dE}{dx}\right)_{E_p}$$

*Detector area was measured by counting Am^{241} alphas with and without an aluminum mask (1.29 cm^2 aperture) in front of detector.

Since the latter derivative is negative,

$$\frac{dE}{dE_p} \cong \frac{1 - \frac{1}{2} t_R \overline{\sec\psi} \left| \frac{d}{dE_p} \left(\frac{dE}{dx}\right)_{E_p} \right|}{\overline{\cos^2\psi}} \tag{9}$$

This Jacobian was calculated and the results are shown in Figure 13.

F. ENERGY RESOLUTION

The spectrometer energy resolution is defined as $\Delta E/E$, where ΔE is the FWHM of the spectrometer response function for monoenergetic neutrons of energy E. Here the neutron energy $E = (E_p + \delta E_p)/\overline{\cos^2\psi}$. The resolution is found using the relation

$$\left(\frac{\Delta u}{u}\right)^2 = \left(\frac{1}{u}\right)^2 \sum_i \left(\frac{\partial u}{\partial x_i}\right)^2 (\Delta x_i)^2$$

where $u = u(x_1, x_2, x_3, \ldots)$. Thus,

$$\left(\frac{\Delta E}{E}\right)^2 = \left(\frac{\Delta E_p}{E \overline{\cos^2\psi}}\right)^2 + \left[\frac{\Delta(\delta E_p)}{E \overline{\cos^2\psi}}\right]^2 + \left[\frac{\Delta(\cos^2\psi)}{\overline{\cos^2\psi}}\right]^2 \tag{10}$$

The three terms are due to variations of (1) the proton detector response, (2) the proton energy losses in the radiator, and (3) the n-p scattering angle, respectively. Each term will be discussed in order.

1. Detector Term

The detector term, $\Delta E_p / E \overline{\cos^2\psi}$, is the smallest and is negligible at all but low energies (6% at 2 Mev, 3% at 4 Mev). Table 3 gives ΔE_α as 30 and 40 Kev for the thick and thin detectors, respectively, in an evacuated test chamber. When they are installed in the spectrometer and it is submerged in the reactor pool as it is during normal operation, ΔE_α of both

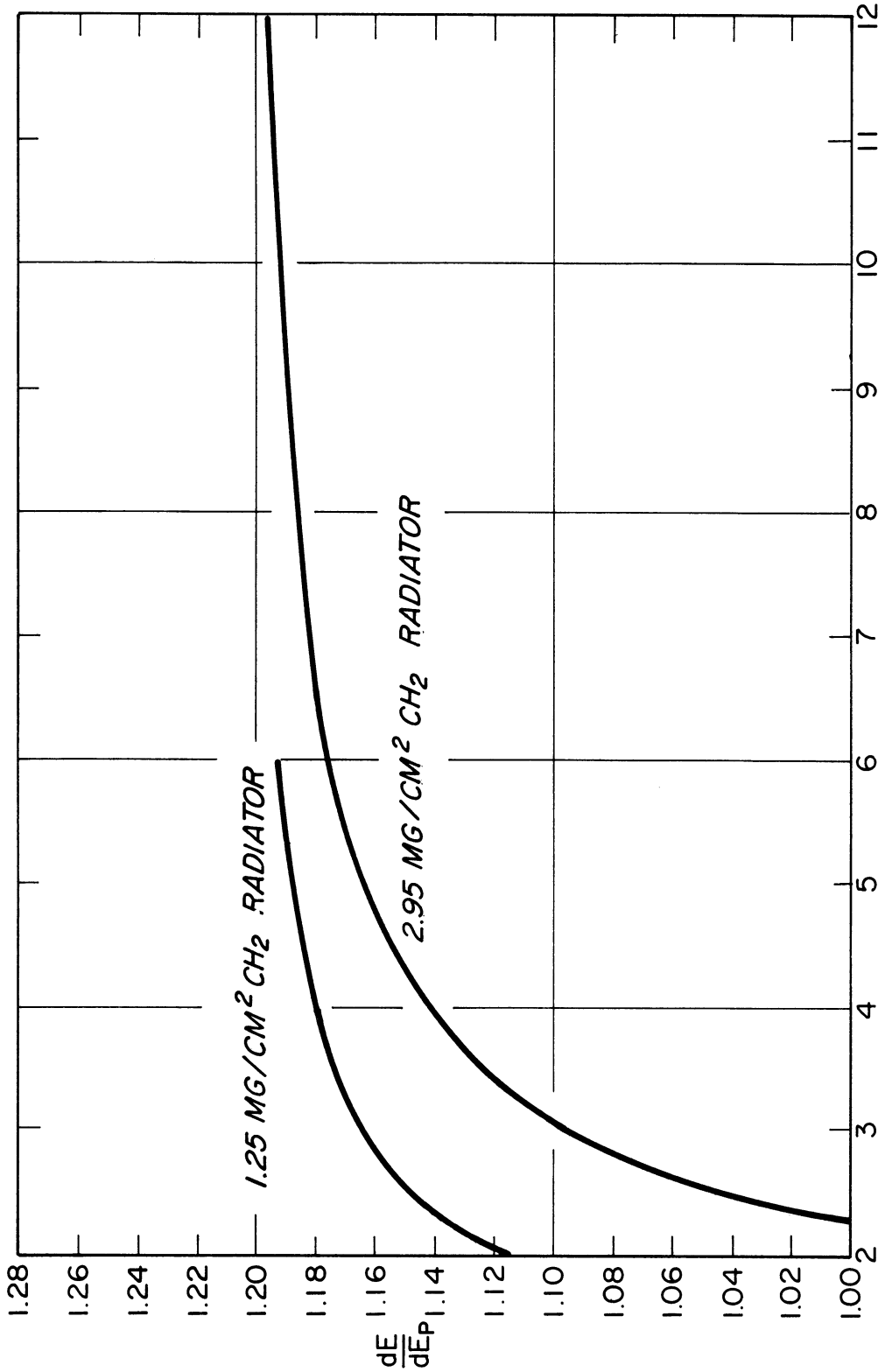

Figure 13. Calculated energy Jacobian: dE/dE_p.

detectors increases to about 60 Kev. This increase is probably due to ground loops. Also, ΔE_α increases to 140 Kev during some periods. During the same periods, a one megacycle ripple is observed on the preamplifier output. The appearance of this ripple has been found to correspond to the broadcasting time of a local, daytime radio station which transmits at 1.05 megacycles. Since spectrum measurements were taken about equally during day and night, an average ΔE_α is 100 Kev. This value is used for ΔE_p. As before, $\overline{\cos^2\psi} = \int \cos^2\psi f(\psi) d\psi = 0.83$. Hence, $\Delta E_p / E \overline{\cos^2\psi} = 120 \text{ Kev}/E$.

2. Radiator Term

The radiator term, $\Delta(\delta E_p)/E \overline{\cos^2\psi}$, is the dominant term at low energies, but becomes negligible at high energies. It can be estimated by neglecting the variations in ψ and assuming all protons are scattered through some mean angle $\overline{\psi}$. Then the response function is a rectangular function whose maximum energy is $E \cos^2\overline{\psi}$ and whose minimum energy is $E \cos^2\overline{\psi} - \int_0^{t_R \sec\overline{\psi}} (dE/dx)dx$. Thus, the width of this rectangular function is $\Delta(\delta E_p) = \int_0^{t_R \sec\overline{\psi}} (dE/dx)dx \cong t_R \sec\overline{\psi} (dE/dx)_{E_p}$. Replacing $\sec\overline{\psi}$ by $\overline{\sec\psi} = \int \sec\psi \, f(\psi) \, d\psi = 1.10$, $\Delta(\delta E_p) = 2 \, \delta E_p$ and $\Delta(\delta E_p)/E \overline{\cos^2\psi} \cong 2.41 \, \delta E_p / E \cong 1.32 \, t_R \left(\frac{dE}{dx}\right)_{E_p} / E$.

3. Geometry Term

The last term, $\Delta(\cos^2\psi)/\overline{\cos^2\psi}$, is called the geometry term because it is determined primarily by the scattering angles allowed by the collimator-radiator-detector geometry. However, it also depends on the angular dependence of the n-p scattering cross section. As before, the scattering is

assumed to be isotropic in the CMCS. Also, the neutrons are assumed to be normally incident on the radiator. The small angular divergence of the long, conical collimator makes the latter assumption very good. Thus, the geometry term is determined by the radiator-detector geometry and the cosine of the laboratory scattering angle. This term is independent of neutron energy, and it is the dominant term at high energies.

$\Delta(\cos^2\psi)$ is the FWHM of the normalized distribution function $f(\cos^2\psi)$, where $f(\cos^2\psi)d(\cos^2\psi) = f(\psi)\, d\psi$ and $f(\psi)d\psi$ is the fraction of the counts due to protons scattered in $d\psi$ about ψ.

To find $f(\psi)$, consider a beam of neutrons normally incident on the differential radiator area, dA_R, shown in Figure 14. The resulting current of protons scattered in $d\psi$ about ψ from dA_R to the differential detector area, dA_D, is

$$J_p(E,r,\theta,\psi)dE dA_R d\Omega_D = J_n(E,r,\theta)dE dA_R N_R^H t_R \frac{d\sigma_{n\text{-}p}(E,\psi)}{d\Omega} d\Omega_D$$

where: $J_n(E, r, \theta)dEdA_R$ is the number of neutrons with energies in dE about E which are normally incident on dA_R per second. $J_p(E, r, \theta, \psi)$ $dEdA_R d\Omega_D$ is the number of protons elastically scattered by neutrons with energies in dE about E from dA_R into $d\Omega_D$ per second.

$$d\Omega_D = \frac{S(r,\theta,\psi)R\, d\psi}{R^2} = \frac{S(r,\theta,\psi)\cos\psi\, d\psi}{H}$$

Assuming

$$\frac{d\sigma_{n\text{-}p}(E,\psi)}{d\Omega} = \frac{\sigma_{n\text{-}p}(E)\cos\psi}{\pi}$$

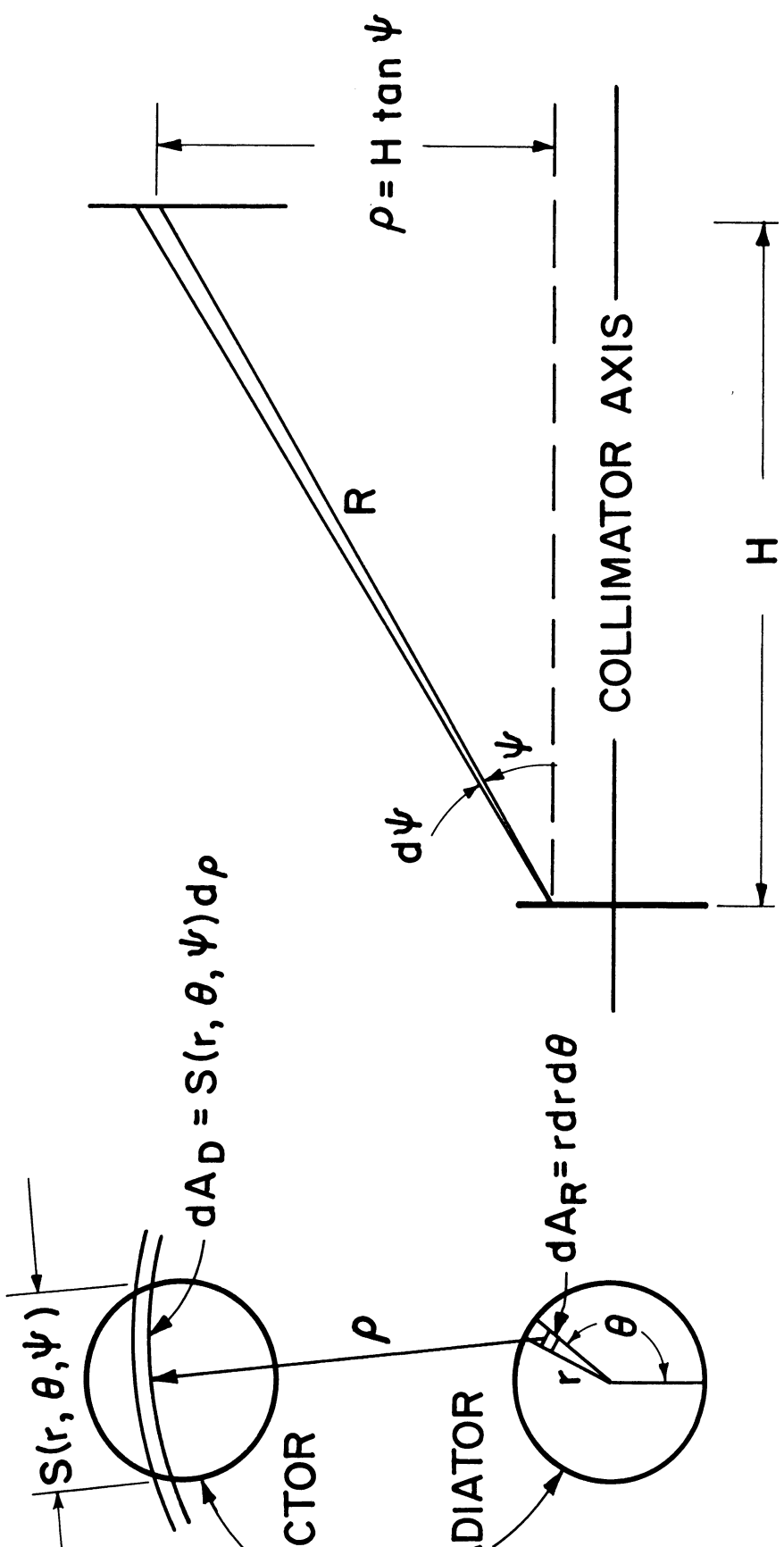

Figure 14. Radiator-detector geometry used for calculation of $f(\psi)$ and $f(\cos^2\psi)$.

and

$$J_n(E,r,\theta) = J_n(E)\,F(r,\theta)$$

$$J_p(E,r,\theta,\psi)\,dE\,dA_R\,d\Omega_D = (N_R^H t_R/\pi H)\,\sigma_{n\text{-}p}(E)\,J_n(E)\,dE\,F(r,\theta)\,S(r,\theta,\psi)\,dA_R\,\cos^R\psi\,d\psi$$

Define:

$$J_p(E,\psi)\,dE\,d\psi \equiv \int_{A_R} J_p(E,r,\theta,\psi)\,dE\,d\Omega_D\,dA_R$$

$$S(\psi) \equiv \frac{1}{A_R}\int_{A_R} F(r,\theta)\,S(r,\theta,\psi)\,dA_R$$

Substituting,

$$J_p(E,\psi)\,dE\,d\psi = (N_R^H t_R A_R/\pi H)\,\sigma_{n\text{-}p}(E)\,J_n(E)\,dE\,S(\psi)\,\cos^R\psi\,d\psi$$

Define:

$$P(E,\psi)\,d\psi \equiv \frac{J_p(E,\psi)\,dE\,d\psi}{J_n(E)\,dE}$$

$$P(E,\psi)\,d\psi = (N_R^H t_R A_R/\pi H)\,\sigma_{n\text{-}p}(E)\,S(\psi)\,\cos^R\psi\,d\psi$$

But,

$$f(\psi)\,d\psi \equiv \frac{P(E,\psi)\,d\psi}{\int P(E,\psi)\,d\psi}$$

$$f(\psi)\,d\psi = \frac{S(\psi)\,\cos^R\psi\,d\psi}{\int S(\psi)\,\cos^R\psi\,d\psi}$$

$$f(\psi)\,d\psi = Z\,S(\psi)\,\cos^R\psi\,d\psi$$

where the normalization constant

$$Z = \left[\int S(\psi)\,\cos^R\psi\,d\psi\right]^{-1}$$

To find $f(\cos^2\psi)$, recall $f(\cos^2\psi)\,d(\cos^2\psi) = f(\psi)\,d\psi$. Since $d(\cos^2\psi) = -2\cos\psi\sin\psi\,d\psi$,

$$f(\cos^2\psi) = -(Z/2)\,S(\psi)\cot\psi\,d\psi$$

The determination of $f(\psi)$ and $f(\cos^2\psi)$ requires $S(\psi)$. The function $S(\psi)$ must be evaluated for a specific radiator-detector geometry and a

given $F(r,\theta)$. Here it is assumed that $F(r,\theta) = F(r)$. Thus,

$$S(\psi) = \frac{1}{A_R} \int_{\theta} \int_{r} F(r)\, S(r,\theta,\psi)\, r\, dr\, d\theta$$

This integral is evaluated by the following graphical-numerical method. Draw to scale the front view of the radiator and detector shown in Figure 14. Then draw concentric circles within the radiator that divide it into m equal areas. Next, draw radii which divide each of the m areas into n equal areas. This procedure is illustrated in Figure 15 for m=3 and n=12. Each of the resulting mn = 36 areas is equal. Due to the symmetry, only the 18 areas in the right half of the radiator are used. Arcs with radii which correspond to various values of ψ are swung from the centers of these areas to intercept the detector area. From Figure 14, the arc radius, $\rho(\psi) = H \tan \psi$. Figure 15 shows arcs drawn from area (m,n) =(3,5) for integral values of ψ. The intercept of $\rho(24^\circ)$ with the detector area is $S(r_3, \theta_5, 24^\circ)$. A set of arcs with radii corresponding to integral values of ψ was drawn for each of the radiator areas (m,n). The length of each intercept with the detector area was measured to get $S(r_m, \theta_n, \psi)$. Using these values of $S(r_m, \theta_n, \psi)S(\psi) = (\Delta A_R/A_R) \sum_{m,n} F(r_m)\, S(r_m, \theta_n, \psi)$,

where $(\Delta A_R / A_R) = (1/18)$,

Thus, $$f(\psi) = (2/18) \cos^2\psi \sum_{m,n} F(r_m)\, S(r_m, \theta_n, \psi)$$

and $$f(\cos^2\psi) = -(2/36) \cot\psi \sum_{m,n} F(r_m)\, S(r_m, \theta_n, \psi)$$

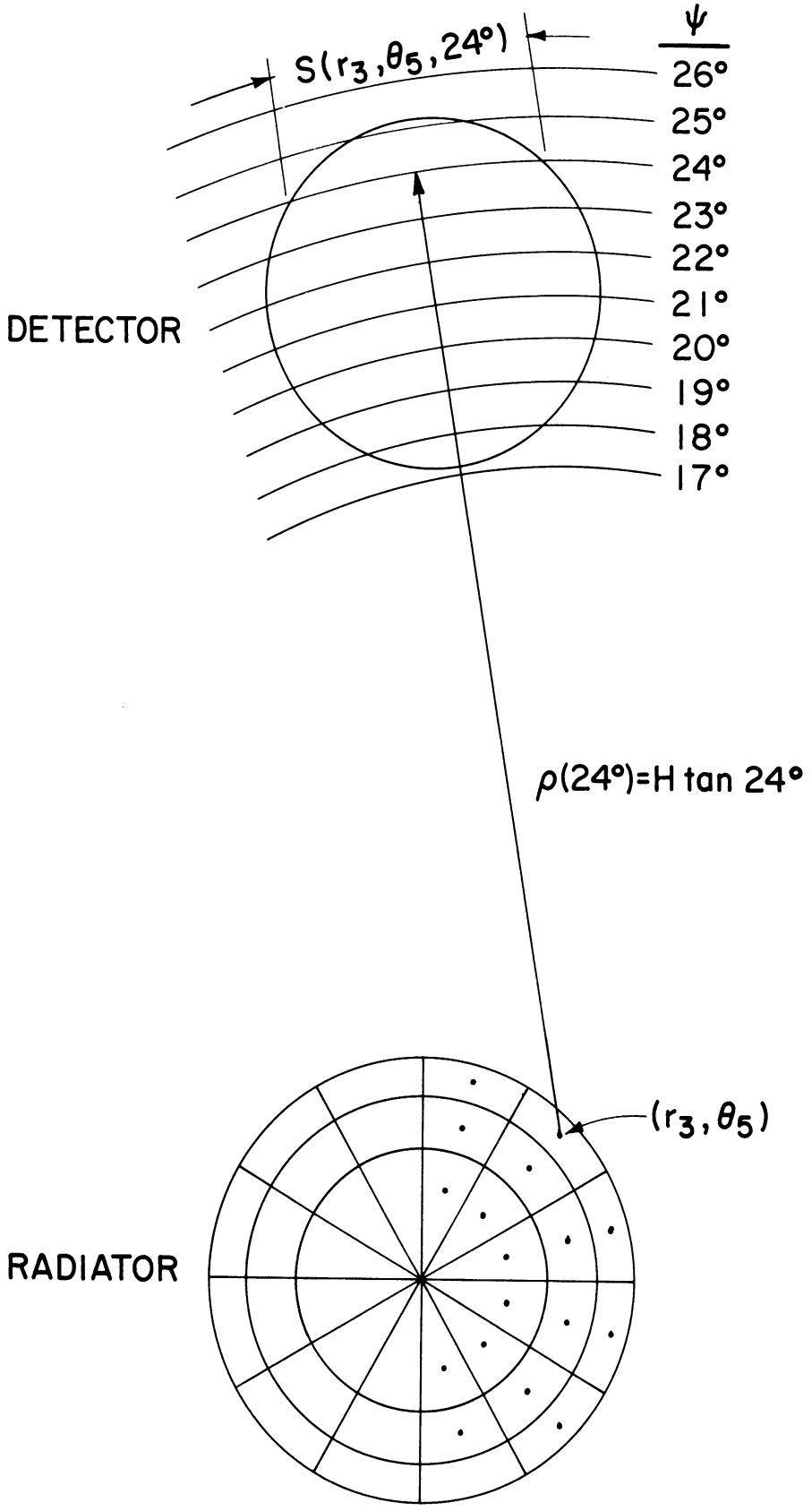

Figure 15. Example of construction used for calculation of $S(\psi)$.

The latter function was evaluated and plotted. The FWHM of this function is $\Delta(\cos^2\psi)$. It was evaluated for three cases to find the influence of the radial function $F(r_m)$. The results are shown in Table 6.

TABLE 6

INFLUENCE OF $F(r_m)$ ON $\Delta(\cos^2\psi)$

Case	$F(r_1)$	$F(r_2)$	$F(r_3)$	$\Delta(\cos^2\psi)$	$\frac{\Delta(\cos^2\psi)}{\cos^2\psi}$
I	0.333	0.333	0.333	0.108	0.130
II	0.500	0.333	0.167	0.100	0.120
III	1.000	0	0	0.083	0.100

The function, $f(\cos^2\psi)$ is shown in Figure 16 as calculated for case II. Due to the cylindrical collimator throat, the $F(r_m)$ used for this case is expected to be a good estimate of the actual $F(r_m)$. The results shown in the table indicate that the uncertainty in $\Delta(\cos^2\psi)$, introduced by the uncertainty in $F(r_m)$, is less than 10%. The average values of $\cos\psi$, $\cos^2\psi$, and $\sec\psi$ calculated using $f(\psi)d\psi$ are relatively insensitive to the choice of $F(r_m)$.

4. System Resolution

The detector, radiator, and geometry terms are combined to get the system resolution as follows.

$$\frac{\Delta E}{E} = \left[\left(\frac{0.120\ \text{MeV}}{E}\right)^2 + \left(\frac{2.41\ \delta E_p}{E}\right)^2 + (0.120)^2\right]^{\frac{1}{2}} \qquad (11)$$

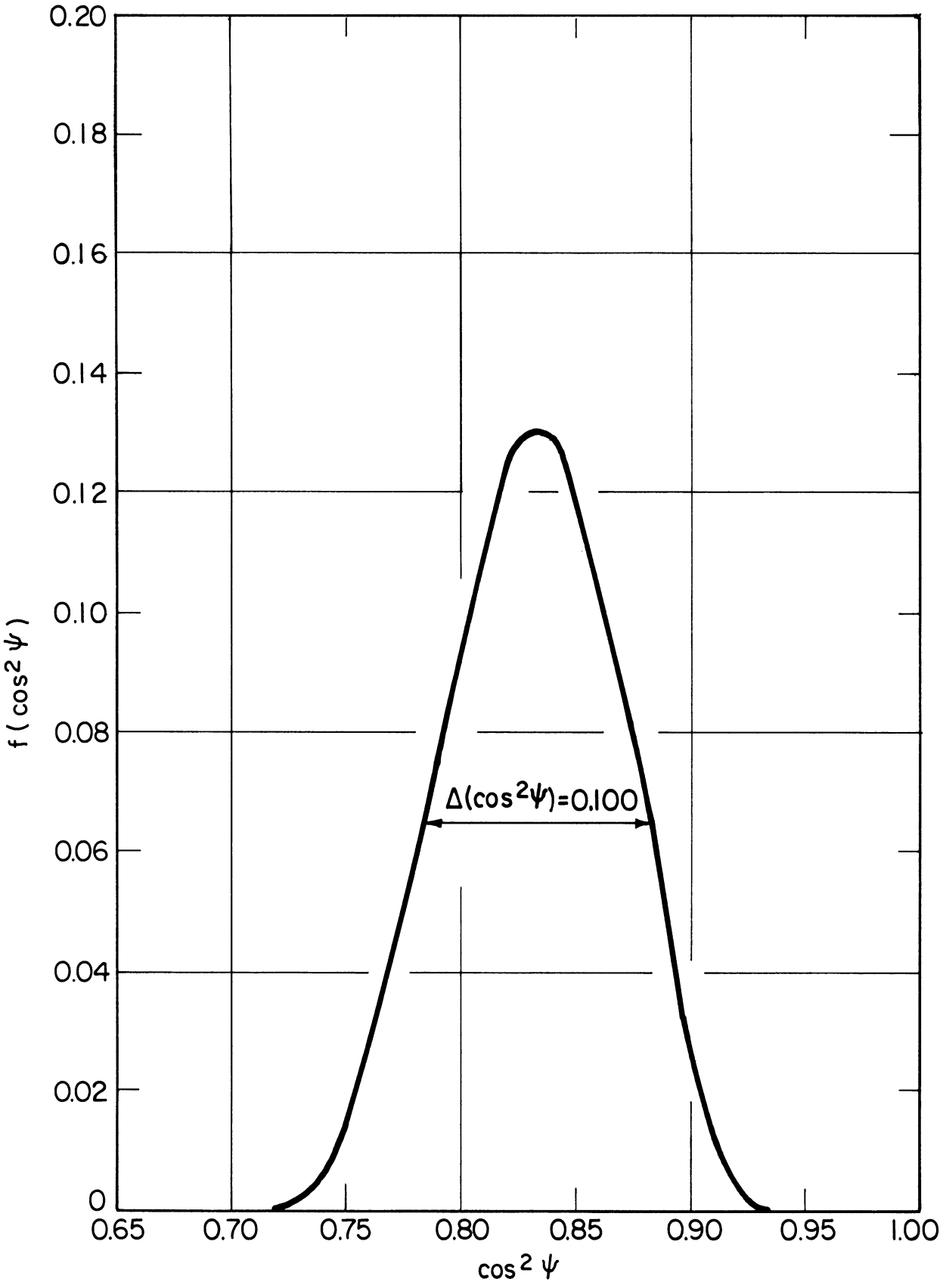

Figure 16. Calculated distribution function: $f(\cos^2\psi)$.

The resolution (i.e., FWHM in per cent) is shown as a function of neutron energy in Figure 17 for the two radiator thicknesses used. Due to the better resolution at low energies, the thin radiator is used with the thin detector for neutron energies from 2 to 6 Mev. The thick radiator and thick detector are used together for neutron energies from 4 to 12 Mev.

5. Influence on Measurement

The effect of the spectrometer resolution on measured neutron spectra depends on the FWHM and shape of the resolution function and on the shape of the neutron spectra. Since the fission spectrum decreases approximately exponentially at high energies, it is of interest to know how the resolution influences the measurement of an exponential spectrum. To estimate this effect, the resolution function is assumed to be Gaussian. Thus the measured spectrum,

$$\varphi_m(E) = \int_{-\infty}^{\infty} \varphi(E') P(E', E)\, dE'$$

where

$$\varphi(E') = \varphi_0 e^{-\alpha E'}$$

$$P(E', E) = \frac{1}{\sqrt{2\pi}\,\sigma(E)} e^{-\frac{(E'-E)^2}{2\sigma^2(E)}}$$

Using $R = \Delta E/E$ and $\sigma(E) = \Delta E/2.355 = RE/2.355$, evaluation of the integral gives

$$\frac{\varphi_m(E)}{\varphi(E)} = e^{\left(\frac{\alpha R E}{3.33}\right)^2} \qquad (12)$$

For $\alpha = (1.290\ \text{Mev})^{-1} = 0.7752\ \text{Mev}^{-1}$ and $R = 0.12$, $\varphi_m(E)/\varphi(E) = 1.03$ for $E = 6$ Mev and 1.12 for $E = 12$ Mev.

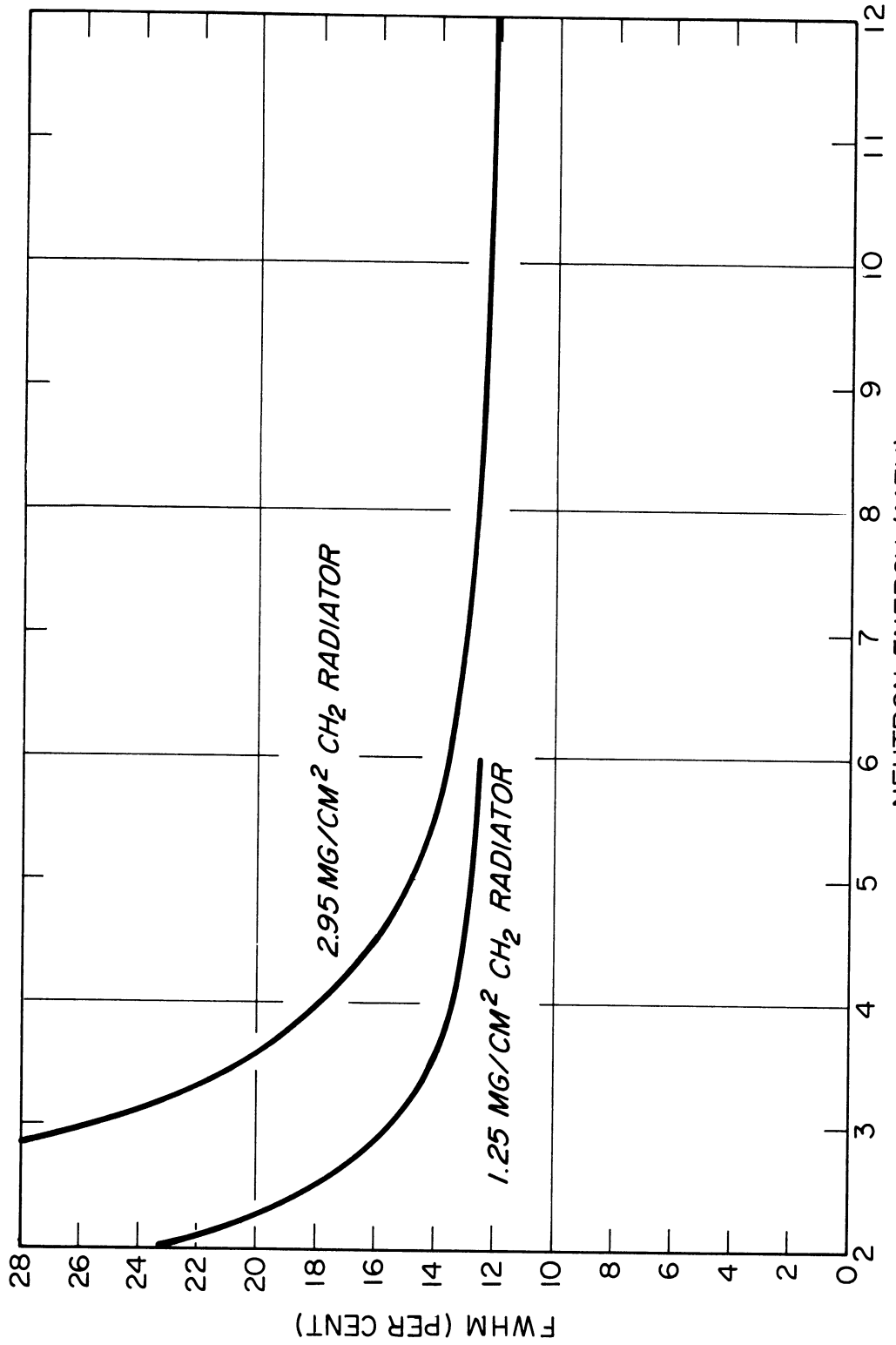

Figure 17. Calculated energy resolution: $\Delta E/E$.

The slope of the measured spectra is

$$\frac{Q'_m(E)}{Q_m(E)} = -\alpha + \left(\frac{\alpha R}{2.355}\right)^2 E \qquad (13)$$

Using the same α and R,

$$\frac{Q'_m(E)}{Q_m(E)} = -0.7654\ \text{Mev}^{-1} = -(1.306\ \text{Mev})^{-1} \quad \text{for } E = 6\ \text{Mev}$$

$$= -0.7565\ \text{Mev}^{-1} = -(1.322\ \text{Mev})^{-1} \quad \text{for } E = 12\ \text{Mev}$$

For comparison, the slope of the actual spectrum is

$$\frac{Q'(E)}{Q(E)} = -\alpha = -0.7752\ \text{Mev}^{-1} = -(1.290\ \text{Mev})^{-1} \quad \text{for } E > 0$$

The above ratios show the spectrometer resolution causes the measured flux to be greater than the actual flux at a given energy, and the slope of the measured spectrum to be less than that of the actual spectrum.

The influence of a change or uncertainty in the resolution on the measured slope is given by the following relation.

$$\frac{\Delta(Q'_m/Q_m)}{(Q'_m/Q_m)} = -\left[\frac{2}{(5.55/\alpha E R^2) - 1}\right]\frac{\Delta R}{R} \qquad (14)$$

Using the same α and R again,

$$\frac{\Delta(Q'_m/Q_m)}{(Q'_m/Q_m)} = -0.024\left(\frac{\Delta R}{R}\right) \quad \text{for } E = 6\ \text{Mev}$$

$$= -0.049\left(\frac{\Delta R}{R}\right) \quad \text{for } E = 12\ \text{Mev}$$

Thus, a 10% change or uncertainty in the resolution results in a change or uncertainty in the measured slope in the opposite sense by less than 0.5%.

G. ENERGY RANGE

As has been indicated, the energy range of the spectrometer is from 2 to 12 Mev. The lower limit is determined by two factors. First, the signal-to-background ratio, which increases with decreasing energy, drops below one at about 2 Mev for most of the measured spectra. Secondly, the resolution becomes poorer at lower energies. The upper limit is also determined by two factors. The low efficiency and the few neutrons with energies above 10 Mev result in poor statistics at these energies unless very long counting times are used. Also, the detector must be thicker than the range of the highest energy protons of interest.

The above considerations indicate the complex nature of the spectrometer energy range. It depends on the thickness and geometry of the radiators and detectors, and on the intensity and energy dependence of both the source and the background.

CHAPTER III

EXPERIMENTAL RESULTS

A. FORD NUCLEAR REACTOR

The spectrum measurements in water and graphite were made in the Ford Nuclear Reactor (FNR) pool using core leakage neutrons as the fast neutron source.

1. Reactor Description

The FNR is an open pool type research reactor operated at power levels up to 2 megawatts at The University of Michigan. It is very similar to the Bulk Shielding Reactor I (BSR-I) at Oak Ridge National Laboratory. The volume fractions of the standard fuel element are 0.2% uranium (95% U^{235}), 41.6% aluminum, and 58.2% water. The H_2O serves as moderator, coolant, reflector, and shield. The reflector system also includes a tank of D_2O on the north core face and graphite reflector elements on other faces. Different core configurations were used for the water and graphite measurements. The two configurations are shown in Figure 18.

2. Reactor Power Measurement

The measured spectra were normalized to reactor power. Reactor power was measured by stopping the secondary coolant flow while the reactor was operating at a steady state power level and observing the rate at which the pool water temperature increased as the primary coolant water returned to the pool. The average reactor power,

$$P = mc_p \frac{\Delta T}{\Delta t}$$

where $\Delta T/\Delta t$ is the rate of the pool water temperature increase, m is the mass of the water in the pool and the primary cooling system, and c_p is the

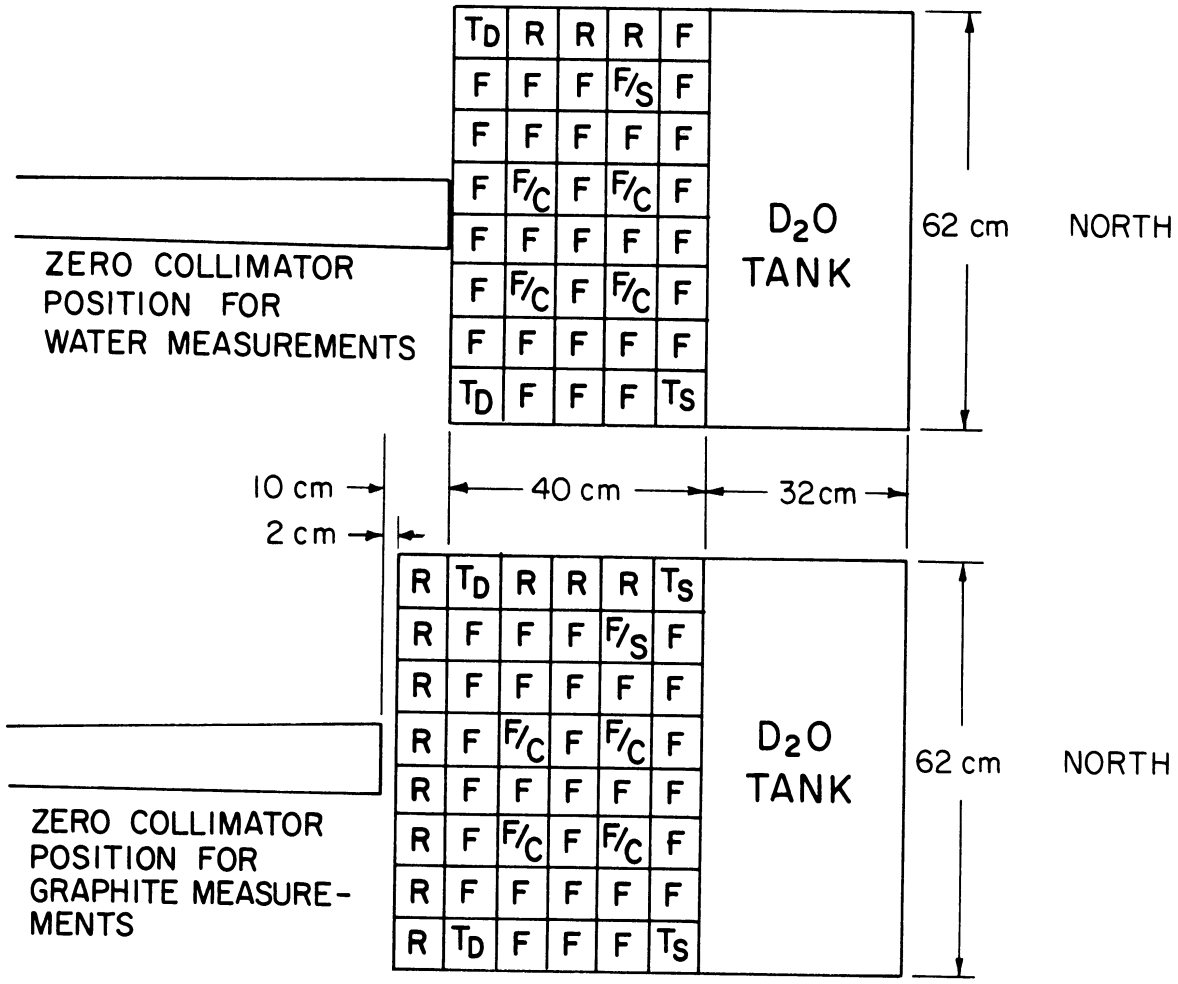

F FUEL ELEMENT (FUEL HEIGHT: 60 cm)
R REFLECTOR ELEMENT (GRAPHITE)
F/S FUEL ELEMENT WITH CENTRAL CHANNEL FOR SAMPLES
F/C FUEL ELEMENT WITH CONTROL ROD IN CENTRAL CHANNEL
T_S TUBE FOR SAMPLES
T_D TUBE FOR DETECTOR DURING REACTOR STARTUP

Figure 18. Ford Nuclear Reactor core configurations.

specific heat of water. For the FNR, $(1/mc_p)$ = 8.65°F/megawatt hour. This method assumes (1) nonfission heat sources are negligible, (2) heat losses are negligible, and (3) the pool water is mixed thoroughly. These assumptions are apparently valid and the method is quite reliable and accurate (±5%).(101)

B. WATER MEASUREMENTS

As indicated in Figure 18, the spectrum measurements were made on the south side of the core. The spectrometer was submerged in the reactor pool and the collimator axis was aligned with the north-south core centerline. A photograph of the spectrometer suspended above the pool is shown in Figure 19. Figure 20 shows the submerged collimator 60 cm from the south core face. The demineralized pool water ranged from 35°C to 43°C during the measurements.

1. Normalization

In order to reduce the influence of flux shifts within the core, due for instance to control rod withdrawal during xenon buildup, the spectrum measurements were normalized directly to the fast neutron leakage flux from the south core face. The spectra were then normalized to reactor power by relating the leakage flux to a single calorimetric measurement of reactor power for the same core configuration used during the spectrum measurements.

The fast neutron leakage flux was monitored by activating aluminum wires and counting the Al^{27} (n,α) Na^{24} reaction* product gammas (1.37 and

*This reaction was used because its threshold is in the Mev range (3.26 Mev)(26) and the half life of its product is well known (±0.13%)(102) and much longer than the half lives of other reaction products present. The other reactions are the Al^{27} (n,p) Mg^{27} reaction with threshold at 1.89 Mev and the Al^{27}(n,γ) Al^{28} reaction. The half life of Na^{24} is 14.97 hours whereas the half lives of Mg^{27} and Al^{28} are 9.4 minutes and 2.3 minutes, respectively. Hence, the activated aluminum wires can be allowed to decay until the only significant reaction product remaining is Na^{24}. The effect of Na^{23} (n,γ) Na^{24} reactions which result from thermal neutron capture by sodium impurities in the aluminum wires was minimized by using high purity aluminum and by covering the aluminum with 10 mil cadmium.

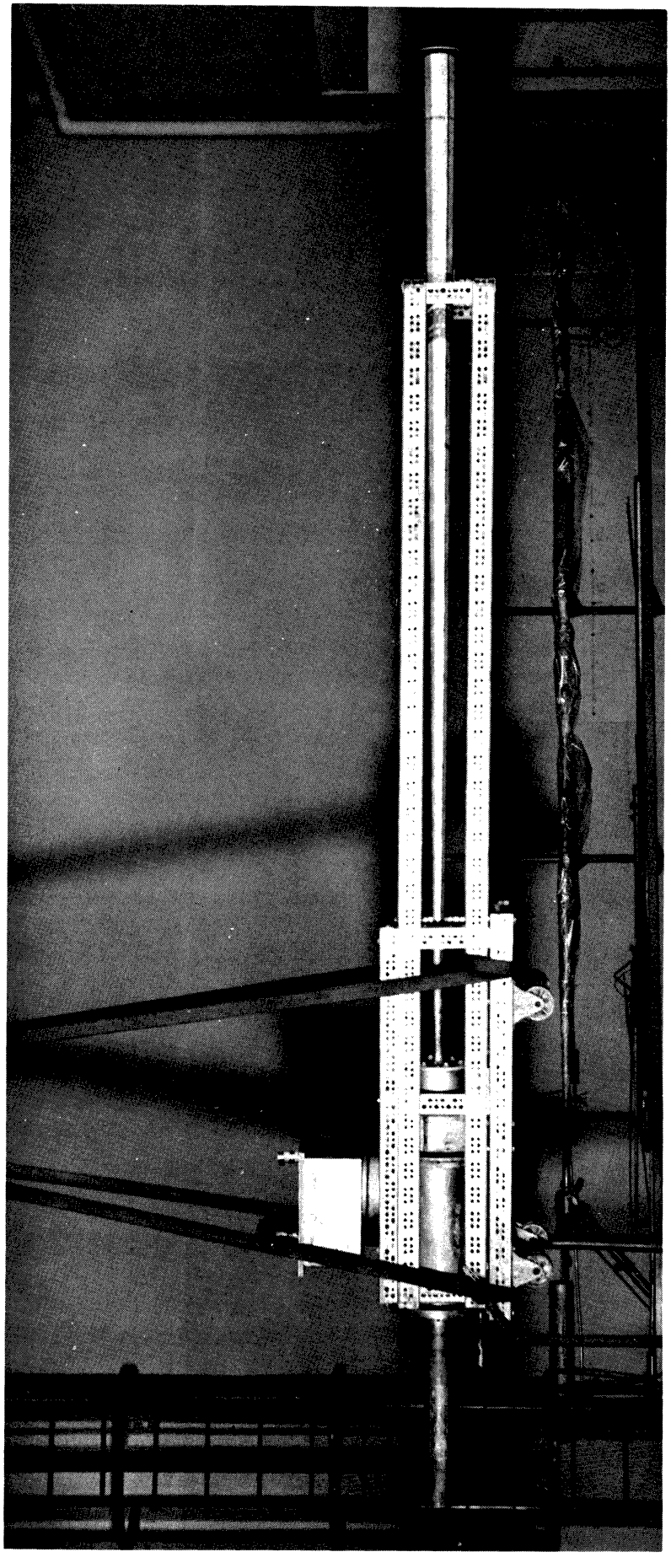

Figure 19. Spectrometer suspended above FNR pool.

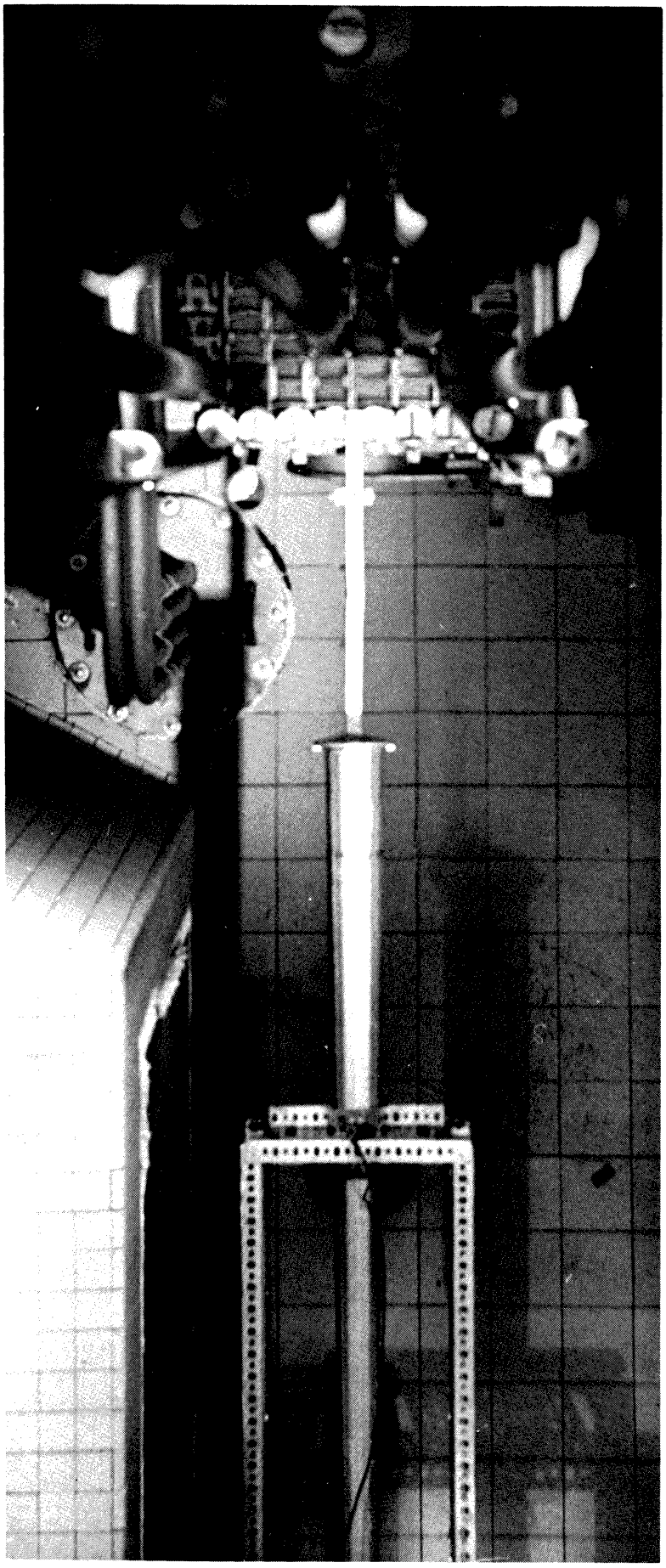

Figure 20. Collimator positioned 60 cm from FNR core.

2.75 Mev) with a 3" x 3" NaI (Tl) crystal. Four wires were positioned 30 cm from the core for each activation. The wires were mounted at 90° intervals on the circumference of a ring (30-cm diameter) that was centered on the north-south core centerline. With the wires in these positions, it was found that when the collimator was against the core, the aluminum activation was approximately 33% higher than it was without the collimator present. This undesirable perturbation was negligible at the other collimator positions, but did introduce an estimated ±5% uncertainty in the normalized amplitude of the zero spectrum measurement.

2. Reactor Power

The FNR was operated at 2 megawatts for all of the measurements except those with the collimator against the core. The latter measurements were made at 0.2 and 0.5 megawatt using the thick detector and thin detector, respectively. The lower power levels were used to limit the counting rates and thus reduce pile-up distortion. This distortion was monitored by observing the width of the Am^{241} alpha peak. Negligible broadening ($< 10\%$) was observed at the power levels used.

3. Counting Times and Statistics

The water measurements were made during a four-week period. The initial measurements were made with the collimator against the reactor core. For the measurements from 2 to 6 Mev made using the thin detector and thin radiator, three 20-minute foreground counts and three 20-minute background counts were taken in alternating sequence. After the zero spectrum was measured, measurements were made with the collimator 20, 40, and finally 60 cm from the reactor core. The measurement from 4 to 12 Mev for the 60-cm spectrum, made using the thick detector and thick radiator, required the longest counting time. Here six 10-hour foreground counts and six 5-hour background counts were taken in alternating sequence.

Due to the few number of neutrons at the higher energies, the statis-

tical uncertainties were largest at these energies. At 10 Mev the standard deviation (sigma) of a single point varied from 3.2% to 6.0%, and at 12 Mev it ranged from 6.5% to 12.9%.

4. Measured Spectra

A machine plot of the measured spectra of FNR leakage neutrons which penetrated 0, 20.0, 40.0, and 60.0 cm of pool water is shown in Figure 21. Each measured point was obtained by subtracting the normalized background counting rate (without radiator) from the normalized foreground counting rate (with radiator). Then, as indicated by Equation (8), the resulting counts per second per Mev of proton energy per megawatt of reactor power were divided by the total efficiency in cm^2 steradian and by the energy Jacobian in Mev of neutron energy per Mev of proton energy. The resulting angular flux is expressed in neutrons per second per cm^2 per Mev (of neutron energy) per steradian (directed normally to the south core face) per megawatt (of reactor power).

The semilog plot of Figure 21 is characterized by three principal features. First, the FNR leakage spectrum falls off exponentially above 5 Mev as the fission spectrum does. Secondly, the attenuation of lower energy neutrons is much greater than that of the higher energy neutrons due primarily to the higher elastic scattering cross section of hydrogen at the lower energies. Thirdly, the progressively deepening dip in the spectra at about 3.5 Mev is due to the elastic scattering resonance of oxygen at that energy. The scatter of the data at the higher energies is due to

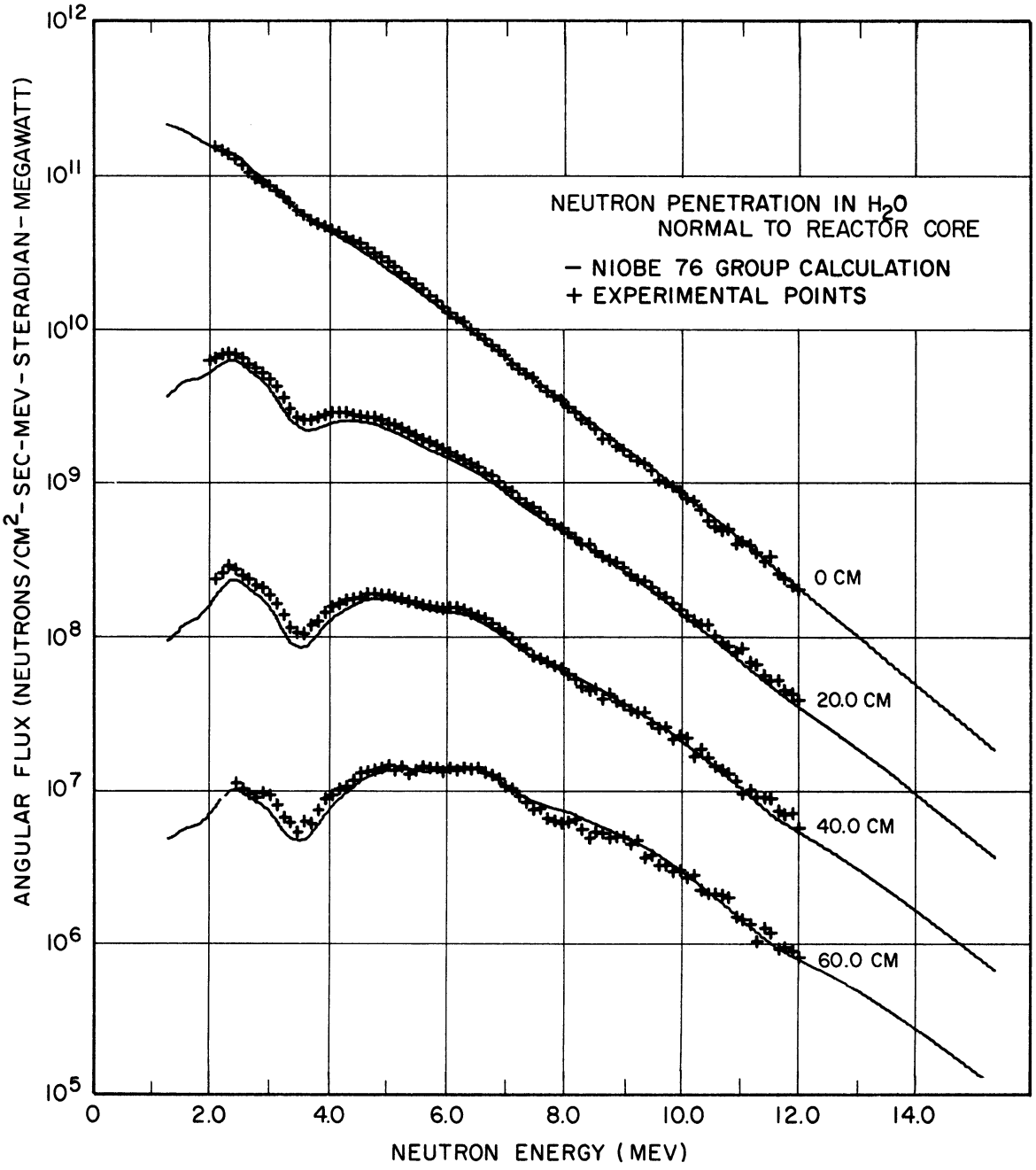

Figure 21. Neutron penetration in water.

counting statistics. The calculated spectra shown in Figure 21 are discussed in Chapter IV.

5. Experimental Uncertainties

The principal experimental uncertainties are summarized in Table 7. The uncertainties associated with the background were limited by restricting the reported data to that with signal-to-background ratios above one. Even so, with the collimator effects included, these uncertainties may be as high as ± 10% at 2 Mev.

The influence of the spectrometer resolution was to convolute the actual spectra with the spectrometer response function, i.e., the measured spectra are averaged over the energy width of the response function. The averaging process results in loss of spectral detail and, as shown in Chapter II for an exponential spectrum like the fission spectrum above 5 Mev, the slope of the spectrum may be modified. The importance of the latter effect in determining the slope of the fission source spectrum is discussed in Chapter IV.

Excluding these resolution effects, the total relative and total absolute uncertainties in the amplitudes of the measured spectra are typically ±10% and ±20%, respectively. Counting statistics increase these percentages somewhat at neutron energies above 10 Mev, and background uncertainties make them slightly higher at neutron energies near 2 Mev.

The ±2% uncertainty in the spectrometer energy calibration is due mainly to the uncertainties in the mean squared cosine of the n-p scatter-

TABLE 7

PRINCIPAL EXPERIMENTAL UNCERTAINTIES

A. Proton Recoil Spectra Measurement

Detector Energy Calibration: ± 1%

*Background: Avg. ± 3%, Max. ± 10% at 2 Mev

*Counting Statistics: Avg. ± 3%, Max. ± 13% at 12 Mev for water
Max. ± 23% at 12 Mev for graphite

B. Conversion from Proton Spectra to Neutron Spectra

Spectrometer Energy Calibration (includes detector): ± 2%

Efficiency: ± 5%

C. Normalization

Reactor Power Measurement: ± 5%

*Aluminum Activation: ± 2% except ± 5% for 0 cm water

D. Shield Geometry

*Thickness: ± 1.5%, ± 0.75%, ± 0.5% for 20, 40, 60 cm water
± 0.5% for graphite

*Density: ± 0.2% for water
± 2% for graphite

E. Spectrometer Resolution

*Denotes uncertainties associated with relative measurements.

ing angle ($\overline{\cos^2\psi} = 0.83 \pm 0.01$) and the mean energy required for protons to generate an electron-hole pair in silicon ($\epsilon_p = \epsilon_\alpha \pm 1\%$).

C. GRAPHITE MEASUREMENTS

The graphite measurements were made with graphite slabs mounted against the south core face.

1. Description of Graphite Slabs

The graphite was high density, fine grained, HLM grade (Great Lakes Carbon Corp.). Its measured density* was 1.74 ± 0.04 grams/cm^3. Each slab was 20.2 cm x 62.5 cm x 62.5 cm. These dimensions include the 0.635-cm thick 6061 aluminum plate which completely encased each slab to keep it dry while submerged in the FNR pool. Two views of four of the slabs fabricated for this experiment are shown in Figure 22. Figure 23 shows three of the slabs positioned against the south core face during measurements at 2 megawatts. The collimator axis was aligned with the north-south core centerline as for the water measurements. The graphite slabs were suspended from above the reactor pool. The tube attached to the top side of each slab was provided for off-gassing.**

---

*The supplier specified an average density of 1.72 grams/cm^3 for this grade

**Little off-gassing was observed except from the slab nearest the core for a short period after the reactor reached full power. This was probably due to thermal expansion of air within the graphite as gamma heating increased the temperature of the graphite.

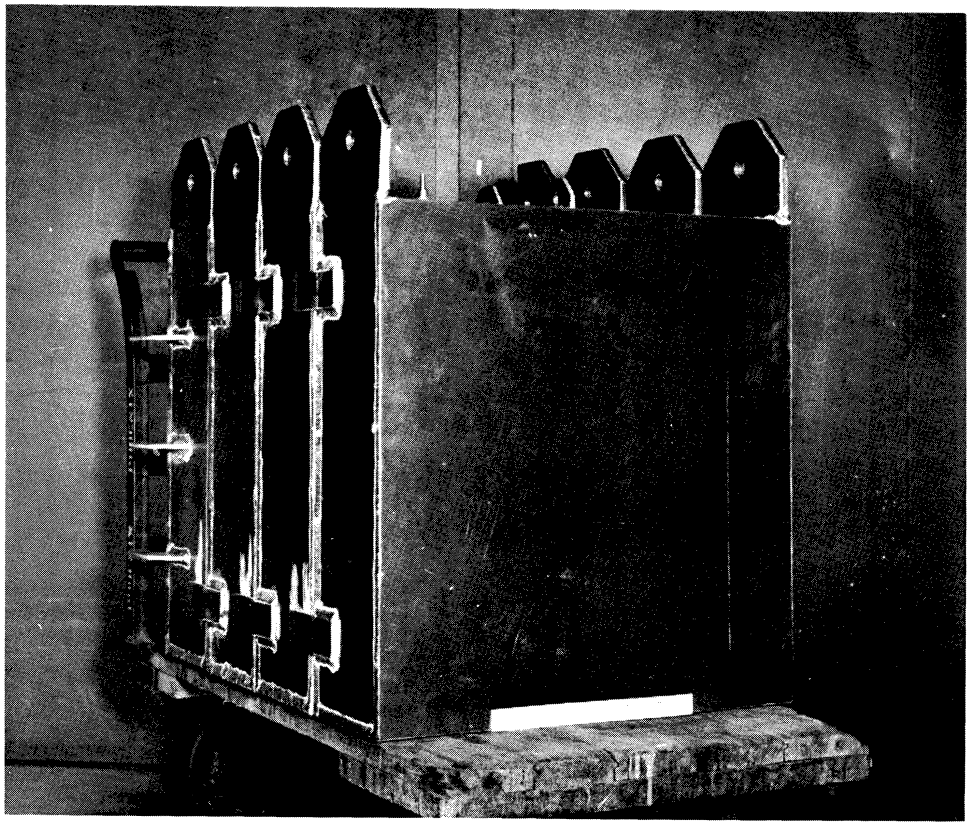

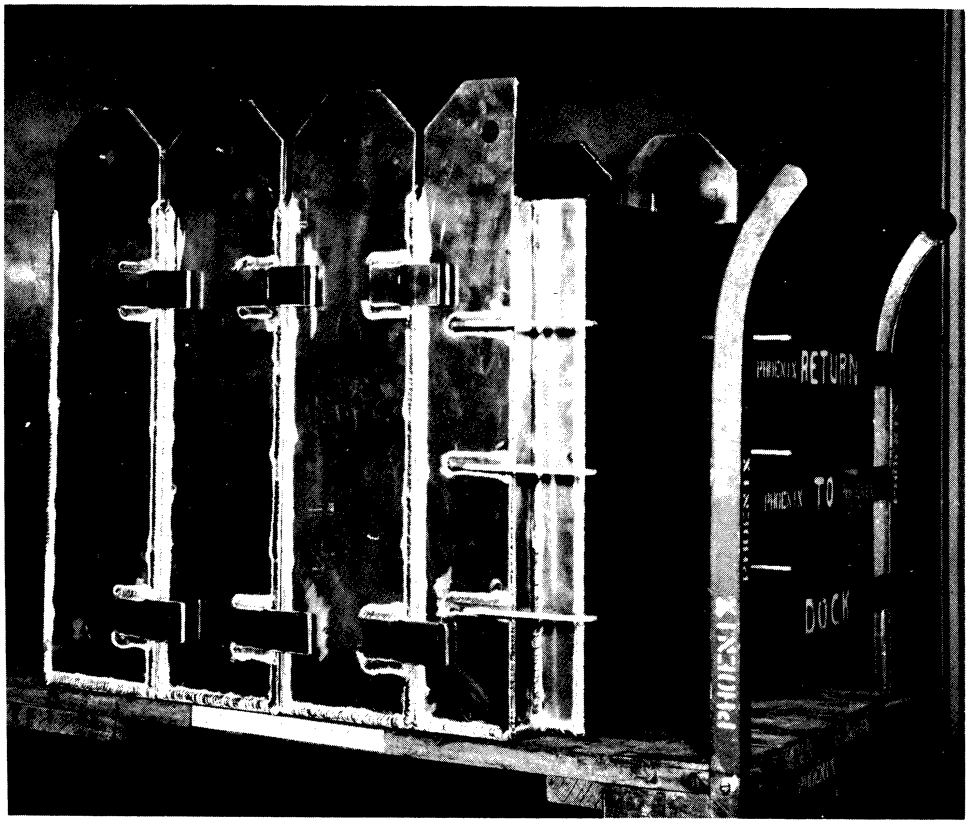

Figure 22. Two views of four graphite slabs.

Figure 23. Three graphite slabs positioned against FNR core.

2. Reactor Core Modification

Unfortunately the reactivity of the graphite slabs positioned directly against the fuel elements on the south core face exceeded the maximum reactivity allowed an experiment by the USAEC license for the FNR. Thus, in order to decouple the slabs and core, a row of graphite reflector elements was added on the south core face. The resulting core configuration is shown in Figure 18. It should be noted that this configuration introduces a 2-cm water gap between the graphite reflector elements and the zero collimator position. Hence, the source spectrum for the graphite measurements differs from that of the water measurements in that the former includes the effect of an additional 10-cm penetration through the row of graphite reflector elements and the water gap. The volume fractions for the graphite reflector elements are: 85.1% graphite (1.65 grams/cm^3),7.9% aluminum, and 7.0% water. In order to keep the source spectrum constant, the water gap was maintained during all graphite measurements.

3. Normalization and Reactor Power

These measurements were normalized to reactor power as in the water measurements except the aluminum wires were located differently during activation. They were positioned on a 36-cm diameter circle within the water gap. No perturbation in the wire activation due to the collimator position was observed.

Except for the measurements of the source spectrum, the reactor was operated at 2 megawatts. The source spectrum was measured at power levels

of 0.5 and 1.0 megawatt using the thick detector and thin detector, respectively.

4. Counting Times and Statistics

The graphite measurements were made during a three-week period. The counting times varied from three 20-minute foreground counts and three 10-minute background counts for the thin detector-thin radiator case with 0 slabs of graphite to five 10-hour foreground counts and five 5-hour background counts for the thick detector-thick radiator case with 3 slabs of graphite. As for the water measurements, the foreground and background counts were alternated.

At the higher neutron energies, the counting statistics were slightly poorer than those of the water data. At 10 Mev, one sigma ranged from 4.1% to 7.7%, and at 12 Mev it varied from 9.5% to 23.3%.

5. Measured Spectra and Experimental Uncertainties

A machine plot of the measured spectra of FNR leakage neutrons which penetrated 0, 1, 2, and 3 slabs of graphite is shown in Figure 24. The structure is the energy averaged effect of the elastic scattering cross section of carbon. Again, the scatter of data points at the higher energies is due to statistical fluctuations. The errors are the same as those of the water measurements except for those associated with counting statistics, aluminum activation, shield thickness and shield density. These are noted in Table 7.

The measured spectra in both water and graphite are tabulated in Appendix C.

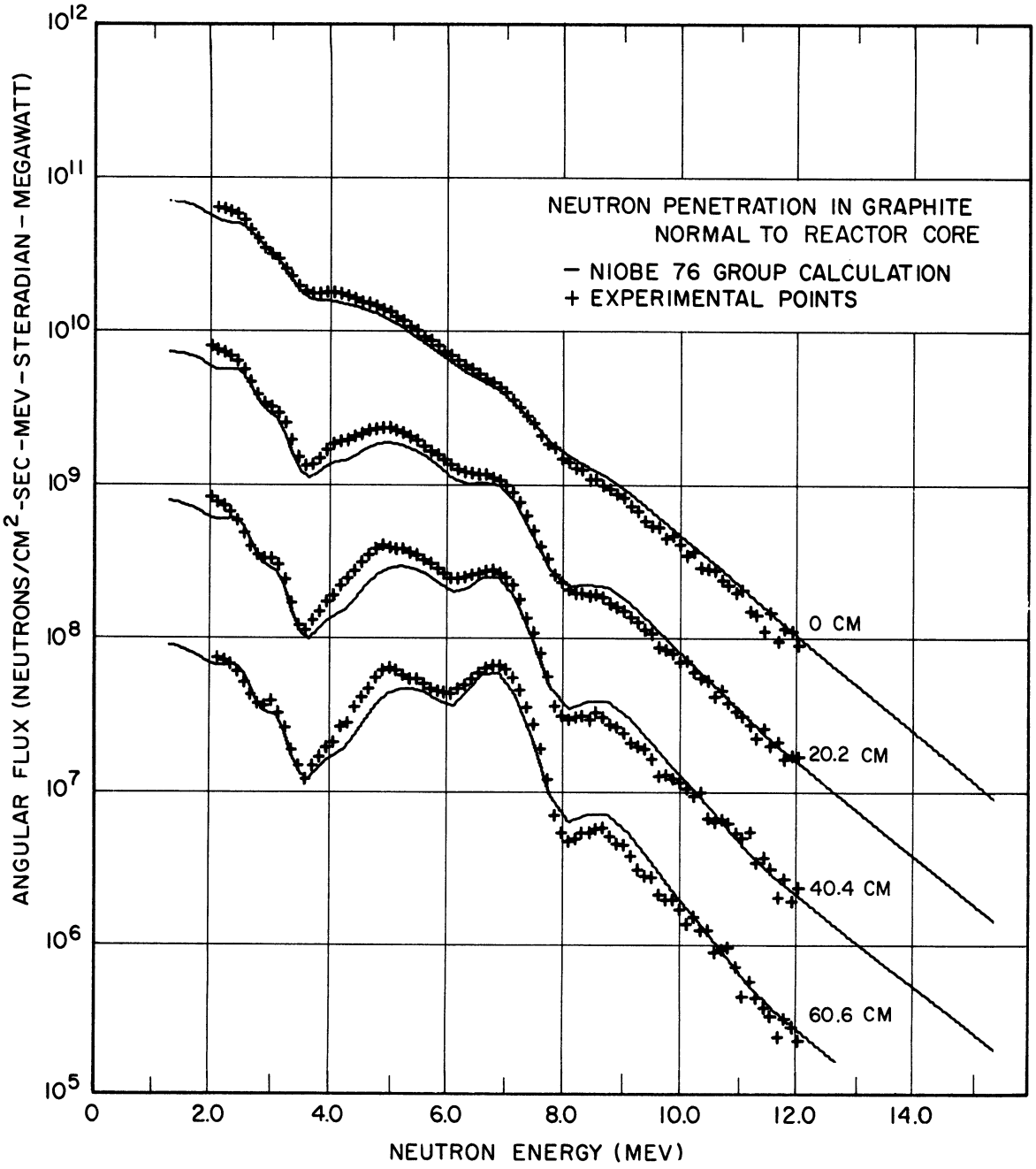

Figure 24. Neutron penetration in graphite.

CHAPTER IV

COMPARISON WITH CALCULATIONS AND CONCLUSIONS

A. NIOBE CALCULATIONS

The calculated spectra shown in Figures 21 and 24 were obtained with the NIOBE (Numerical Integration of Boltzmann Equation) code.* This code was developed by Nuclear Development Corp. (now United Nuclear Corp.) beginning with the work of Certaine and Mittelman[104] in 1955 and culminating in codes for the IBM 704 in 1960[12] and for the IBM 7090 in 1961[13]. NIOBE was selected because of its ability to calculate angular fluxes at deep penetrations through multilayered configurations, its capacity for many energy groups, and its exactness. It has two important restrictions: only spherical configurations are allowed, and any inelastic scattering cross sections used are treated as isotropic in the laboratory system.

1. Neutron Transport Equation

NIOBE solves the following steady state, multienergy, neutron transport equation for a finite, multilayered, spherical configuration.

$$\bar{\Omega} \cdot \bar{\nabla} F(r,\mu,E) + \Sigma_t (r,E) F(r,\mu,E) = S(r,\mu,E) + I_{el}(F;r,\mu,E) + I_{in}(F;r,\mu,E)$$

Where:

$F(r,\mu,E)$ is the angular flux, i.e., the number of neutrons with energy E, per second, per unit energy, per steradian, which move in directions

*All NIOBE calculations were performed by G. G. Sherwood[103] using the IBM-7094 at the Institute for Defense Analysis, Washington, D.C.

making an angle whose cosine is μ with the radius vector crossing unit area normal to the neutron direction, at distance r measured from the origin.

$S(r,\mu,E)$ is the number of neutrons produced by true sources per second, with energy E, which move in directions making an angle whose cosine is μ with the radius vector, per unit volume, per unit energy, per steradian, at distance r.

$I_{el}(F;r,\mu,E)$ is the number of neutrons produced per second, with energy E, which move in directions making an angle whose cosine is μ with the radius vector, per unit volume, per unit energy, per steradian, as a result of elastic scattering by all nuclei present at distance r, when the angular flux is $F(r,\mu,E)$.

$I_{in}(F;r,\mu,E)$ is defined similarly for inelastic scattering.

$$\bar{\Omega} \cdot \bar{\nabla} = \mu \frac{\partial}{\partial r} + \left(\frac{1-\mu^2}{r}\right) \frac{\partial}{\partial \mu} \quad ;$$

$$\Sigma_t(r,E) = \sum_i N_i(r)\sigma_{ti}(E) \quad ;$$

$N_i(r)$ is the number of atoms per unit volume of isotope i at distance r.

$\sigma_{ti}(E)$ is the total cross section per atom of isotope i at energy E.

The required boundary condition is that the flux at the outer boundary of the configuration be specified. (i.e., that $F(A,\mu,E)$ be given for $\mu < 0$ where A is the outer radius).

In order to reduce this equation to terms suitable for numerical integration, it is assumed that the angular dependence of $F(r,\mu,E)$ can be represented by a finite Legendre series expansion. Accordingly,

$$F(r,\mu,E) = \sum_{\ell=0}^{L} \frac{2\ell+1}{4\pi} F_\ell(r,E) P_\ell(\mu) \qquad L \leq 12$$

Since Legendre polynomials satisfy the orthogonality relation

$$\frac{2\ell+1}{2} \int_{-1}^{1} P_\ell(\mu) P_m(\mu) d\mu = \delta_{\ell m} = \begin{cases} 0, & \ell \neq m \\ 1, & \ell = m \end{cases}$$

the scalar flux terms are given by

$$F_\ell(r,E) = 2\pi \int_{-1}^{1} F(r,\mu,E) P_\ell(\mu) d\mu$$

The Gaussian quadrature rule is used to evaluate the above integral. This scheme requires the selection of a discrete set of μ_q which are the zeros of the Legendre polynomial of degree $2Q$, where Q is an integer. This set of μ_q are the rays of the angular mesh. The selection of discrete angular rays so as to facilitate integration is generally referred to as the discrete ordinate method.

2. Source Terms

The source terms represent the total neutron gains per second per unit volume per unit energy per steradian due to true sources such as fission neutrons and slowing down sources consisting of elastically and inelastically scattered neutrons.

The true source in the reactor core region is the fission source.

It was assumed to be separable; i.e. $S(r,\mu,E) = W(\mu)V(r)g(E)$. Also, the angular distribution was assumed to be isotropic in the laboratory system. Thus, $W(\mu) = 1/4\pi$. The radial distribution, V(r), was approximated by the measured radial thermal flux distribution[36] for the ORNL BSR-I. Subsequent NIOBE calculations were made to test the sensitivity of the spectra to this V(r). A flat radial distribution produced no significant change in the core leakage spectrum. Hence, it was concluded the form of V(r) used was satisfactory.

The source energy distribution was represented by a normalized Maxwellian distribution, $g(E) = (2/\sqrt{\pi T^3})E^{1/2}e^{-E/T}$. The Maxwellian spectrum was chosen because it agrees with measured U^{235} fission spectra as well or better than Watt[105] or Cranberg[106] spectra[107-110], its analytical form is simple, and it requires only one parameter, T. NIOBE calculations were carried out for several values of T to obtain a best fit to the FNR leakage spectrum (0 cm water). The calculated spectra were sufficiently sensitive to the choice of T that it could apparently be inferred to within $\pm$0.010 Mev. The best fit was for T=1.285 Mev. This compares well with T=1.30$\pm$0.03 Mev given by Terrell[108] and the average T=1.30 Mev for the eight measurements reviewed by Condé and During[111]. All of these T values refer to U^{235} fission induced by thermal neutrons.

For the region outside the core, both the internal source distribution and the incoming flux at the outer radius were specified to be zero.

The elastic scattering source term, $I_{el}(F;r,\mu,E)$, is evaluated by representing the angular dependence of the elastic scattering cross sec-

tion in the center-of-mass system by a finite Legendre series expansion. Then the scattering integral is evaluated using a scattering model appropriate to the mass of the scattering nuclei. NIOBE includes models for hydrogeneous, infinitely heavy, and intermediate weight scatterers. The scattering model for hydrogen treats the scattering as isotropic in the center-of-mass system.

The inelastic scattering source term, $I_{in}(F;r,\mu,E)$, is evaluated by treating the scattering as isotropic in the laboratory system. When inelastic scattering data is available, the energy distribution of the neutrons emitted per inelastic scattering at energy E, G(E,E'), is tabulated as a function of E and E'.

In summary, the energy dependent cross section data required for each element consists of (1) the total cross section, (2) the elastic scattering cross section and Legendre coefficients, and (3) the inelastic scattering cross section and the energy distribution of inelastically scattered neutrons.

3. Energy Groups

In addition to the use of an angular mesh and a radial mesh, an energy mesh, which divides the energy region of interest into equal intervals of ln E, is used. The introduction of the energy mesh allows the transport equation to be reduced to a set of coupled equations in which the slowing down and transport terms can be treated separately. These equations are solved in two steps. First, using assumed solutions, the slow-

ing down source is calculated for each energy group. The true source is then added to the slowing down source to get the total source for each energy group. The second step is to solve the resulting set of "one velocity" transport equations which have these source terms. The solutions are then compared with the initially assumed solutions and the process is repeated until two successive iterations agree within a specified tolerance.*

Examination of the cross sections of interest showed that 4% energy intervals retained most of the differential energy detail. More importantly, 4% energy widths clearly retain more structure than is visible within the limits of the spectrometer resolution ($\geq$ 12%). Use of 4% energy intervals required 76 energy groups for the energy range from 0.90 to 18.02 Mev. Sherwood's 76 group P_7 NIOBE calculations (16 angular rays and 105 radial points) required about 1 hour on the IBM-7094 computer.

4. Geometry

For the water calculations, the FNR core was represented as a sphere of approximately equal volume (29 cm radius, 58% H_2O and 42% aluminum) and the pool water was represented as a spherical shell (80 cm thick, 100% H_2O) about this central region.

The same central region was used for the graphite calculations. Here it was surrounded by two regions: (1) a 10 cm thick shell representing the row of graphite reflector elements and the water gap (volume

*The convergence criterion used was 0.001.

fractions: 68.9% graphite (1.65 grams/cm^3), 24.7% water, and 6.4% aluminum) and (2) an 80 cm thick graphite shell (volume fractions: 93.7% graphite (1.74 grams/cm^3) and 6.3% aluminum).

5. Cross Sections

Cross section data was required for hydrogen, carbon, oxygen, and aluminum. For hydrogen, the total and elastic scattering cross sections are the same. The scattering model for hydrogen which treats elastic scattering as isotropic in the center-of-mass system and the theoretical total cross section curve reported in BNL-325[112] were used. KAPL total and elastic scattering cross sections and Legendre coefficients were used for carbon[113] and oxygen.[114] Since this data extended only up to 15 Mev, the values at 15 Mev were assumed constant to 18 Mev. Due to the unavailability of inelastic scattering data for carbon and oxygen, it was omitted in the slowing down source terms. For aluminum, GA[115] cross section data, including inelastic, was used.

6. Comparison With Measurements

Because the use of 76 energy groups permitted the calculations to show considerably more energy detail than the measurements, comparisons between NIOBE calculations and measured spectra were difficult to evaluate. In order to simplify the comparison, the energy dependent spectrometer response function was convoluted with the NIOBE calculations. The response function was assumed to be a Gaussian distribution function with its FWHM

given as a function of neutron energy by the curves shown in Figure 17.* The resulting spectra were normalized with the measured spectra at a single point (7.5 Mev at 0 cm) and machine plotted with them as shown in Figures 21 and 24. A quantitative comparison is given in Table 8 which shows the average and maximum ratios of the calculated flux to the measured flux.

TABLE 8

RATIOS OF CALCULATED FLUX TO MEASURED FLUX

Shield Thickness	Average Ratio	Maximum Ratio
0 cm H_2O	1.00	0.90 at 4.3 Mev
20.0 cm H_2O	0.92	0.86 at 3.3 Mev
40.0 cm H_2O	0.93	0.80 at 2.3 Mev
60.0 cm H_2O	0.99	1.30 at 8.5 Mev
0 cm Graphite	1.00	0.82 at 2.2 Mev
20.2 cm Graphite	0.95	0.74 at 4.2 Mev
40.4 cm Graphite	0.96	0.67 at 4.5 Mev
60.6 cm Graphite	0.98	0.67 at 4.9 Mev

The comparison shows surprisingly good agreement, particularly with the water data, in view of the assumptions made in the NIOBE calculations.

*A smooth line between the thin radiator curve at 4 Mev and the thick radiator curve at 6 Mev was used for the 4 to 6 Mev region.

These include (1) all regions are homogeneous and spherically symmetrical, (2) there is no inelastic scattering by carbon and oxygen in the slowing down source terms, (3) hydrogen scattering is isotropic in the center-of-mass system, (4) inelastic scattering by aluminum is isotropic in the laboratory system, and (5) carbon and oxygen cross sections and Legendre coefficients are constant from 15 Mev to 18 Mev. With regard to the graphite calculations, much better agreement was obtained by the questionable procedure of mixing cross sections and Legendre coefficients from different libraries.

In convoluting the spectrometer response function with the NIOBE calculations, an important bias is introduced. As demonstrated analytically in Chapter II, the convolution process introduces a tilt in exponential spectra. Thus, the inference of the Maxwellian T characteristic of the U^{235} fission spectrum from the comparison of the measured core leakage spectrum with smoothed spectra calculated for different values of T requires the response function to be sufficiently well known so as to introduce little or negligible uncertainty in finding T. The greatest uncertainty in the response function is that associated with the radial distribution function, $F(r_m)$. From Table 6, this uncertainty is estimated to be $\pm 10\%$. Equation 14 shows that a $\pm 10\%$ uncertainty in $\Delta E/E$ introduces $\leq \pm 0.5\%$ uncertainty in the slope of smoothed spectra. Since the uncertainty in T associated with matching the measured and calculated core

leakage spectra is ±0.010 Mev, the total* uncertainty in T is ≤ ± [0.010 Mev + 0.005 (1.285 Mev)] or ≤ ±0.016 Mev. Most measurements[108,111] of this T have reported uncertainties of ±0.030 or ±0.040 Mev.

B. CONCLUSIONS

A relatively simple, moderate resolution (12%), low efficiency (10^{-6}), differential proton-recoil, fast neutron spectrometer has been developed to measure directed neutron fluxes in the presence of high intensity fission gamma fields (10^7 to 10^8 roentgens/hour). It has been used to measure the energy distributions (2 to 12 Mev) of normally directed neutrons which leaked from the Ford Nuclear Reactor core and penetrated several thicknesses of two common reactor materials, H_2O and graphite.

In contrast to Clifford *et al.*'s[49] recent spectrum measurements of uncollided reactor neutrons, these measured spectra are dominated by scattered neutrons. For example, the ratio of scattered neutrons to unscattered neutrons ranges from 100 at 2 Mev to 1 at 12 Mev for neutrons which penetrated 60 cm of H_2O. Although measurements of uncollided neutrons test the total cross sections very well, these measurements test both the total cross sections and the slowing down sources. In contrast with other measurements dominated by scattered neutrons and compared with detailed calculations (such as Verbinski's[36] spectra in H_2O and Profio's[33] spectra in CH_2), the agreement between these measured and

*This does not include effects of uncertainties in the energy calibration of the spectrometer or in the cross sections used in the NIOBE calculation of the core leakage spectrum.

calculated spectra is excellent.

In summary, because of the relatively high accuracy ($\pm$10% relative intensity and $\pm$20% absolute intensity, $\pm$2% energy) and the deep penetration (up to 60 cm), these measurements are the most useful that have been reported for testing detailed calculations of fast neutron spectra in bulk media.

C. SUGGESTED FUTURE WORK

Opportunities for extending the present work lie in two directions. One is in the choice of experiments and the other is in the modification and improvement of the spectrometer. However, except for modifications which give a general reduction in background (as for example might result from reducing the ID of the beam trap or reshaping the collimator throat), the important changes in the spectrometer system will probably reflect the choice of experiment. The following experiments are fairly direct extensions of the present work.

1. Spectrum measurements in H_2O at oblique angles.
2. Spectrum measurements at higher energies.[103]
3. Spectrum measurements in other bulk materials (e.g. materials with relatively high and well known inelastic scattering cross sections such as iron).
4. Spectrum measurements of fission sources and (α,n) sources.
5. Measurement of angular distributions of n-p scattering using multiple detectors or a single movable detector in the detector chamber.

6. Measurements of spectrometer efficiency and resolution using $D(d,n)He^3$ and $T(d,n)He^4$ neutron sources of known intensity and energy width.

7. Collimator studies[116-122] to measure the influence of (a) wall and liner material, (b) shape, and (c) length.

APPENDIX A

EFFECT OF CARBON RECOILS

Fast neutrons incident on CH_2 radiators scatter carbon ions as well as protons. Although many of the carbon ions are stopped within the radiator, those which do escape the radiator and reach the detector are indistinguishable from protons of the same energy. The necessary condition for the background counts due to carbon recoils to be negligible compared to the proton recoil counts is that

$$\left.\frac{C(E_c)}{C(E_p)}\right|_{E_c=E_p} << 1 \quad \text{for} \quad (E_{min}\overline{\cos^2\psi} - \delta E_p) \leq E_p \leq (E_{max}\overline{\cos^2\psi} - \delta E_p)$$
$$\text{or} \quad 1.5 \text{ Mev} \leq E_p \leq 10.0 \text{ Mev}$$

where $C(E_p)$ is the count rate for protons with energy E_p, and

$C(E_C)$ is the count rate for carbon ions with energy E_C.

To find the ratio of carbon recoil counts to proton recoil counts, first note that from Equations 2 and 6,

$$C(E_p) = \epsilon(E)\phi(E)\frac{dE}{dE_p} = \frac{1}{\pi} N_R^H t_R G \overline{\cos\psi}\, \sigma_{n-p}(E)\phi(E)\frac{dE}{dE_p} \qquad (15)$$

where $$G \equiv \left(\frac{A_C A_R A_D}{L_C^R L_D^R}\right)$$

The expression for the total efficiency, $\epsilon(E)$, was derived with the assumptions that n-p scattering is isotropic in the center-of-mass system and that all protons which are scattered toward the detector escape the radiator with some mean energy loss δE_p, where $\delta E_p \ll E_p$. Both of these assumptions are invalid for carbon ions because n-C scattering is not

isotropic in the center-of-mass system and the carbon ion energy losses in the radiator are so large that most of the ions do not escape the radiator with energies above 1.5 Mev.

The energy of the carbon ions before losing any energy is related to the energy of the incident neutrons by

$$E'_c = \frac{4A}{(A+1)^2} E' \overline{\cos^2\psi} \tag{16}$$

With A = 12 and $\overline{\cos^2\psi} = 0.83$, $E'_C = 0.236E'$

An expression for $C(E_C)$ which includes the carbon ion energy losses in the radiator is developed as follows

$$C(E_c)dE_c = \int_{E_c}^{E''_c} C_o(E'_c)dE'_c\, P(E'_c, E_c)dE_c \tag{17}$$

where $C_o(E'_C)dE'_C$ is defined as $C(E_C)dE_C$ except that carbon ion energy losses in the radiator are assumed to be zero.

$P(E'_C,E_C)dE_C$ is the probability that carbon ions, which would be counted with energies in dE'_C about E'_C if energy losses in the radiator were zero, are counted with energies in dE_C about E_C.

$E''_C = 0.236E_{max}$

From its definition,

$$C_o(E'_c)dE'_c = \epsilon(E')\phi(E')dE'$$

where $\epsilon(E')$ is the total efficiency for counting carbon ions with energy $E'_C = 0.236E'$. It is evaluated as before for n-p scattering except that the carbon ions are assumed to be scattered isotropically in the laboratory system. This assumption requires that

$$\frac{d\sigma_{n-C}(E',\psi)}{d\Omega} = \frac{\sigma_{n-C}(E')}{4\pi}$$

This is equivalent to replacing $(1/\pi)\ \sigma_{n-p}(E)\ \overline{\cos\psi}$ by $(1/4\pi)\ \sigma_{n-C}(E)$ in the previous expression for $\epsilon(E)$ so that

$$C_0(E'_c)dE'_c = \frac{1}{4\pi} N_R^c t_R G\, \sigma_{n-C}(E')\, \phi(E')dE' \qquad (18)$$

Thus,

$$C(E_c) = \frac{1}{4\pi} N_R^c t_R G \frac{dE'}{dE'_c} \int_{E_c}^{E''_c} P(E'_c, E_c)\, \sigma_{n-C}(4.24E'_c)\, \phi(4.24E'_c)dE'_c$$

Hence, the ratio of count rates is

$$\frac{C(E_c)}{C(E_p)} = \left(\frac{1}{4\overline{\cos\psi}}\right)\left(\frac{N_R^c}{N_R^H}\right)\frac{\left(\frac{dE'}{dE'_c}\right)}{\left(\frac{dE}{dE_p}\right)} \frac{\int_{E_c}^{E''_c} P(E'_c, E_c)\, \sigma_{n-C}(4.24E'_c)\, \phi(4.24E'_c)\, dE'_c}{\sigma_{n-p}(E)\, \phi(E)} \qquad (19)$$

For a CH_2 radiator, $(N_R^C/N_R^H) = 1/2$.

Here $\overline{\cos\psi} = 0.91$, $(dE/dE_p) \cong (1/\overline{\cos^2\psi}) = 1.20$, and $(dE'/dE'_C) = 4.24$.

Using these values, the ratio becomes

$$\frac{C(E_c)}{C(E_p)} = 0.464 \frac{\int_{E_c}^{E''_c} P(E'_c, E_c)\, \sigma_{n-C}(4.24E'_c)\, \phi(4.24E'_c)dE'_c}{\sigma_{n-p}(E)\, \phi(E)}$$

In order to evaluate the integral, $\sigma_{n-C}(E)$ and $\varphi(E)$ must be specified.

For example, choose

$$\phi(E) = \begin{cases} \phi(E) & \text{for } 0 < E < 4.24(E_c)_{min} \\ \phi_0 & \text{for } 4.24(E_c)_{min} \leq E \leq E_{max} \\ 0 & \text{for } E > E_{max} \end{cases}$$

where $(E_C)_{min} = (E_p)_{min} = (E_{min}\ \overline{\cos^2\psi} - \delta E_p) = 1.5$ Mev and $4.24\ (E_C)_{min} = 6.36$ Mev

Since $\sigma_{n-C}(E) = 1.5 \pm 0.8$ barns for 6.36 Mev < E < 20 Mev, choose

$$\sigma_{n-C}(E) = \overline{\sigma_{n-C}} = 1.5 \text{ barns} \quad \text{for } 6.36 \text{ Mev} \leq E \leq 20 \text{ Mev}$$

For this example,

$$\frac{C(E_c)}{C(E_p)} = 0.484\ \frac{\overline{\sigma_{n\text{-}c}}}{\sigma_{n\text{-}p}(E)} \int_{E_c}^{E_c''} P(E_c', E_c)\, dE_c'$$

To evaluate the integral, assume

$$P(E_c', E_c)\, dE_c' = P(x)\, dx = \frac{dx}{t}$$

where $x = R^c_{CH_2}(E_c') - R^c_{CH_2}(E_c)$ for $0 \le x \le \left[R^c_{CH_2}(E_c'') - R^c_{CH_2}(E_c)\right]$

and $t \ge R^c_{CH_2}(E_c'')$

$R^C_{CH_2}(E_C)$ is the range of carbon ions with energy E_C in CH_2

$$t = t_R \overline{\sec\psi} = 1.38 \text{ milligrams/cm}^2$$

Thus,

$$\int_{E_c}^{E_c''} P(E_c', E_c)\, dE_c' = \int_0^{R^c_{CH_2}(E_c'') - R^c_{CH_2}(E_c)} \frac{dx}{t} = \frac{R^c_{CH_2}(E_c'') - R^c_{CH_2}(E_c)}{t_R\ \overline{\sec\psi}}$$

Using this result,

$$\left.\frac{C(E_c)}{C(E_p)}\right|_{E_c = E_p} = 0.525\ \frac{R^c_{CH_2}(E_c'') - R^c_{CH_2}(E_c)}{\sigma_{n\text{-}p}(E)} \quad \frac{\text{barns}}{\text{mg/cm}^2} \qquad (20)$$

where $E_C = E_p = E\ \overline{\cos^2\psi} - \delta E_p$ and $E_C'' = 0.236\ E_{max}$.

A range-energy curve for carbon ions in CH_2 is not available. An approximate one can be obtained using the following relationship[123].

$$\frac{R^c_{CH_2}(E_c/M_c)}{R^c_c(E_c/M_c)} = \frac{R^H_{CH_2}(E_H/M_H)}{R^H_c(E_H/M_H)} \qquad \text{for } \left(\frac{E_c}{M_c}\right) = \left(\frac{E_H}{M_H}\right)$$

With M_H = 1 amu and M_C = 12 amu,

$$R^c_{CH_2}(E_c/12) = \frac{R^H_{CH_2}(E_H)}{R^H_c(E_H)}\ R^c_c(E_c/12) \qquad \text{for } (E_c/12) = E_H$$

where E_H and $(E_C/12)$ are the energies of the hydrogen and carbon ions, respectively, expressed in Mev/amu.

A range-energy curve for protons in carbon for the proton energies of interest (0.1 to 0.5 Mev) is not available. Hence, the ratio of ranges of protons in CH_2 and carbon is estimated by assuming that both of the ranges can be represented by $R(E) = AE^B$ so that

$$\frac{R^H_{CH_2}(E_H)}{R^H_C(E_H)} = \frac{A^H_{CH_2}}{A^H_C}(E_H)^{B^H_{CH_2} - B^H_C}$$

The constants are evaluated using the ranges of protons in CH_2 and carbon at $E_H = 2$ Mev and $E_H = 4$ Mev as calculated by Barkas and Berger[81]. Using this procedure, the ratio is found to vary from 0.70 to 0.75 as E_H increases from 0.1 to 0.5 Mev.

Using these results and a range-energy curve[123] for carbon ions in carbon, an approximate range-energy curve for carbon ions in CH_2 is obtained. From this curve, which is shown in Figure 25, and the values for $\sigma_{n-p}(E)$ which are tabulated by Gammel[100], the ratio of count rates is calculated for $E_{max} = 14$ Mev and $E_{max} = 18$ Mev. The results are shown in Figure 26 as a function of the incident neutron energy.

It is noted that this example generally overestimates the background due to carbon recoils for the spectrum measurements reported here. Even so, as shown in Figure 26, the effect of carbon recoils is small.

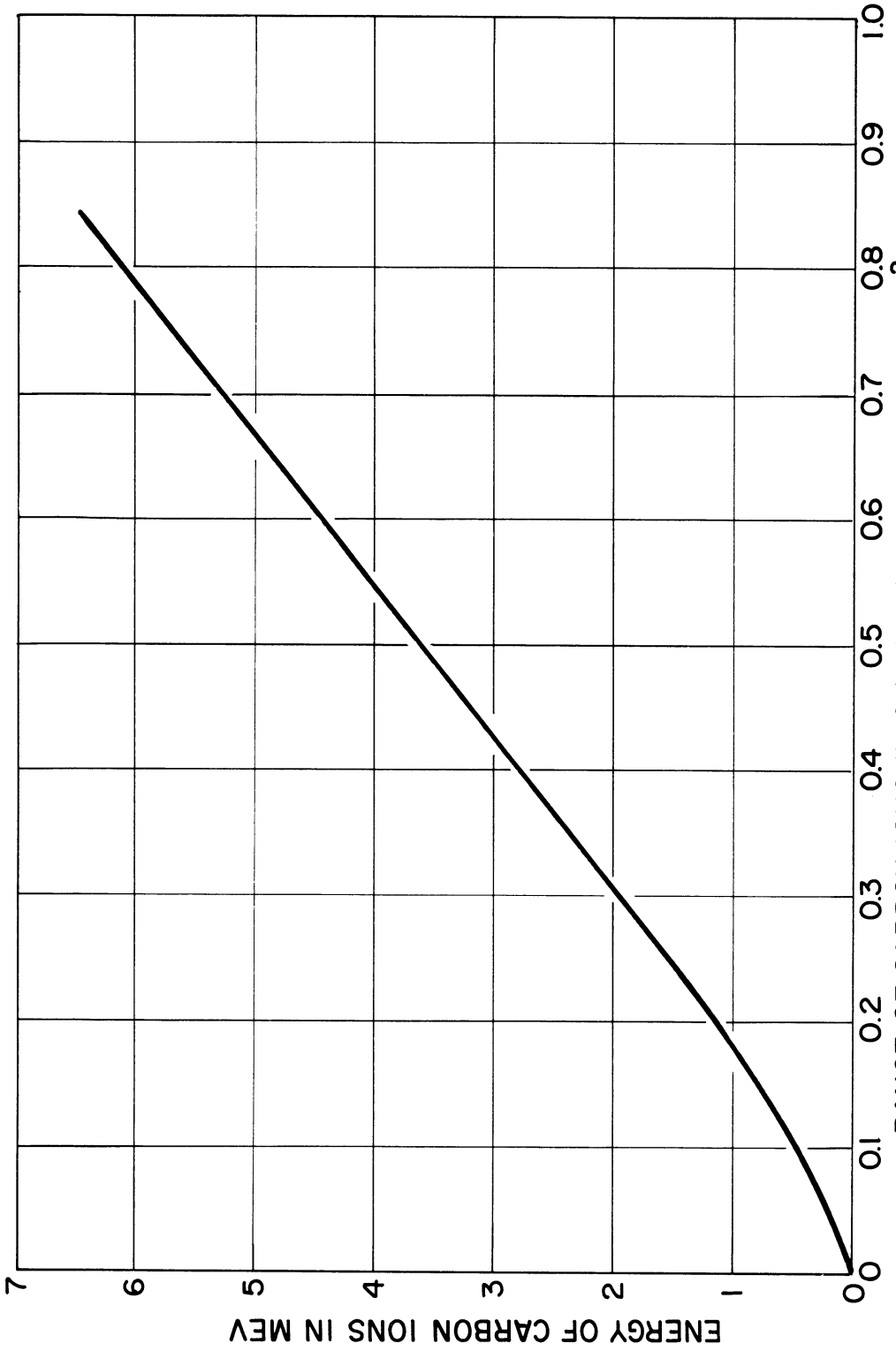

Figure 25. Range of carbon ions in polyethylene.

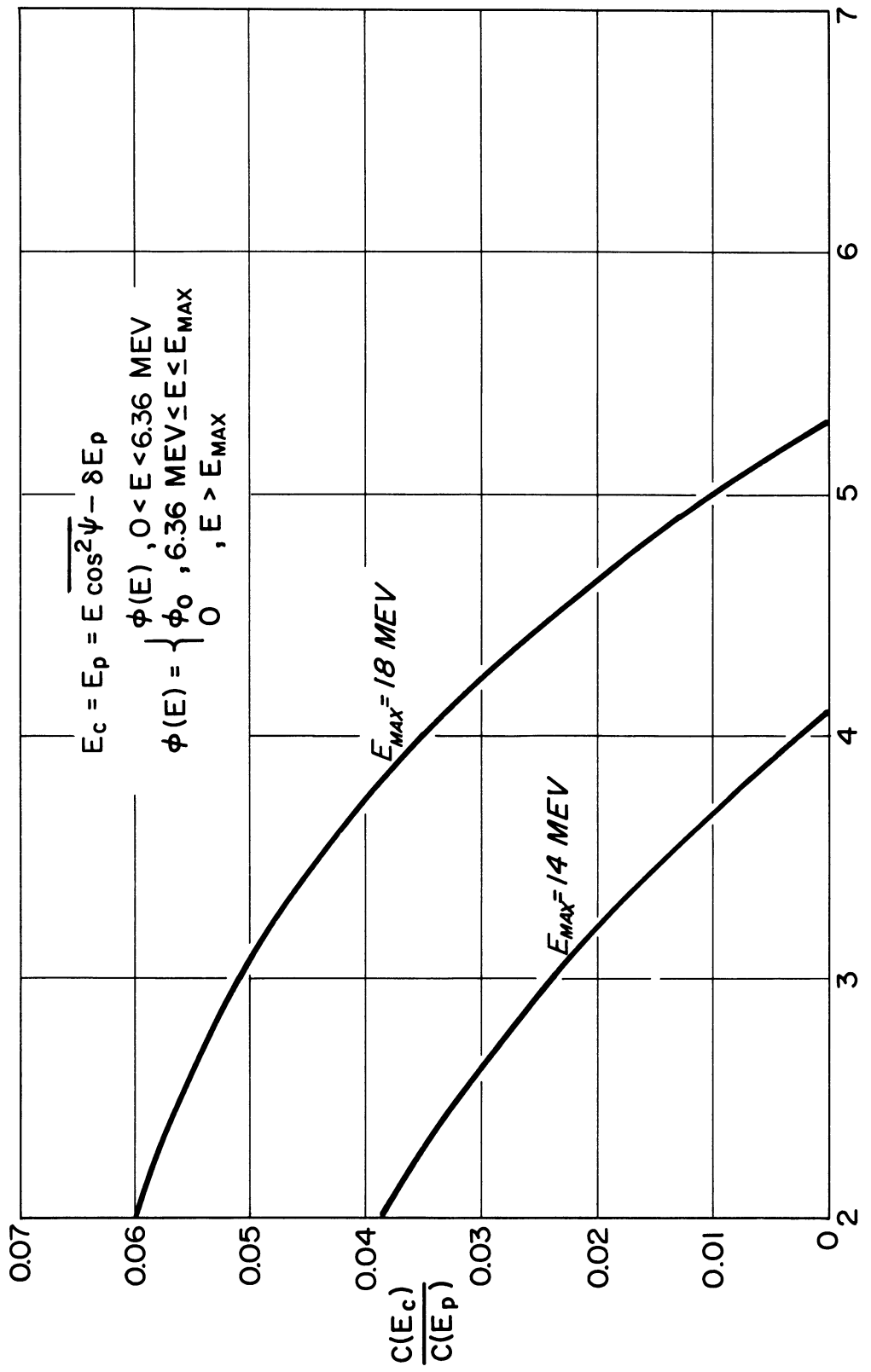

Figure 26. Ratio of carbon recoil counts to proton recoil counts.

APPENDIX B

COLLIMATOR EFFECTS

To zeroth order approximation, the neutron beam which exits the collimator consists only of neutrons which entered the source end of the collimator and traveled to the exit end without being scattered or attenuated. Let these neutrons be designated F_E. Three corrections must be considered. First, a fraction of the neutrons are absorbed or scattered by the gas in the collimator. For long, air-filled collimators this fraction can be significant. Here, it is negligible because the collimator is evacuated.

Secondly, some of the neutrons in the exiting beam entered the collimator through the source end, but were scattered in the collimator wall before reaching the exit. These neutrons are degraded in energy, although for long collimators the most probable scattering angles may be so small that the energy degradation is negligible. Even so, these scattered neutrons were not directed toward the exit when they entered the collimator so that the exiting neutrons have an additional component which is designated F_{EW}.

Thirdly, some of the neutrons in the exiting beam entered the collimator initially through the wall rather than through the source end. Let this additional component be designated F_W.

Both F_{EW} and F_W depend on the angular dependence of the source and on the geometry of the source and the collimator. There are no general

expressions available which can be used to evaluate these terms. However, they can be roughly estimated for long, cylindrical and long, conical collimators used with isotropic sources. Here "long" implies that the length of the collimator is much larger than its largest diameter.

Simon and Clifford[116] have estimated (F_{EW}/F_E) for the case where a point, isotropic source is located on the axis of a long, cylindrical collimator. Their calculation considers only single scattering in the collimator walls and depends on the assumptions that the scattering is isotropic in the laboratory system and that the energy degradation is negligible. Their result is

$$\left(\frac{F_{EW}}{F_E}\right) \cong \frac{\pi}{2}\left(\frac{\Sigma_s}{\Sigma_t}\right)\left(\frac{\delta}{\ell}\right) \tag{21}$$

where δ is the radius of the cylinder

ℓ is the length of the cylinder

Σ_s and Σ_t are the macroscopic scattering and total cross sections, respectively, for the wall of the cylinder.

If the collimator wall is hydrogeneous, it is a good approximation to assume the scattering is isotropic in the center-of-mass system. This assumption can be incorporated into the above results by replacing Σ_s by $4\,\Sigma_s\,\bar{\mu}$, where $\bar{\mu}$ is the average cosine of the scattering angles associated with F_{EW}. Since for long collimators, most of the neutrons which contribute to F_{EW} are scattered through relatively small angles, $\bar{\mu}$ is approximately unity. Thus, for long, cylindrical collimators with hydrogeneous walls,

$$\left(\frac{F_{EW}}{F_E}\right) \cong 2\pi\left(\frac{\Sigma_s}{\Sigma_t}\right)\left(\frac{\delta}{\ell}\right) = 2\pi\left(\frac{\lambda_t}{\lambda_s}\right)\left(\frac{\delta}{\ell}\right) \qquad (22)$$

where: $\lambda_s = 1/\Sigma_s$ and $\lambda_t = 1/\Sigma_t$

Extension of the analysis of Simon and Clifford to long, conical collimators gives the same result except that

$$\delta = \frac{1}{2}(\delta_s + \delta_e)$$

where: δ_s is the radius of the source end and

δ_e is the radius of the exit end

(F_W/F_E) can be crudely estimated for the case of a plane, isotropic source at the end of a long, cylindrical collimator. If only the uncollided neutrons are considered, it can be shown that

$$\left(\frac{F_W}{F_E}\right) \cong 2\left(\frac{\lambda_t}{\ell}\right) \qquad (23)$$

Extension of the same analysis to long, conical collimators gives

$$\left(\frac{F_W}{F_E}\right) \cong 2\left(\frac{\delta_e}{\delta_s}\right)\left(\frac{\lambda_t}{\ell}\right) \qquad (24)$$

From the above two expressions, it is noted that

(1) For long collimators, (F_W/F_E) depends on (λ_t/ℓ), not (δ/ℓ);

(2) When using a long, conical collimator with a plane source, it is advantageous to use the large end of the collimator as the source end so that $(\delta_e/\delta_s) < 1$.

Also, it is noted that the above expressions for (F_W/F_E) do not include neutrons which enter the collimator through the wall and then

reenter the wall to be scattered to the collimator exit. This contribution is expected to be small compared to (F_{EW}/F_E), at least when $(\delta_e/\delta_s) < 1$.

(F_{EW}/F_E) and (F_W/F_E) can now be evaluated for the collimator used with this spectrometer. The cross section of the collimator is actually dodecagonal rather than circular, but the difference is neglected here. The wall of the collimator is 0.32 cm thick aluminum surrounded by water. Since the aluminum is very thin relative to the mean free path of Mev neutrons in aluminum, the collimator wall is represented by a water wall. Hence, these ratios are evaluated for a long, evacuated, conical collimator with water walls and the following dimensions: ℓ = 305 cm, δ_s = 5.10 cm, and δ_e = 0.95 cm. For 10 Mev neutrons in water, λ_t = 9.6 cm and λ_s = 12.4 cm. Using these values,

$$\left(\frac{F_{EW}}{F_E}\right) \cong \pi \left(\frac{\lambda_t^{H_2O}}{\lambda_s^{H_2O}}\right)\left(\frac{\delta_s+\delta_e}{\ell}\right) = 0.048 \qquad (25)$$

$$\left(\frac{F_W}{F_E}\right) \cong 2\left(\frac{\delta_e}{\delta_s}\right)\left(\frac{\lambda_t^{H_2O}}{\ell}\right) = 0.017 \qquad (26)$$

Thus, $(F_{EW}/F_E) + (F_W/F_E) \cong 6.5\%$. This small percentage, although only a rough estimate, indicates the collimator effects are relatively small.

APPENDIX C

TABULATION OF MEASURED SPECTRA

The measured spectra are tabulated on the following four pages.

The neutron energy .12030E+02 is read 12.03 Mev.

The flux .19700E+09 is read 1.97×10^{8} neutrons sec^{-1} cm^{-2} Mev^{-1} $steradian^{-1}$ $megawatt^{-1}$. It was measured normal to the reactor core.

The phrase 0 CM WATER refers to the thickness (0 cm) of material (water) between the Ford Nuclear Reactor core and the source end of the spectrometer collimator.

NEUTRON ENERGY IN MEV	FLUX 0 CM WATER	FLUX 20.0 CM WATER	FLUX 40.0 CM WATER	FLUX 60.0 CM WATER
.12030E+02	.19700E+09	.38700E+08	.56200E+07	.81100E+06
.11910E+02	.20800E+09	.42400E+08	.70200E+07	.89500E+06
.11790E+02	.23500E+09	.44300E+08	.68700E+07	.95200E+06
.11670E+02	.25200E+09	.51100E+08	.72700E+07	.92800E+06
.11550E+02	.32400E+09	.51800E+08	.87500E+07	.11800E+07
.11430E+02	.30000E+09	.55000E+08	.88900E+07	.12800E+07
.11310E+02	.34500E+09	.65200E+08	.89500E+07	.10300E+07
.11190E+02	.38300E+09	.68400E+08	.99600E+07	.13400E+07
.11070E+02	.40700E+09	.83000E+08	.95400E+07	.14400E+07
.10950E+02	.39300E+09	.78400E+08	.11400E+08	.15000E+07
.10830E+02	.48800E+09	.86700E+08	.12700E+08	.20300E+07
.10710E+02	.48300E+09	.90500E+08	.13400E+08	.21000E+07
.10590E+02	.50900E+09	.99200E+08	.14100E+08	.21400E+07
.10470E+02	.55000E+09	.11800E+09	.16100E+08	.21200E+07
.10350E+02	.65900E+09	.11900E+09	.18200E+08	.22400E+07
.10230E+02	.74200E+09	.12400E+09	.16400E+08	.28000E+07
.10110E+02	.77900E+09	.13400E+09	.21600E+08	.26800E+07
.99900E+01	.86200E+09	.14600E+09	.22600E+08	.30300E+07
.98800E+01	.92500E+09	.16100E+09	.21200E+08	.29400E+07
.97600E+01	.98300E+09	.17600E+09	.25500E+08	.32600E+07
.96400E+01	.10200E+10	.18600E+09	.25100E+08	.32400E+07
.95200E+01	.11800E+10	.20500E+09	.26900E+08	.37900E+07
.94000E+01	.13300E+10	.22600E+09	.32200E+08	.36000E+07
.92800E+01	.13600E+10	.22700E+09	.32000E+08	.46800E+07
.91600E+01	.14600E+10	.24800E+09	.33400E+08	.44500E+07
.90400E+01	.16100E+10	.27700E+09	.35900E+08	.49700E+07
.89200E+01	.17100E+10	.29800E+09	.38000E+08	.49800E+07
.88000E+01	.19100E+10	.30600E+09	.41700E+08	.48700E+07
.86800E+01	.19200E+10	.32700E+09	.39000E+08	.52100E+07
.85600E+01	.22200E+10	.35000E+09	.45100E+08	.53600E+07
.84500E+01	.24400E+10	.39100E+09	.44500E+08	.48400E+07
.83300E+01	.25800E+10	.39400E+09	.47200E+08	.55500E+07
.82100E+01	.28600E+10	.42900E+09	.52000E+08	.63800E+07
.80900E+01	.30900E+10	.45800E+09	.56400E+08	.62000E+07
.79700E+01	.34300E+10	.49600E+09	.61900E+08	.60400E+07
.78500E+01	.36400E+10	.52700E+09	.64400E+08	.63000E+07
.77300E+01	.38800E+10	.56100E+09	.67700E+08	.65800E+07
.76200E+01	.42100E+10	.62700E+09	.71900E+08	.75500E+07
.75000E+01	.47800E+10	.67400E+09	.74900E+08	.74300E+07
.73800E+01	.50700E+10	.71700E+09	.83100E+08	.83300E+07
.72600E+01	.54500E+10	.77900E+09	.88200E+08	.90700E+07
.71400E+01	.58700E+10	.85600E+09	.96800E+08	.10200E+08
.70200E+01	.66400E+10	.91400E+09	.10500E+09	.10600E+08

NEUTRON ENERGY IN MEV	FLUX 0 CM WATER	FLUX 20.0 CM WATER	FLUX 40.0 CM WATER	FLUX 60.0 CM WATER
.69100E+01	.71300E+10	.99600E+09	.11100E+09	.11800E+08
.67900E+01	.77300E+10	.10900E+10	.12000E+09	.12400E+08
.66700E+01	.84400E+10	.11400E+10	.12900E+09	.12900E+08
.65500E+01	.90600E+10	.12500E+10	.13400E+09	.14000E+08
.64400E+01	.98000E+10	.13200E+10	.14000E+09	.13600E+08
.63200E+01	.10900E+11	.14000E+10	.14700E+09	.14000E+08
.62000E+01	.11600E+11	.14700E+10	.15400E+09	.13500E+08
.60800E+01	.12500E+11	.15500E+10	.15400E+09	.13900E+08
.59600E+01	.13700E+11	.16300E+10	.15100E+09	.13300E+08
.58500E+01	.15000E+11	.17300E+10	.15300E+09	.13900E+08
.57300E+01	.16100E+11	.18200E+10	.15600E+09	.13900E+08
.56100E+01	.18000E+11	.19100E+10	.15900E+09	.14300E+08
.55000E+01	.19500E+11	.20200E+10	.16400E+09	.13500E+08
.53800E+01	.20800E+11	.21100E+10	.16900E+09	.12800E+08
.52600E+01	.22800E+11	.22400E+10	.17500E+09	.14100E+08
.51400E+01	.25000E+11	.23600E+10	.17600E+09	.13500E+08
.50300E+01	.27100E+11	.24400E+10	.18200E+09	.14400E+08
.49100E+01	.28900E+11	.25400E+10	.18500E+09	.14000E+08
.47900E+01	.31000E+11	.26400E+10	.18800E+09	.13400E+08
.46700E+01	.33300E+11	.26500E+10	.18600E+09	.13300E+08
.45500E+01	.35600E+11	.27000E+10	.17600E+09	.12900E+08
.44300E+01	.36900E+11	.27400E+10	.17300E+09	.11500E+08
.43100E+01	.39400E+11	.28500E+10	.17200E+09	.10600E+08
.42000E+01	.41800E+11	.28600E+10	.16200E+09	.10200E+08
.40800E+01	.43900E+11	.28500E+10	.15700E+09	.92600E+07
.39600E+01	.46200E+11	.27600E+10	.14200E+09	.87400E+07
.38400E+01	.48100E+11	.26500E+10	.12400E+09	.74900E+07
.37300E+01	.50800E+11	.25800E+10	.11800E+09	.60400E+07
.36100E+01	.54500E+11	.25800E+10	.10400E+09	.62600E+07
.34900E+01	.58800E+11	.26700E+10	.10500E+09	.53600E+07
.33700E+01	.65700E+11	.30300E+10	.11300E+09	.62000E+07
.32600E+01	.71700E+11	.35600E+10	.13600E+09	.66600E+07
.31400E+01	.78800E+11	.41700E+10	.16100E+09	.80400E+07
.30200E+01	.85100E+11	.47300E+10	.18300E+09	.92500E+07
.29100E+01	.90100E+11	.51600E+10	.20400E+09	.95900E+07
.27900E+01	.95200E+11	.55700E+10	.21300E+09	.89100E+07
.26700E+01	.10400E+12	.58600E+10	.23500E+09	.94300E+07
.25600E+01	.11600E+12	.64000E+10	.24800E+09	.10200E+08
.24400E+01	.12800E+12	.68200E+10	.26900E+09	.11100E+08
.23300E+01	.13800E+12	.69800E+10	.28400E+09	
.22200E+01	.14500E+12	.67700E+10	.25600E+09	
.21000E+01	.15300E+12	.64600E+10	.23300E+09	
.19900E+01	.16200E+12	.62000E+10		

NEUTRON ENERGY IN MEV	FLUX 0 CM GRAPHITE	FLUX 20.2 CM GRAPHITE	FLUX 40.4 CM GRAPHITE	FLUX 60.6 CM GRAPHITE
.12030E+02	.91700E+08	.17000E+08	.24000E+07	.24000E+06
.11910E+02	.11200E+09	.17500E+08	.19900E+07	.29900E+06
.11790E+02	.11500E+09	.16500E+08	.27500E+07	.33700E+06
.11670E+02	.97100E+08	.21400E+08	.20800E+07	.25400E+06
.11550E+02	.14600E+09	.20300E+08	.32200E+07	.35100E+06
.11430E+02	.11200E+09	.26200E+08	.37600E+07	.39700E+06
.11310E+02	.14200E+09	.22300E+08	.34800E+07	.46300E+06
.11190E+02	.15100E+09	.27400E+08	.55000E+07	.58400E+06
.11070E+02	.20700E+09	.31200E+08	.50300E+07	.47400E+06
.10950E+02	.19600E+09	.33600E+08	.54600E+07	.72600E+06
.10830E+02	.21900E+09	.38200E+08	.63400E+07	.97800E+06
.10710E+02	.23800E+09	.46500E+08	.66900E+07	.94900E+06
.10590E+02	.27300E+09	.42000E+08	.64700E+07	.91400E+06
.10470E+02	.28000E+09	.53400E+08	.67900E+07	.12800E+07
.10350E+02	.28700E+09	.55300E+08	.99300E+07	.12700E+07
.10230E+02	.36300E+09	.61300E+08	.94500E+07	.15600E+07
.10110E+02	.34300E+09	.71600E+08	.10500E+08	.13900E+07
.99900E+01	.40700E+09	.71000E+08	.11600E+08	.17400E+07
.98800E+01	.46300E+09	.79600E+08	.12300E+08	.20200E+07
.97600E+01	.44600E+09	.84400E+08	.12900E+08	.20200E+07
.96400E+01	.52100E+09	.87500E+08	.12800E+08	.21800E+07
.95200E+01	.53500E+09	.10800E+09	.16300E+08	.28200E+07
.94000E+01	.57100E+09	.11300E+09	.18900E+08	.28700E+07
.92800E+01	.66300E+09	.12800E+09	.19600E+08	.31300E+07
.91600E+01	.71200E+09	.13700E+09	.21000E+08	.38200E+07
.90400E+01	.81700E+09	.14900E+09	.24100E+08	.45000E+07
.89200E+01	.86300E+09	.15900E+09	.26500E+08	.46000E+07
.88000E+01	.93300E+09	.16800E+09	.27300E+08	.51800E+07
.86800E+01	.98700E+09	.18200E+09	.30600E+08	.58100E+07
.85600E+01	.10700E+10	.19100E+09	.33400E+08	.57900E+07
.84500E+01	.10800E+10	.18600E+09	.29900E+08	.54200E+07
.83300E+01	.12400E+10	.19300E+09	.31600E+08	.54400E+07
.82100E+01	.12700E+10	.19500E+09	.30700E+08	.49300E+07
.80900E+01	.13900E+10	.20700E+09	.29700E+08	.48000E+07
.79700E+01	.14600E+10	.22900E+09	.31400E+08	.54100E+07
.78500E+01	.17500E+10	.25800E+09	.36100E+08	.71000E+07
.77300E+01	.18400E+10	.32600E+09	.56900E+08	.12100E+08
.76200E+01	.20900E+10	.39400E+09	.80200E+08	.19100E+08
.75000E+01	.24900E+10	.49500E+09	.10700E+09	.27600E+08
.73800E+01	.27900E+10	.61700E+09	.13400E+09	.35900E+08
.72600E+01	.31800E+10	.76100E+09	.17800E+09	.46200E+08
.71400E+01	.35800E+10	.88100E+09	.21900E+09	.55600E+08
.70200E+01	.39500E+10	.97400E+09	.24600E+09	.62600E+08

NEUTRON ENERGY IN MEV	FLUX 0 CM GRAPHITE	FLUX 20.2 CM GRAPHITE	FLUX 40.4 CM GRAPHITE	FLUX 60.6 CM GRAPHITE
.69100E+01	.42500E+10	.10500E+10	.26300E+09	.66300E+08
.67900E+01	.45800E+10	.10900E+10	.27400E+09	.67200E+08
.66700E+01	.48700E+10	.11500E+10	.27200E+09	.63800E+08
.65500E+01	.52500E+10	.11600E+10	.26000E+09	.60000E+08
.64400E+01	.56300E+10	.11700E+10	.25600E+09	.54400E+08
.63200E+01	.59300E+10	.12100E+10	.24600E+09	.50100E+08
.62000E+01	.63800E+10	.12500E+10	.24400E+09	.46600E+08
.60800E+01	.68900E+10	.13400E+10	.24300E+09	.44000E+08
.59600E+01	.72600E+10	.14500E+10	.25900E+09	.44800E+08
.58500E+01	.80200E+10	.15500E+10	.27800E+09	.45600E+08
.57300E+01	.86400E+10	.16500E+10	.30000E+09	.47000E+08
.56100E+01	.91600E+10	.17800E+10	.31800E+09	.50500E+08
.55000E+01	.99300E+10	.19400E+10	.34600E+09	.54200E+08
.53800E+01	.10500E+11	.20500E+10	.35700E+09	.54600E+08
.52600E+01	.11600E+11	.21600E+10	.37800E+09	.57400E+08
.51400E+01	.12200E+11	.22300E+10	.37500E+09	.62200E+08
.50300E+01	.13100E+11	.23300E+10	.38300E+09	.64700E+08
.49100E+01	.13800E+11	.23400E+10	.40000E+09	.62200E+08
.47900E+01	.14400E+11	.22900E+10	.37800E+09	.55900E+08
.46700E+01	.15000E+11	.22600E+10	.34500E+09	.47300E+08
.45500E+01	.15300E+11	.21300E+10	.30900E+09	.41300E+08
.44300E+01	.16000E+11	.20400E+10	.26900E+09	.35700E+08
.43100E+01	.16600E+11	.19500E+10	.24000E+09	.27800E+08
.42000E+01	.17500E+11	.19200E+10	.21800E+09	.26400E+08
.40800E+01	.17800E+11	.18300E+10	.18800E+09	.20900E+08
.39600E+01	.17600E+11	.16600E+10	.17100E+09	.19500E+08
.38400E+01	.17300E+11	.14600E+10	.14800E+09	.16900E+08
.37300E+01	.17400E+11	.13500E+10	.13000E+09	.14800E+08
.36100E+01	.18100E+11	.13100E+10	.11200E+09	.12000E+08
.34900E+01	.19500E+11	.15000E+10	.12000E+09	.14600E+08
.33700E+01	.22300E+11	.19500E+10	.16800E+09	.18600E+08
.32600E+01	.25300E+11	.24900E+10	.23700E+09	.26200E+08
.31400E+01	.28900E+11	.29000E+10	.29900E+09	.32800E+08
.30200E+01	.31200E+11	.31900E+10	.32500E+09	.38800E+08
.29100E+01	.34600E+11	.33800E+10	.32700E+09	.36100E+08
.27900E+01	.39600E+11	.38700E+10	.34500E+09	.38000E+08
.26700E+01	.45600E+11	.46100E+10	.39400E+09	.43100E+08
.25600E+01	.52200E+11	.55300E+10	.48200E+09	.51900E+08
.24400E+01	.57600E+11	.63100E+10	.57500E+09	.60800E+08
.23300E+01	.60000E+11	.68200E+10	.65900E+09	.68500E+08
.22200E+01	.61400E+11	.71400E+10	.71200E+09	.71600E+08
.21000E+01	.63400E+11	.75100E+10	.75800E+09	.74100E+08
.19900E+01	.66500E+11	.79100E+10	.81300E+09	

REFERENCES

1. F. C. Maienschein, "Methods of Fast-Neutron Spectroscopy for Reactor Shielding," Shielding Division Report ANS-SD-2, pp. 1-9, American Nuclear Society (1965).

2. E. P. Blizard and P. S. Mittelman, "Recent Advances in Reactor Shielding in the United States," Proc. Third United Nations Inter. Conf. on Peaceful Uses of Atomic Energy, Vol. 4, 348 (1964).

3. M. Grotenhuis, P. S. Mittelman, and E. P. Blizard, "Reactor Shielding in the United States of America," Reactor Shielding, Technical Reports Series No. 34, pp. 98-107, International Atomic Energy Agency (1964).

4. Yu. A. Egorov, "Some Problems of Biological Shielding in Reactors," Reactor Shielding, Technical Reports Series No. 34, pp. 108-134, International Atomic Energy Agency (1964).

5. A. D. Kantz, "Average Neutron Energy of Reactor Spectra and Its Influence on Displacement Damage," J. Appl. Phys., 34, 1944 (1963).

6. A. D. Rossin, "Dosimetry for Radiation Damage Studies," ANL-6826, Argonne National Laboratory (1964).

7. R. E. Dahl and H. H. Yoshikawa, "Neutron-Exposure Correlation for Radiation-Damage Studies," Nucl. Sci. Eng., 21, 312 (1965).

8. F. Storrer, "Pulsed Neutron Experiments on Fast and Intermediate Systems," Pulsed Neutron Research, Vol. II, pp. 317-335, International Atomic Energy Agency (1965).

9. W. Y. Kato et al., "Fast-Reactor Physics Parameters from a Pulsed Source," Pulsed Neutron Research, Vol. II, pp. 373-396, International Atomic Energy Agency (1965).

10. H. Borgwaldt et al., "SUAK, A Fast Subcritical Facility for Pulsed Neutron Measurements," Pulsed Neutron Research, Vol. II, pp. 399-415, International Atomic Energy Agency (1965).

11. J. L. Russell, Jr. and A. E. Profio, "Adequacy of Fast and Intermediate Cross Section Data from Measurement of Neutron Spectra in Bulk Media," Neutron Cross Section Technology, CONF-660303, pp. 782-795 (1966).

REFERENCES (Continued)

12. S. Preiser, G. Rabinowitz, and E. deDufour, "A Program for the Numerical Integration of the Boltzmann Transport Equation-NIOBE," ARL Technical Report 60-314, Nuclear Development Corp. (1960). Also reprinted as UNUCOR-632, United Nuclear Corp. (1963).

13. D. Yetman, B. Eisenman, and G. Rabinowitz, "Description of Input Preparation and Operating Procedures for 9-NIOBE, an IBM-7090 Code," NDA 2143-18, United Nuclear Corp. (1961). Also reprinted as UNUCOR-631, United Nuclear Corp. (1963).

14. S. Preiser, "9-NIOBE (UNC-90-2) Computer Code Abstract," Nucl. Sci. Eng., 12, 447 (1962).

15. K. D. Lathrop, "DTF-IV, a FORTRAN-IV Program for Solving the Multigroup Transport Equation with Anisotropic Scattering," LA-3373, Los Alamos Scientific Laboratory (1965).

16. D. C. Irving et al., "05R, A General-Purpose Monte Carlo Neutron Transport Code," ORNL-3622, Oak Ridge National Laboratory (1965).

17. J. Butler et al., "Methods for Calculating Radiation Attenuation in Shields," Reactor Shielding, Technical Reports Series No. 34, pp. 146-151, International Atomic Energy Agency (1964).

18. "Neutron Attenuation in Optically Thick Shields," Shielding Division Report ANS-SD-1, American Nuclear Society (1964).

19. R. B. Murray, "Methods of Fast-Neutron Spectroscopy," WADC Technical Note 57-298, Part I, pp. 151-171, Wright Air Development Center, Wright-Patterson Air Force Base, Ohio (1958).

20. B. V. Rybakov and V. A. Sidorov, Fast-Neutron Spectroscopy, Consultants Bureau, New York (1960).

21. "Measurement of Neutron Flux and Spectra for Physical and Biological Applications," National Bureau of Standards Handbook 72 (1960).

22. L. Cranberg and L. Rosen, "Measurement of Fast Neutron Spectra," in Nuclear Spectroscopy, Part A, F. Ajzenberg-Selove, ed., pp. 358-398, Academic Press, New York (1960).

REFERENCES (Continued)

23. J. M. Calvert and A. A. Jaffe, "Neutron Spectroscopy," in Fast Neutron Physics, Part II: Experiments and Theory, J. B. Marion and J. L. Fowler, eds., pp. 1907-1952, Interscience Publishers, New York (1963).

24. R. Wallace, "Four-Pi Fast-Neutron Spectrometers for Detection and Dosimetry," Neutron Dosimetry, Vol. I, pp. 575-587, International Atomic Energy Agency (1963).

25. R. A. Coombe, "Neutron Energy Spectra - Its Measurement in the Energy Range 0.5 to 15 Mev," Nucl. Power, 8, pp. 47-50 (Jan. 1963), pp. 46-48 (Feb. 1963), and pp. 54-56 (April 1963).

26. K. H. Beckurts and K. Wirtz, Neutron Physics, trans. L. Dresner, pp. 286-296, Springer Verlag, New York (1964).

27. G. Di Cola and A. Rota, "Calculation of Differential Fast-Neutron Spectra from Threshold-Foil Activation Data by Least-Squares Series Expansion Methods," Nucl. Sci. Eng., 23, 344 (1965).

28. W. N. McElroy, S. Berg, and G. Gigas, "Neutron-Flux Spectral Determination by Foil Activation," Nucl. Sci. Eng., 27, 533 (1967).

29. S. H. Levine and R. E. Fortney, "Effect of Threshold Cross Section on the Derivation of Fast-Neutron Spectra," Neutron Cross Section Technology, CONF-660303, pp. 660-674 (1966).

30. J. L. Russell, Jr. et al., "Determination of Neutron Spectra in Bulk Media by Time-of-Flight," Pulsed Neutron Research, Vol. II, pp. 445-459, International Atomic Energy Agency (1965).

31. D. B. Gayther and P. D. Goode, "Measurements of Fast Neutron Spectra in Reactor Materials," Pulsed Neutron Research, Vol. II, pp. 435-443, International Atomic Energy Agency (1965).

32. W. J. Paterson, W. B. McCormick, and J. W. Weale, "Some Measurements of Fast Reactor Spectra by the Time-of-Flight Technique Using a Pulsed Neutron Source," Pulsed Neutron Research, Vol. II, pp. 417-433, International Atomic Energy Agency (1965).

33. A. E. Profio, "Verification of Analytical Techniques (GAPLSN-Transport Theory and 05R-Monte Carlo Theory) by Utilization of Measured Fast Neutron Spectra in Infinite Paraffin and Spherical Paraffin Shields," GA-6765, General Atomic (1966). Also designated AFWL-TR-65-193, Air Force Weapons Laboratory, Kirtland Air Force Base, New Mexico (1966).

REFERENCES (Continued)

34. A. E. Profio, J. U. Koppel, and A. Adamantiades, "Measurements and Calculations of the Slowing-Down and Migration Time," Pulsed Neutron Research, Vol. I, pp. 123-138, International Atomic Energy Agency (1965).

35. R. J. Huber, "In-Core Experiments with a Li^6 'Sandwich' Fast Neutron Spectrometer," Shielding Division Report ANS-SD-2, pp. 25-38, American Nuclear Society (1965).

36. V. V. Verbinski and M. S. Bokhari, "Measurements and Calculations of Energy and Angular Details of Fast Neutron Flux in Water from a Pool-Type Reactor," Shielding Division Report ANS-SD-2, pp. 71-111, American Nuclear Society (1965).

37. V. V. Verbinski et al., "Measurements and Calculations of the Spectral and Spatial Details of the Fast-Neutron Flux in Water Shields," Nucl. Sci. Eng., 27, 283 (1967).

38. A. W. Manning et al., "He^3 - Spectrometer Characteristics and Applications," Nucleonics, 23, No.4, 69 (1965).

39. T. R. Jeter and M. C. Kennison, "Recent Improvements in Helium-3 Solid State Neutron Spectrometry," IEEE Trans. Nucl. Sci., NS-14, No. 1, 422 (1967).

40. A. Sayres, "^{3}He Fast Neutron Spectrometer with Extended Energy Range," Shielding Division Report ANS-SD-2, pp. 136-140, American Nuclear Society (1965).

41. W. A. Bair, "An Improved ^{3}He Neutron Spectrometer," UCRL-16595, University of California Lawrence Radiation Laboratory (1966).

42. R. B. Murray, "Use of ^{6}LiI(Eu) as a Scintillation Detector and Spectrometer for Fast Neutrons," Nucl. Instrum. Methods, 2, 237 (1958).

43. N. Hartmann and G. R. Hopkins, "Fast Neutron Penetration Through Reactor Shields," WAPD-T-783, Westinghouse Atomic Power Division (1959).

44. H. W. Broek and C. E. Anderson, "The Stilbene Scintillation Crystal as a Spectrometer for Continuous Fast-Neutron Spectra," Rev. Sci. Instrum., 31, 1063 (1960).

REFERENCES (Continued)

45. G. G. Doroshenko, V. G. Zolotukhin, and B. A. Efimenko, "Matrix Analysis of Data Obtained by Means of a Single-Crystal Fast-Neutron Scintillation Spectrometer," Atomnaya Énergiya, 19, 51 (1965).

46. V. G. Zolotukhin, G. G. Doroshenko, and B. A. Efimenko, "Analysis of Systematic Error in Differentiating Apparatus Spectra Measured by Means of a Single-Crystal Fast-Neutron Spectrometer," Atomnaya Énergiya, 19, 56 (1965).

47. W. R. Burrus and V. V. Verbinski, "Recent Developments in the Proton-Recoil Scintillation Neutron Spectrometer," Shielding Division Report ANS-SD-2, pp. 148-185, American Nuclear Society (1965).

48. V. V. Verbinski et al., "The Response of Some Organic Scintillators to Fast Neutrons," Shielding Division Report ANS-SD-2, pp. 189-228, American Nuclear Society (1965).

49. C. E. Clifford et al., "Measurements of the Spectra of Uncollided Fission Neutrons Transmitted Through Thick Samples of Nitrogen, Oxygen, Carbon, and Lead: Investigation of the Minima in Total Cross Sections," Nucl. Sci. Eng., 27, 299 (1967).

50. E. F. Bennett, "Fast Neutron Spectroscopy by Proton-Recoil Proportional Counting," Nucl. Sci. Eng., 27, 16 (1967).

51. E. F. Bennett, "Neutron Spectrum Measurement in a Fast Critical Assembly," Nucl. Sci. Eng., 27, 28 (1967).

52. E. F. Bennett, "Neutron Spectra in a Depleted Uranium Block," Trans. Am. Nucl. Soc., 9, 234 (1966).

53. C. H. Johnson, "Recoil Telescope Detectors," in Fast Neutron Physics, Part I: Techniques, J. B. Marion and J. L. Fowler, eds., pp. 247-295, Interscience Publishers, New York (1960).

54. S. B. Herdade et al., "Simplified Proton-Recoil 'Telescope' for Reactor-Beam Fast-Neutron Spectrometry," Neutron Dosimetry, Vol. I, pp. 409-415, International Atomic Energy Agency (1963).

55. A. K. Furr and R. S. Runyon, "A Fast Neutron Spectrometer for Reactor Flux Measurements," Nucl. Instrum. Methods, 27, 292 (1964).

REFERENCES (Continued)

56. E. R. Flynn and H. C. Bryant, "High Efficiency Solid State Neutron Telescope for 15-35 Mev Neutrons," Rev. Sci. Instrum., 37, 215 (1966).

57. L. Harris, Jr., G. Sherwood, and J. S. King, "Fast-Neutron Spectra in Water and Graphite," Nucl. Sci. Eng., 26, 571 (1966).

58. C. M. Cialella, "Design and Calibration of a Broad Range Magnetic Neutron Spectrometer," IEEE Trans. Nucl. Sci., NS-12, No. 1,400 (1965).

59. C. M. Cialella, "A Broad Range Magnetic Neutron Spectrometer," BRL MR 1753, U. S. Army Ballistic Research Laboratories, Aberdeen Proving Ground, Maryland (1966).

60. R. G. Cochran and K. M. Henry, "Fast Neutron Spectra of the BSF Reactor," AECD-3720, Oak Ridge National Laboratory (1953).

61. R. G. Cochran et al., "Reactor Radiations Through Slabs of Graphite," CF-54-7-105, Oak Ridge National Laboratory (1954).

62. V. V. Verbinski, "Fast-Neutron Transport in LiH," Trans. Am. Nucl. Soc., 6, 190 (1963).

63. G. D. Trimble, G. K. Houghton, and J. H. Audas, "Measurement of Neutron Spectra in Liquid Hydrogen," GA-5750, General Atomic (1964). Also assigned NASA-CR-54230, National Aeronautics and Space Administration (1964).

64. G. D. Trimble et al., "Fast-Neutron Spectra in Liquid Hydrogen," Trans. Am. Nucl. Soc., 8, 465 (1965).

65. A. E. Profio and J. Kirkbride, "Measurement of Fast Neutron Spectra in an Infinite Medium of CH_2," GA-5973, General Atomic (1964). Also assigned WL-TR-64-180, Air Force Weapons Laboratory, Kirtland Air Force Base, New Mexico (1964).

66. A. E. Profio, "Fast-Neutron Spectra in Paraffin Shields," Trans. Am. Nucl. Soc., 8, 464 (1965).

67. A. E. Profio, H. M. Antunez, and J. L. Russell, Jr., "Time-of-Flight Measurements of the Neutron Angular-Flux Spectrum in Graphite," Trans. Am. Nucl. Soc., 9, 351 (1966).

68. V. N. Avaev et al., "Spectra of Fast Pile Neutrons in Passage through Polyethylene," Atomnaya Énergiya, 15, 20 (1963).

REFERENCES (Continued)

69. A. P. Veselkin et al., "Spectra of Fast Reactor Neutrons after Passing through Graphite, Lead, and Iron," Atomnaya Énergiya, 16, 32 (1964).

70. G. A. Vasil'ev et al., "The Attenuation of Reactor Radiation by Means of Serpentine Concrete," Atomnaya Énergiya, 18, 121 (1965).

71. G. G. Doroshenko and I. V. Filyushkin, "The Spectra of Fast Neutrons from a Po-Be Source Which Have Passed through Water Shielding," Atomnaya Énergiya, 16, 152 (1964).

72. G. G. Doroshenko, V. A. Fedorov, and E. S. Leonov, "Changes in Fast-Neutron Spectra after Penetrating Aluminum, Paraffin, and Water," Atomnaya Énergiya, 19, 460 (1965).

73. G. During, R. Jansson, and N. Starfelt, "Experimental Fast-Neutron Spectra in Aluminum and Iron," Neutron Dosimetry, Vol. I, pp. 359-367, International Atomic Energy Agency (1963).

74. S. Passe, "Measurement of Fast-Neutron Spectra by Means of Nuclear Emulsions," Neutron Dosimetry, Vol. I, pp. 481-499, International Atomic Energy Agency (1963). In French.

75. E. Tochilin, "Flux and Spectral Measurements of Primary and Moderated Neutron Sources," Neutron Dosimetry, Vol. I, pp. 553-563, International Atomic Energy Agency (1963).

76. G. Ben-David, E. Nardi, and M. Pasternak, "Fast-Neutron Spectroscopy in a Pool-Type Reactor with Activation Detectors," Nucl. Sci. Eng., 20, 281 (1964).

77. E. Aalto, R. Fraeki, and R. Sandlin, "Measured and Predicted Variations in Fast Neutron Spectrum in Massive Shields of Water and Concrete," Nucl. Struct. Eng., 2, 233 (1965).

78. J. R. Stehn et al., "Neutron Cross Sections, Volume I, Z=1 to 20," BNL 325, 2nd ed., Supplement No. 2, Brookhaven National Laboratory (1964).

79. J. O. Hirschfelder and J. L. Magee, "Range-Energy Relations for Protons in Substances Containing C, H, O, A, and Xe," Phys. Rev., 73, 207 (1948).

REFERENCES (Continued)

80. J. B. Parker, P. H. White, and R. J. Webster, "The Interpretation of Recoil Proton Spectra," Nucl. Instrum. Methods, 23, 61 (1963).

81. W. H. Barkas and M. J. Berger, "Tables of Energy Losses and Ranges of Heavy Charged Particles," NAS-NRC Publication 1133, Nucl. Sci. Series Report No. 39, pp. 103-172, National Academy of Sciences - National Research Council (1964).

82. P. J. Van Heerden, "The Crystal Counter: A New Instrument in Nuclear Physics," Noord-Hollandsche Uitgevers-Mij., Amsterdam (1945).

83. K. G. McKay, "A Germanium Counter," Phys. Rev., 76, 1537 (1949).

84. Proc. Informal Conf. Semiconductor Nucl. Particle Detectors, Asheville, N. C., Sept. 28-30, 1960, J.W.T. Dabbs and F. J. Walter, eds., NAS-NRC Publication 871, Nucl. Sci. Series Report No. 32, National Academy of Sciences-National Research Council (1961).

85. Proc. IRE Prof. Group Nucl. Sci. Annual Meeting, Solid State Radiation Detectors, Gatlinburg, Tenn., Oct. 3-5, 1960, IRE Trans. Nucl. Sci., NS-8, No. 1 (1961).

86. W. J. Price, Nuclear Radiation Dectection, 2nd. ed., pp. 212-266, McGraw-Hill Book Co., New York (1964).

87. J. M. Taylor, Semiconductor Particle Detectors, Butterworths, London (1963).

88. G. Dearnaley and D. C. Northrop, Semiconductor Counters for Nuclear Radiation, John Wiley, New York (1963).

89. G. D. O'Kelley, "Detection and Measurement of Nuclear Radiation," NAS-NS 3105, pp. 58-75, National Academy of Sciences - National Research Council (1962).

90. W. Shockley, "Problems Related to p-n Junctions in Silicon," Solid-State Electronics, 2, 35 (1961).

91. A. G. Chynoweth, "Energy Required for Electron-Hole Pair Formation in Silicon," NAS-NRC Publication 871, Nucl. Sci. Series Report No. 32, pp. 95-98, National Academy of Sciences-National Research Council (1961).

REFERENCES (Continued)

92. C. Bussolati, A. Fiorentini, and G. Fabri, "Energy for Electron-Hole Pair Generation in Silicon by Electrons and Alpha Particles," Phys. Rev., 136, A1756 (1964).

93. F. E. Emery and T. A. Rabson, "Temperature Dependence of Average Energy per Pair in Semiconductor Detectors," IEEE Trans. Nucl. Sci., NS-13, No. 1, 48 (1966).

94. S. A. Baranov, V. M. Kulakov, and V. M. Shatinsky, "New Data on Am^{243} and Am^{241} Alpha Decays," Nucl. Phys., 56, 252 (1964).

95. A. H. Wapstra, "Recalibration of Alpha Particle Energies," Nucl. Phys., 57, 48 (1964).

96. C. M. Lederer et al., "Energy Levels of ^{237}Np, (I). The Alpha Decay of ^{241}Am," Nucl. Phys., 84, 481 (1966).

97. P. Siffert, A. Coche, and F. Hibou, "Resolution Limitation of Solid State Radiation Detectors for Heavy Particles," IEEE Trans. Nucl. Sci., NS-13, No. 3, 225 (1966).

98. H. DeLyser, F. P. Ziemba, and W. R. Van Antwerp, "A Lithium Drifted Germanium Surface Barrier Detector," IEEE Trans. Nucl. Sci., NS-12, No. 1, 265 (1965).

99. R. L. Chase, Nuclear Pulse Spectrometry, pp. 39-40, McGraw-Hill Book Co., New York (1961).

100. J. L. Gammel, "The n-p Total and Differential Cross Sections in the Energy Range 0-40 Mev," in Fast Neutron Physics, Part II: Experiments and Theory, J. B. Marion and J. L. Fowler, eds., pp. 2185-2226, Interscience Publishers, New York (1963).

101. J. B. Bullock, "Absolute Power Measurements of the Ford Nuclear Reactor," Trans. Am. Nucl. Soc., 8 (Supplement), 26 (1965).

102. E. E. Lockett and R. H. Thomas, "The Half-Lives of Several Radioisotopes," Nucleonics, 11, No. 3, 14 (1953).

103. G. G. Sherwood, University of Michigan Doctoral Thesis, in progress.

REFERENCES (Continued)

104. J. Certaine and P. S. Mittelman, "A Procedure for the Numerical Integration of the Boltzmann Transport Equation," NDA 10-161, Nuclear Development Corp. (1955).

105. B. E. Watt, "Energy Spectrum of Neutrons from Thermal Fission of U^{235}," Phys. Rev., 87, 1037 (1952).

106. L. Cranberg et al., "Fission Neutron Spectrum of U^{235}," Phys. Rev., 103, 662 (1956).

107. J. Terrell, "Fission Neutron Spectra and Nuclear Temperatures," Phys. Rev., 113, 527 (1959).

108. J. Terrell, "Neutron Yields from Individual Fission Fragments," Phys. Rev., 127, 880 (1962). See Appendix I, Fission Neutron Emission Energies.

109. J. Terrell, "Prompt Neutrons from Fission," Physics and Chemistry of Fission, Vol. II, pp. 3-23, International Atomic Energy Agency (1965).

110. E. K. Hyde, The Nuclear Properties of the Heavy Elements, III, Fission Phenomena, pp. 237-242, Prentice-Hall, Englewood Cliffs, N. J. (1965).

111. H. Condé and G. During, "Fission Neutron Spectra of U^{235}, Pu^{239}, and Cf^{252}," Physics and Chemistry of Fission, Vol. II, pp. 93-102, International Atomic Energy Agency (1965).

112. D. J. Hughes and R. B. Schwartz, "Neutron Cross Sections," BNL 325, 2nd ed., Brookhaven National Laboratory (1958).

113. C. R. Lubitz, private communication with G. G. Sherwood on unpublished C^{12} cross sections and Legendre coefficients (1965).

114. E. L. Slaggie and J. T. Reynolds, "O^{16} Fast Neutron Cross Sections and Legendre Moments Below 15.0 Mev," KAPL-M-6452, Knolls Atomic Power Laboratory (1965).

115. G. D. Joanou and C. A. Stevens, "Neutron Cross Sections for Aluminum," GA-5884, General Atomic (1964).

REFERENCES (Concluded)

116. A. Simon and C. E. Clifford, "The Attenuation of Neutrons by Air Ducts in Shields," Nucl. Sci. Eng., 1, 156 (1956).

117. A. Langsdorf, Jr., "Experimental Applications of Shielding and Collimating to Neutrons from Sources Employing the Electrostatic Generator," WADC Technical Note 57-298, Part I, pp. 196-206, Wright Air Development Center, Wright-Patterson Air Force Base, Ohio (1958).

118. A. Langsdorf, Jr., "Neutron Collimation and Shielding for Experimental Purposes," in Fast Neutron Physics, Part I: Techniques, J. B. Marion and J. L. Fowler, eds., pp. 721-806, Interscience Publishers, New York (1960).

119. B. Antolković et al., "Influence of Collimation on the Energy Spectrum of 2.7 Mev Neutrons," Glasnik mat.-fiz. i astr., 16, 135 (1961).

120. D. C. Piercey and D. E. Bendall, "The Transmission of Fast Neutrons Along Air Filled Ducts in Water," AEEW-R-69, United Kingdom Atomic Energy Authority (1962).

121. W. B. Green and R. S. Hubner, "Monte Carlo Analysis of Neutron-Collimator Efficiency," Trans. Am. Nucl. Soc., 8, 65 (1965).

122. E. A. Straker and M. B. Emmett, "Fast Neutron Collimator Studies," Trans. Am. Nucl Soc., 9, 355 (1966). Also ORNL 3973, Vol. I, pp. 40-41, Oak Ridge National Laboratory (1966).

123. L. C. Northcliffe, "Passage of Heavy Ions Through Matter, II. Range-Energy Curves," NAS-NRC Publication 1133, Nucl. Sci. Series Report No. 39, pp. 173-186, National Academy of Sciences-National Research Council (1964).